THE UNIVERSITY OF CHICAGO

DESIGNING, PROBING, AND STABILIZING EXOTIC FABRY-PEROT CAVITIES FOR STUDYING STRONGLY CORRELATED LIGHT

A DISSERTATION SUBMITTED TO
THE FACULTY OF THE DIVISION OF THE PHYSICAL SCIENCES
IN CANDIDACY FOR THE DEGREE OF
DOCTOR OF PHILOSOPHY

DEPARTMENT OF PHYSICS

BY
ALBERT RYOU

CHICAGO, ILLINOIS
AUGUST 2017

To my family and friends

TABLE OF CONTENTS

LIST OF FIGURES

LIST OF TABLES

ACKNOWLEDGMENTS

It has truly been a blessing to have been Jon's student. Everybody knows that he is a brilliant physicist, the foremost of his generation. I can attest that the brilliance of his mind is matched only by the deepest care he has for his students. Since the moment I first stepped into his office five years ago, Jon has been both a mentor and a friend. He has taught me so much, not just about physics but about life as well. I will remember these lessons for a long time.

Soon after I joined Simon Lab as an inaugural member, our postdoc Ariel Sommer arrived. Ariel is a model scientist. He is kind, gentle, caring, and of course, he is a genius too. I was always amazed by the way he could explain things with absolute crystal clarity. I am extremely thankful for his guidance on many projects I worked on, and I will strive to follow his example as I begin my own postdoc career.

As for my fellow graduate colleagues: Jia Ningyuan and Nathan Schine are some of the hardest-working people I have met. Seeing them in lab day and night and over the weekends served as a great motivation, and they have been very generous whenever I needed help. Clai Owens is tremendously friendly, and his jokes can immediately brighten up any day. Aziza Suleymanzade and Mark Stone are so full of smarts, wits, and laughter that it is a pleasure to be in their company. Finally, Alex Georgakopoulos, my first labmate as well as one of my roommates for the last four years, is a wonderful, one-of-a-kind scholar. I will miss bantering with him.

The undergraduate students in Simon Lab have been just as fun to work with. I thank Aaron Krahn, Michael Cervia, Tahoe Schrader, Michelle Chalupnik, and many others for their dazzling and pure positive energy that only undergrads can bring to lab. And I thank Graham Greve for having been a good friend both in and out of lab.

I would also like to thank the wonderful people without whom our lab would not have been possible. Pegg Anderson was exceptionally nice and kind, far beyond helping us with lab orders or conference registrations, and Maria Jimenez has been incredibly supportive

as well. Helmut Krebs and Luigi Mazzenga have been enormously generous in teaching me invaluable machine shop skills. Finally, John Phillips is not only the best building manager but also an exceptionally kind-hearted person; every one of our encounters began and ended with his warmest smile.

Just as important to my graduate life as my colleagues in lab have been my colleagues outside of lab. I will most fondly remember the weekly dinner and board game nights with Mengfei He, Pavel Motloch, Tony Antorre, and my other roommate for the last four years, Johnny Ho.

Finally, I thank my family - my parents Jaiwon and Yunju and my sister Audrey and my brother-in-law Yale - for their unconditional love, support, and encouragement.

ABSTRACT

Synthetic materials made of engineered quasiparticles are a powerful platform for studying manybody physics and strongly correlated systems due to their bottom-up approach to Hamiltonian modeling. Photonic quasiparticles called polaritons are particularly appealing since they inherit fast dynamics from light and strong interaction from matter. This thesis describes the experimental demonstration of cavity Rydberg polaritons, which are composite particles arising from the hybridization of an optical cavity with Rydberg EIT, as well as the tools for probing and stabilizing the cavity.

We first describe the design, construction, and testing of a four-mirror Fabry-Perot cavity, whose small waist size on the order of 10 microns is comparable to the Rydberg blockade radius. By achieving strong coupling between the cavity photon and an atomic ensemble undergoing electromagnetically induced transparency (EIT), we observe the emergence of the dark-state polariton and characterize its single-body properties as well as the single-quantum nonlinearity.

We then describe the implementation of a holographic spatial light modulator for exciting different transverse modes of the cavity, an essential tool for studying polariton-polariton scattering. To compensate for optical aberrations, we employ a digital micromirror device (DMD), combining beam shaping with adaptive optics to produce diffraction-limited light. We quantitatively measure the purity of the DMD-produced Hermite-Gauss modes and confirm up to 99.2% efficiency. One application of the technique is to create Laguerre-Gauss modes, which have been used to probe synthetic Landau levels for photons in a twisted, nonplanar cavity.

Finally, we describe the implementation of an FPGA-based finite impulse response (FIR) filter for stabilizing the cavity. We digitally cancel the acoustical resonances of the feedback-controlled mechanical system, thereby demonstrating an order-of-magnitude enhancement in the feedback bandwidth from 200 Hz to more than 2 kHz. Harnessing the massive processing power of a state-of-the-art FPGA, we present a novel, low-latency digital architecture for

loop-shaping, with applications in atomic physics and beyond.

CHAPTER 1

INTRODUCTION

It is a testament to the richness of quantum mechanics that nearly a century after its foundations were laid out, its consequences are still being explored today. Strongly correlated manybody phenomena like superconductivity [1] and quantum phase transitions [2] are at the forefront of current research in both theoretical and experimental condensed matter physics.

An extremely fruitful approach to studying these complicated phenomena is with quantum simulations - realizing model Hamiltonians in simple, well-understood systems and mapping the results back to real-life materials. For instance, ultracold atoms trapped in optical lattices have been used to simulate the spin-1/2 Ising chain [3] or the low-temperature, doped Hubbard model [4].

The field of quantum simulations has in turn given birth to synthetic materials, where the goal is to engineer systems that operate in hitherto unexplored parameter regimes and gain new insight. Often the choice of building block for synthetic materials is a photonic quasiparticle called a polariton, which inherits both the fast dynamics of photons and the quantum properties of the matter they couple to. Some of the examples of polaritons include exciton polaritons in semiconductor microcavities [5], magnons [6], and surface plasmons [7]; for an excellent overview of these systems, see Ref. [8].

The goal of this thesis is to build a new form of synthetic material, that of strongly correlated light, in the quantum nonlinear regime. Direct photon-photon interactions are negligibly weak, so they require a nonlinear medium. Nonlinear crystals exist, but they too require a large number of photons for operation. We aim to build a photonic crystal made of quasiparticles called cavity Rydberg polaritons, taking advantage of recent advances in both optical and atomic physics.

1.1 Strongly interacting photons with Rydberg EIT

The combination of electromagnetically induced transparency (EIT) with Rydberg atoms has recently gained significant interest as an attractive candidate for realizing a strong single-quantum nonlinearity. Under EIT, an atomic ensemble with three energy levels, $|g\rangle$, $|e\rangle$, and $|r\rangle$, is made transparent to a "probe" laser driving $|g\rangle \rightarrow |e\rangle$ in the presence of a "control" laser driving $|e\rangle \rightarrow |r\rangle$ [9]. The spectral window of transparency, which can reach 100% transmission, can be made extremely narrow; any photon with a frequency that falls outside this window is scattered by the lossy $|e\rangle$.

Enter Rydberg atoms. Atoms excited to states with a high principal quantum number n exhibit strong, long-range van der Waals interaction [10]. When $|r\rangle$ in EIT is a Rydberg state, a single Rydberg atom pushes all other atoms within its "blockade radius" out of resonance with the control laser [11]. The conversion of a coherent probe beam into a correlated train of blockade-radius-separated photons is a springboard for many technological applications, including single-photon switches and all-optical deterministic quantum logic [12].

Single-photon nonlinearity with Rydberg EIT has been successfully demonstrated in free space. Dudin *et al.* reported a small single-photon generation efficiency [13]. Peyronel *et al.* showed both two-photon attenuation and one-photon transmission up to 60% in a cold atomic gas [14], and soon after they reported an observation of a coherently traveling two-photon bound state in the dispersive regime [15]. While these works focused on one-dimensional nonlinearity, our objective is to synthesize a polaritonic crystal, which requires a spatial order in higher dimensions. To access this degree of freedom, we turn to an optical cavity.

1.2 Optical cavities and cavity QED

The past couple of decades have seen extraordinary experiments probing fundamental cavity quantum electrodynamics, in particular, in the strong coupling regime between light and

matter [16]. Hood *et al.* observed the vacuum Rabi splitting for cold atoms coupled to a high-finesse optical cavity [17], as did Boca *et al.* for "one-and-the-same-atom" [18]. A two-level atom, due to the anharmonicity of the Jaynes-Cummings ladder, presents its own type of photon blockade. Birnbaum *et al.* measured the intensity correlation function of the light transmitted from their atom-cavity system and confirmed its sub-Poissonian and antibunching behavior [19].

1.3 Cavity Rydberg polaritons

In the spirit of combining different fields to bring about new physics, as has been the case with EIT and Rydberg atoms as well as cold atoms trapped in optical cavities, our goal is to synthesize strongly correlated light by fusing Rydberg EIT with an optical cavity. Instead of driving $|g\rangle \leftrightarrow |e\rangle$ directly with a probe laser, we couple the atomic transition to a cavity resonance. The result is the creation of a cavity Rydberg polariton, which exhibits both the single-photon nonlinearity and the strong, long-range interaction. When combined with the cavity's degenerate modes, cavity Rydberg polaritons provide a robust platform for studying photonic quantum materials, including the polaritonic fluid-to-crystal phase transition [20].

1.4 Overview of the thesis

The star of the thesis is undeniably the optical cavity, which plays a critical role in creating cavity Rydberg polaritons and hosting polariton-polariton interactions. Before diving into our main experiment, I will review some of the theoretical background in Gaussian optics and light-matter interaction that guided the cavity's design. After the Rydberg experiment, I will discuss two powerful experimental tools, a spatial light modulator and a digital filter, which began as accessories to the cavity but very soon grew into their own major topics with far-reaching implications.

Chapter 2 introduces the basic concepts behind an optical cavity. I first review its fre-

quency spectrum and discuss how the cavity eigenstates, or modes, arise from the impedance relations. Then, I talk about the geometrical properties, starting with the paraxial approximation and arriving at the ABCD matrix formalism, an elegant aid in understanding the propagation of a laser beam through optical elements, including a cavity.

Chapter 3 introduces the light-matter interaction. Beginning with dressed states arising from the coupling between the atoms and the cavity field, I describe dissipation and re-formulate the strong coupling regime in terms of the atom-field cooperativity. I then address the collective excitation of an atomic ensemble and the electromagnetically induced transparency. Finally, I conclude by describing Rydberg atoms and the effect of their strong, long-rang interaction on quantum nonlinearity.

Chapter 4 discusses the design, construction, and science of the four-mirror experimental cavity for the cavity Rydberg polariton experiment. I start by explaining the cavity requirements such as the small waist size and mode degeneracy. Then, I summarize the first experimental results, characterizing the single polariton behavior, followed by the observation of nonclassical light in our second-generation cavity.

Chapter 5 discusses the use of a digital micromirror device as a holographic spatial modulator and its applications. I first review beam shaping and adaptive optics using the theory of Fourier optics. Then, I present an experimental procedure for coupling light into higher-order cavity modes. The chapter concludes with a brief summary of a major application in probing synthetic Landau levels for photons in a twisted cavity.

Chapter 6 discusses an FPGA-based digital filter for enhancing the cavity stabilization. I introduce general concepts in feedback and control theory and the critical role that acoustical resonances play in limiting the feedback bandwidth. I then discuss the implementation of a finite impulse response filter for digitally canceling the resonances and improving the cavity lock. The chapter ends with suggestions for further development and applications beyond AMO physics.

Chapter 7 concludes the thesis with an outlook for the experiments, both current and on

the horizon. The references and the appendix follow.

CHAPTER 2

OPTICAL CAVITY

2.1 Introduction

Optical cavities, long-venerated components in lasers, filters, and nonlinear frequency synthesizers, play a critical role in quantum optics. Pioneering experiments in cavity quantum electrodynamics (cQED) demonstrated the cavity's ability to suppress, enhance, and even reverse the spontaneous emission of atoms in the cavity, culminating in the strong matter-field coupling [21]. Today's cavities and qubits come in an exotic array of shapes and sizes [22], and they have become indispensable tools in such applications as quantum metrology [23] and quantum information processing [24].

The major advantage of a cavity made of discrete bulk mirrors is its robust mode engineering. The cavity modes' spatial, spectral, and spin degrees of freedom can all be finely tuned. An optical cavity coupled to laser-cooled atoms provides an elegant platform for exploring quantum manybody physics.

This chapter introduces the physics relevant for understanding Fabry-Perot optical cavities, the type that is employed in our cavity Rydberg polariton experiment. I first derive important cavity parameters regarding impedance matching and Gaussian optics before addressing mode degeneracy. The details for designing and building the actual experimental cavity will be deferred to Chapter 4.

2.2 Basic cavity parameters

A Fabry-Perot cavity consists of two thin, partially reflecting surfaces, separated by a distance d. Each "mirror" is characterized by a reflection amplitude coefficient r and a transmission amplitude coefficient t.

A plane wave field E incident on a mirror gives rise to a transmitted field tE and a

reflected field rE. The total transmitted field through the cavity is the coherent sum of all successive transmitted fields:

$$E_T = E_0 t_1 e^{ikd} t_2 + E_0 t_1 e^{ikd} r_2 e^{ikd} r_1 e^{ikd} t_2 + ... \tag{2.1}$$

$$= E_0 t_1 t_2 e^{ikd} \left(1 + r_1 r_2 e^{ik2d} + ...\right) \tag{2.2}$$

$$= E_0 \frac{t_1 t_2 e^{ikd}}{1 - r_1 r_2 e^{ik2d}} \tag{2.3}$$

where E_0 is the incident field.

The transmitted intensity is

$$I_T = |E_T|^2 = I_0 \frac{T_1 T_2}{1 + R_1 R_2 - 2\sqrt{R_1 R_2}\cos\delta} \tag{2.4}$$

where $R = |r|^2$, $T = |t|^2$, and $\delta = k2d$ is the round-trip phase. R is called reflectivity.

Factoring out $\left(1 - \sqrt{R_1 R_2}\right)^2$ from the denominator:

$$\frac{I_T}{I_0} = \frac{T_1 T_2}{\left(1 - \sqrt{R_1 R_2}\right)^2} \frac{1}{1 + \frac{4\sqrt{R_1 R_2}}{\left(1 - \sqrt{R_1 R_2}\right)^2} \sin^2(\delta/2)} \tag{2.5}$$

$$= \frac{T_1 T_2}{\left(1 - \sqrt{R_1 R_2}\right)^2} \frac{1}{1 + f \sin^2(\delta/2)} \tag{2.6}$$

which thus defines the coefficient of finesse f:

$$f = \frac{4\sqrt{R_1 R_2}}{\left(1 - \sqrt{R_1 R_2}\right)^2} \tag{2.7}$$

The cavity transmission is given by the second term in Equation 2.6, $1/(1 + f \sin^2(\delta/2))$, known as the Airy function, modulated by the first term. The plot of the transmission for different coefficients of finesse is shown in Fig. 2.1.

For lossless mirrors, energy conservation means $R + T = 1$. For a cavity made of identical mirrors ($R_1 = R_2$), the maximum transmitted intensity equals the incident intensity: all

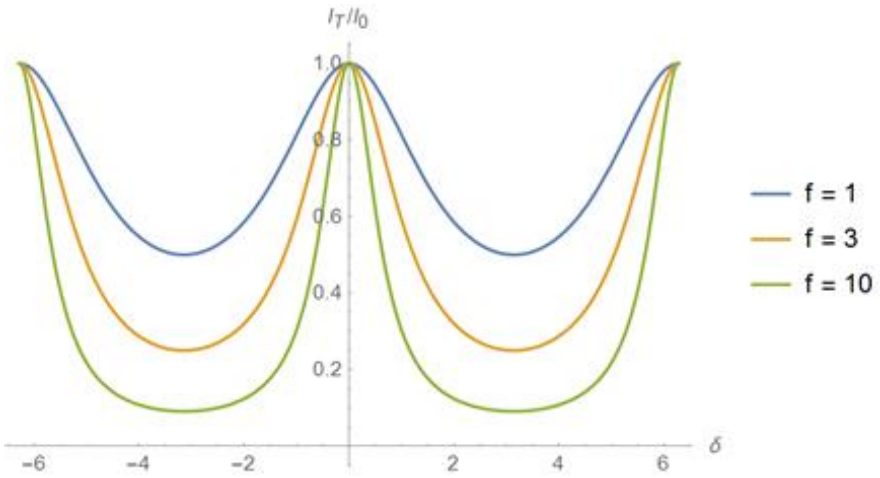

Figure 2.1: **Cavity transmission.** The plot shows the transmitted light as a function of the phase δ for different values of the coefficient of finesse. Low values of f have been chosen for illustration; for $R = 0.99$, $f \approx 40000$, yielding extremely sharp peaks.

incident intensity gets transmitted, and none is reflected. The cavity is then said to be *impedance matched*.

Maximum transmission: modes

The cavity transmission is 2π-periodic in δ, so the condition for maximum transmission is given by $k2d = 2\pi n$, where n is an integer. Plugging in for $k = 2\pi/\lambda$,

$$k2d = 2\pi n \rightarrow d = n\left(\frac{\lambda}{2}\right) \tag{2.8}$$

Thus, maximum transmission occurs when an integer number of half-waves fit in the cavity. For mirrors with high reflectivity ($R > 0.99$), the transmission appears as a series of extremely sharp peaks, called the *modes* of the cavity.

Free spectral range, linewidth, and finesse

The difference in phase between two adjacent modes is given by

$$k'2d' - k2d = 2\pi \tag{2.9}$$

If we attribute this phase difference to the difference in the frequency ν of the light (i.e. $d' = d$), then

$$\nu_{FSR} = \frac{c}{2d} \tag{2.10}$$

is called the free spectral range. Note that ν_{FSR} is the inverse of the time it takes for light to make one round trip inside the cavity.

Let δ_{width} be the FWHM of the mode in phase:

$$\frac{1}{1 + f \sin^2 \delta_{width}/4} = \frac{1}{2} \tag{2.11}$$

$$\delta_{width} = 4 \sin^{-1}\left(\frac{1}{\sqrt{f}}\right) \approx \frac{4}{\sqrt{f}} \tag{2.12}$$

where the last approximation is valid for $f > 1$.

The frequency linewidth $\delta\nu$ is then given by

$$\delta\nu = \delta_{width} \cdot \frac{\nu_{FSR}}{2\pi} = \frac{4}{\sqrt{f}} \frac{\nu_{FSR}}{2\pi} \tag{2.13}$$

Actually, $\delta\nu$ is more commonly given by defining finesse F to be the ratio of ν_{FSR} over the linewidth:

$$F = \frac{v_{FSR}}{\delta\nu} \tag{2.14}$$

$$= \frac{\pi}{2}\sqrt{f} \tag{2.15}$$

$$= \frac{\pi}{2}\left[\frac{4\sqrt{R_1 R_2}}{\left(1 - \sqrt{R_1 R_2}\right)^2}\right]^{1/2} \tag{2.16}$$

Defined this way, F is related to the number of round trips the cavity light makes before leaking out of the cavity. Each round trip takes $t_{round} = 2d/c = 1/\nu_{FSR}$, and the cavity

lifetime is given by $\tau = 1/(2\pi\delta\nu)$. Thus, the number of round trips is given by

$$N_{round} = \frac{\tau}{t_{round}} = \frac{1/(2\pi\delta\nu)}{1/\nu_{FSR}} = \frac{F}{2\pi} \tag{2.17}$$

Reflected field

The reflected field will be useful later (see Appendix C), so let's calculate it now. Proceeding as before by summing up the successively reflected fields:

$$E_R = -E_0 r_1 + E_0 t_1 e^{ikd} r_2 e^{ikd} t_1 + E_0 t_1 e^{ikd} r_2 e^{ikd} r_1 e^{ikd} r_2 e^{ikd} t_1 + ... \tag{2.18}$$

$$= E_0 \left(-r_1 + r_2 t_1^2 e^{ik2d} \left(1 + r_1 r_2 e^{ik2d} + ... \right) \right) \tag{2.19}$$

$$= E_0 \left(\frac{r_2 t_1^2 e^{ik2d}}{1 - r_1 r_2 e^{ik2d}} - r_1 \right) \tag{2.20}$$

Note that the directly reflected field (first term in the series) must appear with a sign flip upon reflection due to the difference in the indices of refraction.

For a symmetric, lossless cavity:

$$\frac{E_R}{E_0} = \frac{r\left(e^{i\delta} - 1\right)}{1 - r^2 e^{i\delta}} \tag{2.21}$$

$$\frac{I_R}{I_0} = \frac{2R\left(1 - \cos\delta\right)}{1 + R^2 - 2R\cos\delta} \tag{2.22}$$

where $\delta = 2kd$ as before.

Intracavity field

Let's also calculate what the intracavity field should be:

$$E_I = E_0 t_1 + E_0 t_1 r_2 e^{ikd} r_1 e^{ikd} + ... \tag{2.23}$$

$$= E_0 t_1 \left(1 + r_1 r_2 e^{ik2d} + ...\right) \tag{2.24}$$

$$= E_0 \frac{t_1}{1 - r_1 r_2 e^{ik2d}} \tag{2.25}$$

Thus, $I_I = I_T / T_2$, which amounts to considerable intensity buildup. For high-finesse cavities,

$$\frac{I_I}{I_0} = \frac{T}{(1-R)^2} \approx \frac{F}{\pi} \tag{2.26}$$

which is called the cavity enhancement factor. It is for this reason that cavities are commonly employed together with nonlinear crystals.

2.3 Gaussian optics

If the mirrors are concave instead of flat, the cavity field is more appropriately described by Gaussian waves rather than plane waves. The result is the appearance of *transverse* modes in addition to the *axial* modes described in the previous section. I begin with an overview of the small-angle, or paraxial, approximation that leads to the fundamental Gaussian and higher-order modes. The complex beam parameter q, combined with the ABCD matrix formalism, provides a simple yet powerful tool for understanding and designing cavities.

2.3.1 Paraxial wave equation

The scalar wave equation, $\nabla^2 u = \frac{1}{c} \frac{\partial^2 u}{\partial t^2}$, can be solved by assuming a monochromatic plane wave modulated by a slowly varying envelope ψ:

$$u(x, y, z) = \psi(x, y, z) e^{i(kz - \omega t)} \tag{2.27}$$

Under the paraxial approximation, the normal to the wavefront makes a negligibly small angle with the optical axis (z-axis in this case) such that $\left|\frac{\partial^2\psi}{\partial z^2}\right| \ll \left|\frac{\partial^2\psi}{\partial x^2}\right|, \left|\frac{\partial^2\psi}{\partial y^2}\right|$ and $\left|\frac{\partial\psi}{\partial z}\right| \ll \kappa\,|\psi|$. The resulting equation

$$\nabla_t^2\psi - 2ik\frac{\partial\psi}{\partial z} = 0 \tag{2.28}$$

where ∇_t^2 is the transverse Laplacian, is called the paraxial wave equation.

2.3.2 The Gaussian beam

The paraxial wave equation admits a family of solutions, the simplest of which is the Gaussian beam given by

$$\psi(x,y,z) = \exp\left[-i\left(P(z) + \frac{k}{2q(z)}r^2\right)\right], \quad r^2 = x^2 + y^2 \tag{2.29}$$

where the complex beam parameter, q, is defined as:

$$\frac{1}{q} \equiv \frac{1}{R} - i\frac{\lambda}{\pi w^2} \tag{2.30}$$

The original wave then becomes

$$u(x,y,z) = \exp\left[-i\left(P(z) + kz + k\frac{r^2}{2R}\right) - \frac{r^2}{w^2}\right] \tag{2.31}$$

which is a Gaussian with a phase shift. w characterizes the radial size of the beam and R the wavefront radius.

The Gaussian beam has a minimum size at the waist where the wavefront radius becomes inifinite. The q parameter at the waist is:

$$q(R=\infty) \equiv q_0 = i\frac{\pi w_0^2}{\lambda} \tag{2.32}$$

Placing $z = 0$ at the waist gives the following neat properties of the beam:

$$z_R \equiv \frac{\pi w_0^2}{\lambda} \tag{2.33}$$

$$q(z) = q_0 + z = iz_R + z \tag{2.34}$$

$$w(z) = w_0 \sqrt{1 + \left(\frac{z}{z_R}\right)^2} \tag{2.35}$$

$$R(z) = z\left[1 + \left(\frac{z_R}{z}\right)^2\right] \tag{2.36}$$

The Rayleigh range z_R quantifies how fast a diffraction-limited beam expands: the more tighly focused the beam is at its waist, the faster it expands.

Finally, solving for $P(z)$ leads to the complete Gaussian beam:

$$u(x, y, z) = \frac{w_0}{w(z)} \exp\left[i\zeta(z) - ik\left(z + \frac{r^2}{2R}\right) - \frac{r^2}{w^2}\right] \tag{2.37}$$

where $\zeta(z) \equiv \tan^{-1}\left(\frac{z}{z_R}\right)$ is called the Gouy phase. Note that on axis ($r = 0$), the phase shift due to kz is much greater than the Gouy phase. The latter is important for determining the resonant frequencies of the cavity modes.

2.3.3 ABCD matrix formalism

The reason for introducing the q parameter is that an extremely useful formalism, called the ABCD matrix, exists for propagating q through various optics. In classical ray optics, every optical element, such as a lens or a mirror, can be associated with a 2 x 2 matrix that describes its action on the incident ray's displacement and angle [25]. The total action of a series of optical elements on a light ray is then given by the product of the corresponding ABCD matrices in sequence.

The most remarkable fact is that the same ABCD matrices for rays describe how the q parameter, associated with Gaussian waves, propagates through the optics. According to

Table 2.1: Common ABCD matrices.

Common ABCD matrices	
Free space, length d	$\begin{pmatrix} 1 & d \\ 0 & 1 \end{pmatrix}$
Thin lens, focal length f	$\begin{pmatrix} 1 & 0 \\ -1/f & 1 \end{pmatrix}$
Mirror, radius of curvature R	$\begin{pmatrix} 1 & 0 \\ -2/R & 1 \end{pmatrix}$

the ABCD rule [25],

$$q' = \frac{Aq + B}{Cq + D} \tag{2.38}$$

where A, B, C, and D correspond to the individual matrix elements.

The ABCD matrices of common optical elements are listed in Table 2.1.

2.3.4 Optical cavity

A cavity is just a series of optical elements whose light path forms a closed loop, so we naturally use the theory of Gaussian optics and the ABCD matrix developed above. If a certain light field replicates itself after one round trip, then that field configuration constitutes a mode [25].

Stability criterion

Only certain *stable* geometric configurations have modes. The stability criterion is given by stipulating that the q parameter remain the same after one cavity round trip:

$$q' = q = \frac{Aq + B}{Cq + D} \tag{2.39}$$

Using $AD - BC = 0$ (ABCD matrices are orthogonal),

$$q = \frac{A - D}{2C} \pm \frac{\sqrt{(A + D)^2 - 4}}{2C} \tag{2.40}$$

It is more convenient to solve for $1/q$:

$$\frac{1}{q} = \frac{C + D\left(\frac{1}{q}\right)}{A + B\left(\frac{1}{q}\right)} \tag{2.41}$$

whence

$$\frac{1}{q} = \frac{D - A}{2B} \pm \frac{\sqrt{(A + D)^2 - 4}}{2B} \tag{2.42}$$

Since the ABCD matrix is real, the first term must be associated with the real part of q and the latter the imaginary part. Then, from the definition of $1/q$:

$$R = \frac{2B}{D - A} \tag{2.43}$$

$$w = \sqrt{\frac{\lambda}{\pi} \frac{|B|}{\sqrt{1 - ((A + D)/2)^2}}} \tag{2.44}$$

Thus, for a mode to exist, w must be real, which means

$$\left| \frac{A + D}{2} \right| \leq 1 \tag{2.45}$$

Constraints on R_1 and R_2 for a two-mirror cavity

Consider a cavity made of two concave mirrors with radii of curvature R_1 and R_2, separated by distance d. The ABCD matrix for the cavity is (starting at the middle of the cavity):

$$\begin{pmatrix} A & B \\ C & D \end{pmatrix} = \begin{pmatrix} 1 & d/2 \\ 0 & 1 \end{pmatrix} \begin{pmatrix} 1 & 0 \\ -2/R_1 & 1 \end{pmatrix} \begin{pmatrix} 1 & d \\ 0 & 1 \end{pmatrix} \begin{pmatrix} 1 & 0 \\ -2/R_2 & 1 \end{pmatrix} \begin{pmatrix} 1 & d/2 \\ 0 & 1 \end{pmatrix} \tag{2.46}$$

$$= \begin{pmatrix} 2g_1g_2 - g_1 + g_2 - 1 & \frac{d}{2}(2g_1g_2 + g_1 + g_2) \\ \frac{2}{d}(2g_1g_2 - g_1 - g_2) & 2g_1g_2 + g_1 - g_2 - 1 \end{pmatrix} \tag{2.47}$$

where

$$g_1 \equiv 1 - \frac{d}{R_1} \tag{2.48}$$

$$g_2 \equiv 1 - \frac{d}{R_2} \tag{2.49}$$

Applying the stability criterion then yields a simple relation in terms of g_1 and g_2:

$$\left|\frac{A+D}{2}\right| \leq 1 \tag{2.50}$$

$$0 \leq g_1g_2 \leq 1 \tag{2.51}$$

2.3.5 N-mirror cavity

A cavity can be made up of more than two mirrors. While much of the formalism for the two-mirror cavity carries over, a N-mirror cavity has a few important differences:

1. Running-wave instead of standing-wave configuration
2. The reflected beam is physically displaced from the incident beam.
3. Additional spatial degree of freedom

Table 2.2: Summary of cavity parameters.

Summary of cavity parameters		
Parameter	N-mirror	Identical two-mirror, low-loss
ν_{FSR}	$\frac{c}{d_{total}}$	$\frac{c}{2d}$
Finesse, F	$\frac{\pi}{2}\left[\frac{4\sqrt{\left(\prod_{i=1}^{N} R_i\right)(1-A)}}{\left(1-\sqrt{\left(\prod_{i=1}^{N} R_i\right)(1-A)}\right)^2}\right]^{1/2}$	$\frac{2\pi}{L}, L = 2T + 2A$
Maximum I_T/I_0	$\frac{T_1 T_2 (1-A)}{\left(1-\sqrt{\left(\prod_{i=1}^{N} R_i\right)(1-A)}\right)^2}$	$\frac{1}{(1+A/T)^2}$
Maximum I_I/I_0	$(I_T/I_0)/T_2$	$\frac{1}{T}\frac{1}{(1+A/T)^2} \approx \frac{F}{\pi}$

4. Nonplanarity

The most apparent difference is that a N-mirror cavity is a running-wave configuration, whereas the two-mirror cavity is necessarily a standing-wave configuration. This difference becomes significant when atoms are placed in the cavity. For a standing-wave cavity, the atom-cavity interaction becomes strongly dependent on the atoms' location relative to the nodes and the antinodes.

Another difference between the two cavity types is that the reflected beam of an N-mirror cavity is physically separated from that of the incident beam. The main effect is in how one implements the Pound-Drever-Hall technique for cavity locking [26] (see Appendix C).

The spatial degree of freedom afforded by the cavity modes will be the subject of the next chapter.

Finally, nonplanarity, where cavity mirrors are not coplanar, induces a field rotation upon a cavity round trip [27], a topic that will be discussed in Chapter 5.

The calculations for cavity transmission, reflection, etc. for a N-mirror cavity proceed in the same way as that for a two-mirror cavity. Table **??** lists the formulas for some of the cavity parameters.

2.3.6 Higher-order modes

The Gaussian beam is actually the lowest order in the family of modes that satisfy the paraxial wave equation. The solutions in Cartesian coordinates are called Hermite-Gauss modes and they are given by

$$u(x,y,z)_{mn} = \frac{w_{0,x}}{w_x(z)}\frac{w_{0,y}}{w_y(z)} H_m\left(\sqrt{2}\frac{x}{w_x}\right) H_n\left(\sqrt{2}\frac{y}{w_y}\right) \exp\left[i\zeta(n,m;z)) - ik\left(z + \frac{x^2}{2q_x} + \frac{y^2}{2q_y}\right)\right] \tag{2.52}$$

where H_m is a Hermite polynomial of order m. The Gouy phase is

$$\zeta(m,n;z) = \left(m+\frac{1}{2}\right)\tan^{-1}\left(\frac{z}{z_{R,x}}\right) + \left(n+\frac{1}{2}\right)\tan^{-1}\left(\frac{z}{z_{R,y}}\right) \tag{2.53}$$

A specific Hermite-Gauss mode is labeled TEM_{mn}. Note that a careful distinction has been made to account for astigmatism ($w_{0,x} \neq w_{0,y}$) in the case of N-mirror cavities. Also note that the use of other coordinate systems gives different solutions. For example, in cylindrical coordinates, the solutions are instead Laguerre-Gauss modes. I will re-visit them in Chapter 5.

2.3.7 Resonant frequencies

The requirement that the phase replicate itself after one cavity round trip gives the resonant frequencies of the modes. On axis, the phase comes from kz and the Gouy phase. The accounting becomes easier if we think of the cavity as a periodic lens sequence. As an example, let's calculate the resonant frequencies of a two-mirror cavity (no astigmatism).

Two-mirror cavity

Starting at the cavity waist and moving to the right, the total round-trip phase is given by

$$\phi = 2kd - (m+n+1)\left[\tan^{-1}\left(\frac{d_2}{z_R}\right) + \tan^{-1}\left(\frac{d_1}{z_R}\right) + \tan^{-1}\left(\frac{d_2}{z_R}\right) + \tan^{-1}\left(\frac{d_1}{z_R}\right)\right] \tag{2.54}$$

$$= 2kd - 2\,(m+n+1)\left[\tan^{-1}\left(\frac{d_2}{z_R}\right) + \tan^{-1}\left(\frac{d_1}{z_R}\right)\right] \tag{2.55}$$

where d_1 and d_2 are the distances to the mirrors from the waist.

This round-trip phase must equal $2\pi q$, where q is an integer (not the same as the q parameter!). Plugging in for $k = \omega/c$ then gives the resonant frequencies for TEM_{mnq}:

$$2\pi q = 2kd - 2\,(m+n+1)\left[\tan^{-1}\left(\frac{d_2}{z_R}\right) + \tan^{-1}\left(\frac{d_1}{z_R}\right)\right] \tag{2.56}$$

$$\nu_{mnq} = \left\{q + \frac{(m+n+1)}{\pi}\left[\tan^{-1}\left(\frac{d_2}{z_R}\right) + \tan^{-1}\left(\frac{d_1}{z_R}\right)\right]\right\}\nu_{FSR} \tag{2.57}$$

where $\nu_{FSR} = c/2d$ as we defined in the previous section.

The integer q designates specific *axial* modes, and for each such mode, there are an infinite number of *transverse* modes labeled by m and n. For optical frequencies, q is a very large number. Since it is not informative to know what q is, often only the transverse modes TEM_{mn} are specified.

The generalization to N-mirror cavities is fairly straightforward, and I carry out the calculation for a *four*-mirror cavity in Chapter 4. The tricky part is to note that due to astigmatism, $z_{R,x} \neq z_{R,y}$ and that there may be more than one cavity waist.

2.4 Mode degeneracy

The existence of transverse modes gives rise to the possibility of mode degeneracy, where more than one mode have the same frequency. For instance, for a two-mirror cavity, $\mathrm{TEM}_{mn} =$

TEM_{nm}. A few special cavity configurations with regard to the transverse mode spacing are discussed below.

2.4.1 Confocal cavity: $R_1 = R_2 = d$

Let the cavity mirrors with radii of curvature $R = d$ be separated by d. The waist size of the cavity after taking the limit $R \to d$ (directly plugging in $R = d$ in the ABCD matrix yields 0/0 !) is

$$w_0 = \sqrt{\frac{\lambda d}{2\pi}} \tag{2.58}$$

so the Rayleigh range is

$$z_R = \frac{\pi w_0^2}{\lambda} = \frac{d}{2} \tag{2.59}$$

Since the mirrors are located $d/2$ from the waist,

$$\tan^{-1}\left(\frac{d_2}{z_R}\right) + \tan^{-1}\left(\frac{d_1}{z_R}\right) = 2\tan^{-1}(1) = \frac{\pi}{2} \tag{2.60}$$

and the resonant frequencies are (in units of ν_{FSR})

$$\nu_{mnq} = q + \frac{(m+n+1)}{2} \tag{2.61}$$

Let's see what the resonant frequencies of the first few TEM_{mnq} modes are:

$$\nu_{00q} = q + \frac{1}{2} \tag{2.62}$$

$$\nu_{01q}, \nu_{10q} = q + \frac{1}{2} + \frac{1}{2} \tag{2.63}$$

$$\nu_{02q}, \nu_{11q}, \nu_{20q} = q + \frac{1}{2} + \frac{1}{2} + \frac{1}{2} = q' + \frac{1}{2}, \quad q' = q + 1 \tag{2.64}$$

Very interesting! The even modes ($m + n = 0 \bmod 2$) are degenerate with mode spacing ν_{FSR}, and the odd modes ($m + n = 1 \bmod 2$) are also degenerate with the same spacing but located between the even modes.

A confocal cavity has a huge mode degeneracy, but the waist size tends to be large. For a 10-cm cavity using 780-nm wavelength light, the waist size is about 35 μm. In order for the waist size to be about 10 μm, the cavity length would have to be about 0.8 mm.

2.4.2 Spherical cavity: $R_1 = R_2 = d/2$

Proceeding as before by taking the limit $R \to d/2$,

$$w_0 \approx 0 \tag{2.65}$$

$$z_R \approx 0 \tag{2.66}$$

$$2\tan^{-1}(\infty) = \pi \tag{2.67}$$

and

$$\nu_{mnq} = q + m + n + 1 \tag{2.68}$$

This rather unusual cavity is totally degenerate, with all the modes sitting on top of one another and separated by ν_{FSR}. It also barely fulfills the cavity stability criterion and so is technically very challenging to build.

2.5 Example: Cavity mode matching

We end this chapter with a practical example of cavity mode matching. Mode matching means adjusting the input light's beam size and wavefront curvature to match that of a cavity mode, ensuring optimal coupling. While it is possible in theory to accomplish this with a single lens, the constraint on the lens' location makes this impractical (real estate on a typical optical breadboard is very valuable). The convention is therefore to use two lenses.

First we choose a lens with focal length f. We would like to place this lens such that the cavity waist will be at its focus. Because a cavity mirror acts as a diverging optic for the transmitting beam, we must place the lens at a distance slightly greater than f away from

the waist.

We then calculate the coupling efficiency between a beam propagated from the optical fiber and a beam propagated backward from the cavity waist on a given plane, say the plane of the cavity lens, as a function of the fiber collimator's focal length and the distance between the collimator and the lens. See Appendix A for the derivation of the coupling efficiency.

So far we have assumed that the two beams share the same optical axis. In practice, one must optimize the coupling by hand while looking at the cavity transmission on an oscilloscope. Having two mirrors on mirror mounts gives the two degrees of freedom per axis required to tune both the displacement and the angle of the beam.

Other tools that are helpful to have on hand are a fault finder, which is a HeNe laser pointer that serves as a visible aid in optical alignment, and a beam profiler for measuring the spot size of a beam at various physical locations.

CHAPTER 3

CAVITY QED

3.1 Introduction

The goal of this chapter is to understand the interaction between an ensemble of atoms and light confined in a cavity. Starting with a minimal model - a single two-level atom coupled to a single cavity mode - I will gradually build on it and introduce important concepts like dissipation, strong coupling, and cavity Rydberg polaritons. On the other hand, I will not give detailed descriptions of laser cooling and trapping, for which many excellent references are available [28].

To set the scene: a free excited atom tends to decay spontaneously to the ground state, emitting a photon into one of the infinitely many modes of the free-space continuum. The character of this spontaneous emission can be dramatically changed, however, by placing it inside a cavity. For a cavity whose length is smaller than $\lambda/2$, the atom cannot radiate and so the emission is suppressed [29]. For a cavity whose length matches $n\lambda/2$, the vacuum fluctuations stimulate the atom to emit a photon into a cavity mode, enhancing the emission. Finally, in a high-finesse cavity, the radiated photon may be re-absorbed by the same atom before it has time to leak out of the cavity, turning the emission into a "reversible" coherent process [30].

3.2 A two-level atom in a single-mode cavity

Our initial system consists of a single, two-level atom, initially in its excited state, sitting in an empty single-mode cavity. Some time later, the atom jumps from the excited state to the ground state, emitting a photon into the cavity mode. This photon then lives in the cavity until it gets re-absorbed by the atom, and the process repeats. The coherent back-and-forth exchange of the energy quantum between the atom and the cavity occurs at the rate Ω called

the Rabi frequency, and the phenomenon is known as a vacuum Rabi oscillation. We now take a look at the system's eigenstates and eigenvalues.

Let $|G1\rangle = |atom\rangle \otimes |photon\rangle$ denote the state with the atom in the ground state and one photon in the cavity and $|E0\rangle$ that with the atom in the excited state and zero photon in the cavity. In the "dressed" picture, these are the uncoupled, or bare, states. When coupling is introduced, the Hamiltonian can be written as [1]

$$H = \hbar\omega_c |G1\rangle \langle G1| + \hbar\omega_a |E0\rangle \langle E0| + \hbar g \left(|E0\rangle \langle G1| + |G1\rangle \langle E0|\right) \tag{3.1}$$

where ω_c is the cavity photon frequency, ω_a is the atomic transition frequency, and g is the atom-photon coupling strength.

In matrix representation, $|G1\rangle = \binom{1}{0}$, $|E0\rangle = \binom{0}{1}$, and

$$H = \hbar \begin{pmatrix} \omega_c & g \\ g & \omega_a \end{pmatrix} \tag{3.3}$$

Let's re-normalize the energy scale by subtracting ω_a from the diagonal terms (which does not affect the dynamics) and set $\hbar = 1$. The Hamiltonian then becomes

$$H = \begin{pmatrix} \delta & g \\ g & 0 \end{pmatrix} \tag{3.4}$$

where the detuning $\delta = \omega_c - \omega_a$.

---

1. Formally, the Jaynes-Cummings Hamiltonian is written as [31]:

$$H = \frac{1}{2}\hbar\omega_a\sigma_z + \hbar\omega_c a^\dagger a + \hbar g(\mathbf{r})(\sigma + \sigma^\dagger)(a + a^\dagger) \tag{3.2}$$

where the σ's are the Pauli operators for the atomic excitation and the a's are the creation/annihilation operators for the cavity photon. The rotating wave approximation selects out only those terms in the interaction that conserve the total number of excitation.

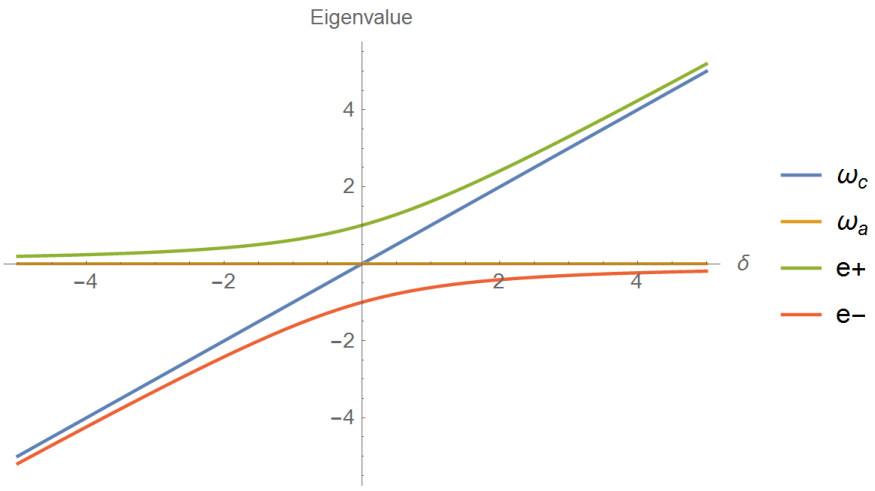

Figure 3.1: **Energy spectrum of the dressed states.** The eigenvalues of both the dressed and the bare states are plotted as a function of the cavity detuning δ; $g = 1$. For large δ, the dressed states are approximately the bare states. At $\delta = 0$, the dressed states are equally balanced superpositions of the bare states.

The eigenvalues, which we denote $e_\pm$, are

$$e_\pm = \frac{1}{2}\left(\delta \pm \sqrt{\delta^2 + (2g)^2}\right) \tag{3.5}$$

The plot of $e_\pm$ vs. δ, along with the bare states, is shown in Fig. 3.1.

The eigenstates, $|e_\pm\rangle$, depend on the sign of δ. For $\delta \geq 0$,

$$\begin{aligned} |e_+\rangle &= \cos\frac{\theta}{2}|G1\rangle + \sin\frac{\theta}{2}|E0\rangle \\ |e_-\rangle &= -\sin\frac{\theta}{2}|G1\rangle + \cos\frac{\theta}{2}|E0\rangle \end{aligned} \tag{3.6}$$

and for $\delta < 0$,

$$\begin{aligned} |e_+\rangle &= \sin\frac{\theta}{2}|G1\rangle + \cos\frac{\theta}{2}|E0\rangle \\ |e_-\rangle &= -\cos\frac{\theta}{2}|G1\rangle + \sin\frac{\theta}{2}|E0\rangle \end{aligned} \tag{3.7}$$

where $\tan\theta = 2g/|\delta|$.

Notice that the dressed states $|e_\pm\rangle$ are quantum-entangled atom-cavity states; they are linear superpositions of the bare states, $|G1\rangle$ and $|E0\rangle$, with the amount of mixing determined

by the rotation angle θ.

It is instructional to look at two limiting cases for θ:

Case 1: $|\delta| \gg g$

If the detuning is much larger than the coupling strength, then θ is approximately zero, and the eigenstates and eigenvalues become

$\delta \geq 0$:

$$|e_+\rangle \approx |G1\rangle\,, \quad e_+ = \delta + \frac{g^2}{\delta} \tag{3.8}$$

$$|e_-\rangle \approx |E0\rangle\,, \quad e_- = -\frac{g^2}{\delta} \tag{3.9}$$

$\delta < 0$:

$$|e_+\rangle \approx |E0\rangle\,, \quad e_+ = \frac{g^2}{|\delta|} \tag{3.10}$$

$$|e_-\rangle \approx |G1\rangle\,, \quad e_- = -|\delta| - \frac{g^2}{|\delta|} \tag{3.11}$$

Thus, for large detuning, the dressed states are approximately the same as the bare states, as can be seen in Fig. 3.1 where the dressed states asymptotically approach the bare states

The energy shift g^2/δ, called the light shift or AC Stark shift, is the origin of the widely used dipole trap for neutral atoms, also known as the far off-resonant trap (FORT). A spatially varying g results in a dipole force, $F = -\nabla(g^2/\delta)$ on an atom. For positive δ ("blue-detuned"), atoms are attracted toward low-intensity regions, whereas for negative δ ("red-detuned"), they are attracted to high-intensity regions.

Case 2: $|\delta| \ll g$

For small detuning, θ is approximately $\pi/2$:

$$\begin{aligned} |e_+\rangle &\approx |G1\rangle + |E0\rangle \qquad e_+ = +g \\ |e_-\rangle &\approx |G1\rangle - |E0\rangle \qquad e_- = -g \end{aligned} \tag{3.12}$$

Thus, for small detuning regime, the dressed states are maximally entangled states, made up of equal parts of $|G1\rangle$ and $|E0\rangle$. The frequencies of the eigenstates are by split by $2g$, which is equivalent to the previously mentioned vacuum Rabi frequency, or the rate at which the quantum of energy is exchanged between the atom and the cavity field: $\Omega = 2g$. The vacuum Rabi splitting is a hallmark of strong coupling between the atom and the cavity.

3.2.1 Photon blockade

An interesting feature of the Hamiltonian we just discussed is the nonlinearity observed in the eigenstates with different numbers of photons. Suppose we start with n photons in the cavity instead of one so that the bare states are $|G\,n\rangle$ and $|E\,n-1\rangle$. The maximally entangled dressed states are $|e_\pm\rangle \approx |G\,n\rangle \pm |E\,n-1\rangle$, with their eigenvalues separated by $2g\sqrt{n}$. This means that once we inject one photon into a cavity with a ground-state atom, the second photon of the same frequency that we try to inject will no longer be in resonance.

This nonlinear effect at the single-photon level, arising from the anharmonicity in the energy levels of the Jaynes-Cummings Hamiltonian, is called "photon blockade", and it has been successfully demonstrated by several groups [19, 32]. Photon blockade has been suggested as a candidate for applications in quantum communication and information processing [24], although achieving high-fidelity input/output coupling is a daunting task. Later, we will discuss a different kind of quantum nonlinearity known as Rydberg blockade.

3.3 Dissipation and strong coupling

The previous section discussed a closed atom-cavity system, but a cavity is naturally "open". After all, as we saw in Chapter 2, the lifetime τ of the intracavity field is inversely proportional to its leakage rate $\kappa = 2\pi\delta\nu$, where $\delta\nu$ is the cavity linewidth. Furthermore, the excited atom, instead of solely exchanging energy with the cavity, can spontaneously decay into free space at a rate Γ. We now look at how these sources of dissipation modify the atom-cavity dynamics.

We make a small note here that whereas the leakage light from the cavity via κ can be collected and measured to reveal the state of the atom-cavity system - and indeed this is how we probe our experiment - the light lost via Γ represents an inaccessible loss of information.

Following the phenomenological picture, we include dissipation as imaginary energy in the Hamiltonian:

$$H = \begin{pmatrix} \omega_c - i\frac{\kappa}{2} & g \\ g & \omega_a - i\frac{\Gamma}{2} \end{pmatrix} \tag{3.13}$$

As expected, the eigenstate populations now decay exponentially, with their lifetime given by $\tau = 2/(\Gamma + \kappa)$.

The strong coupling regime, in which a single atom or a photon has a non-negligible effect on the whole system, is defined by the requirement that the reversible oscillation occur much faster than dissipation rates:

$$2g \gg \Gamma, \kappa \tag{3.14}$$

In practice, Γ is a property of a specific energy level of an atom and, in most cavities, is equal to the spontaneous decay rate in free space. κ can be calculated from the cavity mirrors' reflectivities along with the cavity's length. So what is g?

The interaction between the atom and the cavity field is through the induced dipole moment of the atom:

$$\hbar\Omega = \hbar 2g = d \cdot E \tag{3.15}$$

where the field E of the single photon comes from

$$\hbar\omega_c = \frac{1}{2}\epsilon_0 E^2 V \tag{3.16}$$

The volume V is found by integrating the field configuration over the cavity length. Hence, the single-atom-cavity-field coupling g is given by

$$g = \sqrt{\frac{d^2\omega_c}{2\hbar\epsilon_0 V}} \tag{3.17}$$

3.3.1 Cooperativity

Equation 3.17 suggests that a smaller volume leads to higher g, which is the reason behind the wide array of exotic microcavities, such as quartz microspheres and microtoroidal resonators, employed in current research [22]. A closer inspection using the classical description of field scattering, however, shows that the fundamental quantity is the mode area rather than the volume.

The probability that a ground-state atom will absorb an incident photon in a mode with waist size w_0 is given by the ratio of the absorption cross section to the mode size: $P = \sigma_{abs}/\sigma_{mode}$. Plugging in $\sigma_{abs} = 6\pi/k^2$ and $\sigma_{mode} = \pi w_0^2$ gives

$$P = \frac{6}{(kw_0)^2} \tag{3.18}$$

If the atom is placed inside a running-wave cavity, then the probability is enhanced by the number of round trips that the "photon" makes, $F/2\pi$, times 2 to account for both directions. (In a standing wave cavity, the enhancement is further multiplied by 4 due to the anti-node.) Thus, the atom-cavity interaction probability is given by

$$P_{cav} = \eta \equiv \frac{F}{\pi}\frac{6}{(kw_0)^2} \tag{3.19}$$

where we have defined the single-atom cooperativity η.

Actually, Equation 3.19 is only an approximation for when $\eta < 1$; the correct expression is given by [33]:

$$P_{cav} = \frac{\eta}{1+\eta} \tag{3.20}$$

The strong coupling condition is now $P_{cav} \approx 1$, or in terms of the cooperativity, $\eta \gg 1$.

We now show how the cooperativity is related to g, κ, and Γ. It is actually easier to proceed from the other direction: let there be a quantity $\frac{4g^2}{\kappa\Gamma}$. Plugging in the following,

$$g = \sqrt{\frac{d^2\omega_c}{2\hbar\epsilon_0 V}} \tag{3.21}$$

$$\kappa = 2\pi\frac{\nu_{FSR}}{F}, \quad \nu_{FSR} = c/L \tag{3.22}$$

$$\Gamma = \frac{k^2 d^2}{3\pi\epsilon\hbar} \tag{3.23}$$

we arrive at

$$\frac{4g^2}{\kappa\Gamma} = \eta = \frac{F}{\pi}\frac{6}{(kw_0)^2} \tag{3.24}$$

which shows that for achieving strong coupling, there is a premium on having a small waist size.

3.4 Collective excitation of an atomic ensemble

Coupling a single atom to the cavity field is technically challenging, so instead we employ an ensemble of atoms. If we assume that multiple atoms couple to the mode in the same way, then a phenomenon called collective excitation occurs, in which many atoms behave as one effective superatom. The effective cooperativity is correspondingly enhanced by the number of participating atoms.

To start with, let there be two ground-state atoms inside a cavity containing one photon. The bare states are $|GG\rangle = \begin{pmatrix}1\\0\\0\end{pmatrix}$, $|EG\rangle = \begin{pmatrix}0\\1\\0\end{pmatrix}$, and $|GE\rangle = \begin{pmatrix}0\\0\\1\end{pmatrix}$, and the Hamiltonian is

(ignoring dissipation)

$$H = \begin{pmatrix} \delta & g & g \\ g & 0 & 0 \\ g & 0 & 0 \end{pmatrix} \tag{3.25}$$

where the detuning $\delta = \omega_c - \omega_a$ as before.

Note that the eigenvalues for $\delta = 0$ are 0 and $\pm g\sqrt{2}$, suggesting that one eigenstate does not come into the dynamics. This was to be expected, since only two rows in the matrix are unique. Furthermore, the other eigenstates look the same as those for the single atom in a cavity except the coupling now comes with the factor of $\sqrt{2}$.

Anticipating these results, we can choose different bare states to start with. Let $|GG\rangle$ be a bare state as before. For the other two states, instead of picking states where either of the two atoms is in the excited state, we take their superpositions:

$$|E+\rangle = \frac{|EG\rangle + |GE\rangle}{\sqrt{2}} \tag{3.26}$$

$$|E-\rangle = \frac{|EG\rangle - |GE\rangle}{\sqrt{2}} \tag{3.27}$$

The coupling strength between $|GG\rangle$ and the top "super-radiant" state is $g\sqrt{2}$, whereas that for the bottom "sub-radiant" state is zero. Letting $|GG\rangle = \begin{pmatrix} 1 \\ 0 \\ 0 \end{pmatrix}$, $|E+\rangle = \begin{pmatrix} 0 \\ 1 \\ 0 \end{pmatrix}$, and $|E-\rangle = \begin{pmatrix} 0 \\ 0 \\ 1 \end{pmatrix}$, the Hamiltonian becomes

$$H = \begin{pmatrix} \delta & g\sqrt{2} & 0 \\ g\sqrt{2} & 0 & 0 \\ 0 & 0 & 0 \end{pmatrix} \tag{3.28}$$

which shows that only the super-radiant state enters the dynamics.

The result can be generalized to a cavity containing N atoms. The super-radiant superposition represents a collectively excited state that acts like a single atom with its coupling to the cavity field enhanced by $\sqrt{N}$.

The employment of an atomic ensemble correspondingly enhances the cooperativity as well: $\eta \to N\eta$. Hence, even when $\eta < 1$, we may still have $N\eta > 1$ and achieve strong coupling.

3.5 Electromagnetically induced transparency

Let's now consider a three-level atom with the bare states given by $|G\rangle$, $|E\rangle$, and $|R\rangle$, indicating the ground state, the first excited state, and the second state, respectively. Each transition has its own coupling strength. We will denote the $|G\rangle \leftrightarrow |E\rangle$ coupling as $G/2$ and the $|E\rangle \leftrightarrow |R\rangle$ coupling as $\Omega/2$. The Hamiltonian is given by

$$H = \begin{pmatrix} \delta_c & G/2 & 0 \\ G/2 & 0 & \Omega/2 \\ 0 & \Omega/2 & \delta_R \end{pmatrix} \tag{3.29}$$

where $\delta_c = \omega_c - \omega_a$ and $\delta_R = \omega_a - \omega_R - \omega_{control}$. $\omega_{control}$ is the frequency of the light driving the $|E\rangle \leftrightarrow |R\rangle$ transition.

The 3 x 3 matrix yields three eigenstates. Under a special condition $\delta_c = \delta_R$, called the electromagnetically induced transparency (EIT), one of the three eigenstates of the Hamiltonian is given by

$$|D\rangle = \cos\theta\,|G\rangle - \sin\theta\,|R\rangle \tag{3.30}$$

which contains no $|E\rangle$ component. The dark-state rotation angle θ is defined by $\tan\theta = G/\Omega$.

The meaning of the dark state $|D\rangle$ is as follows: An atom whose excited state $|E\rangle$ is lossy presents an opaque medium to a "probe" photon that drives $|G\rangle \to |E\rangle$. However, when a "control" laser that drives $|E\rangle \to |R\rangle$ is also present, then there results a special eigenstate that can propagate without loss (assuming of course that both $|G\rangle$ and $|R\rangle$ are long-lived states). What has happened is that the two lasers are driving their respective transitions exactly out of phase, and as a consequence, $|E\rangle$ is never populated.

Note that in the case of an atomic ensemble, both $|E\rangle$ and $|R\rangle$ are collectively excited states.

3.6 Rydberg EIT

Rydberg atoms are atoms with a large principal quantum number n. Due to the large polarizability, Rydberg atoms interact with a strong, long-range potential:

$$V(r) = -\hbar C_6/r^6 \tag{3.31}$$

where r is the distance between them and C_6 is the van der Waals coefficient.

The strong interaction is the origin of the Rydberg blockade, which prevents simultaneous excitation of two Rydberg atoms separated less than the blockade radius r_b. Under EIT with $|R\rangle$ chosen to be a Rydberg state, a single Rydberg excitation creates an effective exclusion zone within its blockade sphere within which all other atoms are out of resonance with the control laser. As a result, two photons cannot pass through each other if the blockade radius is greater than the attenuation length of the optical medium ($r_b > l_a$). Because $r_b \propto n^{11/6}$ and $l_a = (N\sigma_a)^{-1}$, the observation of the blockade effect requires a large principal quantum number and a high density of atoms. In other words, the optical depth per blockade radius $\mathrm{OD_b} = r_b/l_a > 1$.

This theoretical framework has been largely successful in describing Rydberg EIT experiments in free space, in which the probe laser sends out a series of pulses that then travel through an atomic ensemble with a slowed group velocity [14, 15]. When the pulses arrive in a Poissonian stream, one of them becomes a dark state $|D\rangle$, and all the others only see $|G\rangle \leftrightarrow |E\rangle$ and are thus scattered. This is the basis of the dark-state transmission suppression, which is the manifestation of the Rydberg blockade effect. The subsequent intensity correlation measurement with two photodetectors in a Hanbury Twiss-Brown setup has shown the transmitted light to be nonclassical with a sub-Poissonian and antibunching

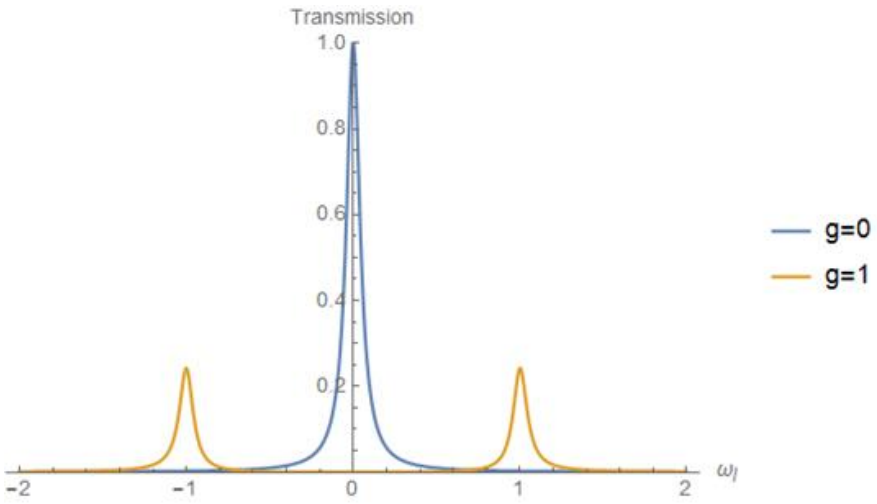

Figure 3.2: **Cavity transmission without the control laser: VRS** The transmission shows two dressed states split by $2g$. The result for $g = 0$ (empty cavity) is also shown. $\kappa = \Gamma = 0.1$

distribution.

The physics of Rydberg EIT in a cavity is distinctly different. A cavity "photon" is distributed over the entire cavity volume, so there is no propagation to speak of; the system is effectively a 0D polaritonic quantum dot [34]. While $\mathrm{OD_b}$ is enhanced by the finesse, to observe nonclassical light, it is also necessary to have a spatially thin atomic sample, requiring us to employ a spatially-selective depumping beam in the experimental sequence. We continue to explore the relationship between $g_2(\tau)$ and $\mathrm{OD_b}$.

3.7 Cavity transmission

Here we plot the typical cavity transmission of the atom-cavity system without and with the control laser, which exhibit the vacuum Rabi splitting and the electromagnetically induced transparency, respectively. For their calculations, see Appendix B.

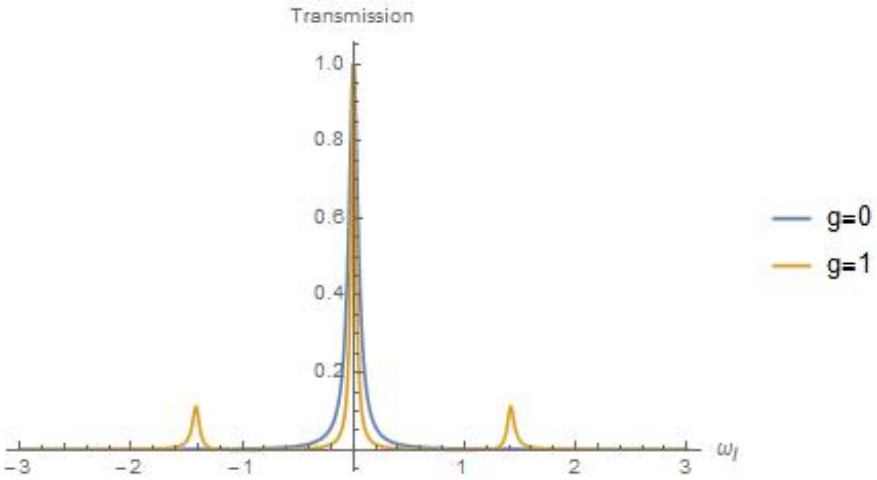

Figure 3.3: **Cavity transmission with the control laser: EIT** The transmission shows two broad bright states and one narrow dark state. The result for $g = 0$ (empty cavity) is also shown. $\kappa = \Gamma = 0.1$, $\Gamma_r = 0.01$

CHAPTER 4

CAVITY RYDBERG POLARITON EXPERIMENT

4.1 Introduction

Quantum simulations is currently a hot topic in the AMO community. Realizing model Hamiltonians in clean systems in order to study exotic phenomena occurring in real condensed matter materials is a job especially suited for AMO physicists, who routinely trap laser-cooled atoms in an optical lattice to study, for example, superconductivity [1].

For synthetic materials, the goal is no longer to simulate existing materials, but rather to engineer new systems and look for novel quantum effects in their own right. To this end, we want to build and study a material made of strongly interacting light. Ordinary photon-photon interactions are extremely weak, so we couple light to an atomic ensemble via electromagnetically induced transparency (EIT), where one of the levels is a Rydberg state. The strong, long-range dipole-dipole interactions between Rydberg atoms gives rise to the Rydberg blockade, which, when combined with the EIT transparency window, provides strong single-photon nonlinearity.

In this chapter, I describe our first observation of cavity Rydberg polaritons [35, 34]. The theory behind the optical cavity and the atom-cavity interaction appears in Chapter 2 and 3, respectively. Here I focus on the process of designing, building, and testing the experimental cavity and discuss the first experimental results.

4.2 Making the optical cavity

4.2.1 Cavity requirements

The heart of the experiment is the optical cavity responsible for strong coupling between the cavity light and an ensemble of laser-cooled ^{87}Rb atoms. There are three main requirements for the cavity:

1. Small waist size, on the order of 10 μm:

   A small waist size is essential for observing the Rydberg blockade, the signature of strong polariton-polariton interaction. Rydberg atoms with principal quantum number of $n \approx 100$ have the blockade radius of about 10 μm. Thus, to prevent two polaritons from sliding past each other in a transverse plane, we must restrict the cavity waist size to be comparable to the blockade radius.

2. Electric field shielding at the waist:

   The extraordinarily high polarizability of the Rydberg atoms that underlie the strong dipole interaction also makes them highly vulnerable to stray electric fields, which come from patches of dipoles on nearby surfaces. Because our polaritons' Rydberg component is a collective excitation of an atomic ensemble, any stray field and its spatial gradient directly translate to the shortening of the polariton's lifetime.

3. Degenerate modes:

   Having multiple cavity modes that are degenerate in frequency will be necessary for studying polariton-polariton scattering, which will in turn be the first step toward observing emergent crystallinity.

As we will see, the constraints imposed by the requirements on the cavity geometry are not mutually exclusive, especially in the cases of the small waist size and mode degeneracy, so we must pick and choose judiciously when designing the cavity. Other important experimental constraints are the limitations on the size and the location of the cavity inside the vacuum chamber.

4.2.2 Cavity geometry

A two-mirror confocal cavity, as noted in Chapter 2, is a simple and robust configuration in terms of beam alignment, but it has a rather large waist size for any reasonable cavity

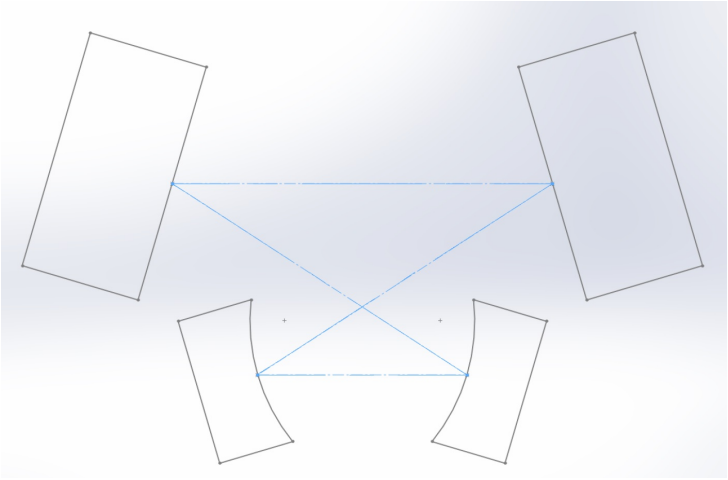

Figure 4.1: **Cavity geometry**. The closed, running-wave path of the cavity field, depicted here as a ray, follows a zigzag path and hits the centers of the mirrors with an AOI of 16.4°.

length. To achieve a 10-μm waist, the length of the cavity would have to be about 0.8 mm. Such a short cavity admits very little field of view for the loading of the atoms. One might try a spherical cavity, hoping to kill two birds with one stone (tiny waist size and totally degenerate modes), but it operates at the very edge of the stability region.

Our solution is to use a multi-mirror cavity. A running-wave configuration naturally offers extra narrowing of the waist size compared to a two-mirror, standing-wave configuration by effectively forcing the incident beam to start out focused (this is done by re-cycling the cavity field in a loop). To minimize astigmatism, we chose to have four mirrors.

The outline of the beam path is shown in Fig. 4.1. It is a bow-tie configuration symmetrical about a vertical line halfway between the two pairs of mirrors. The lower mirrors have the radius of curvature (ROC) of 10 mm, and they are separated by about 11 mm. The upper mirrors have 500-mm ROC and are separated by 20 mm. The perpendicular distance separating the pairs is 6 mm, so that the total length of the cavity is about 68 mm.

The stability of the cavity can be determined by looking at its waist size. Our cavity has two waists: a large waist between the upper mirrors and a small waist between the lower mirrors. We focus on the small waist where the atoms will be loaded. Due to the non-zero angle of incidence (AOI) of the beam on the mirrors, the waist sizes along the x-

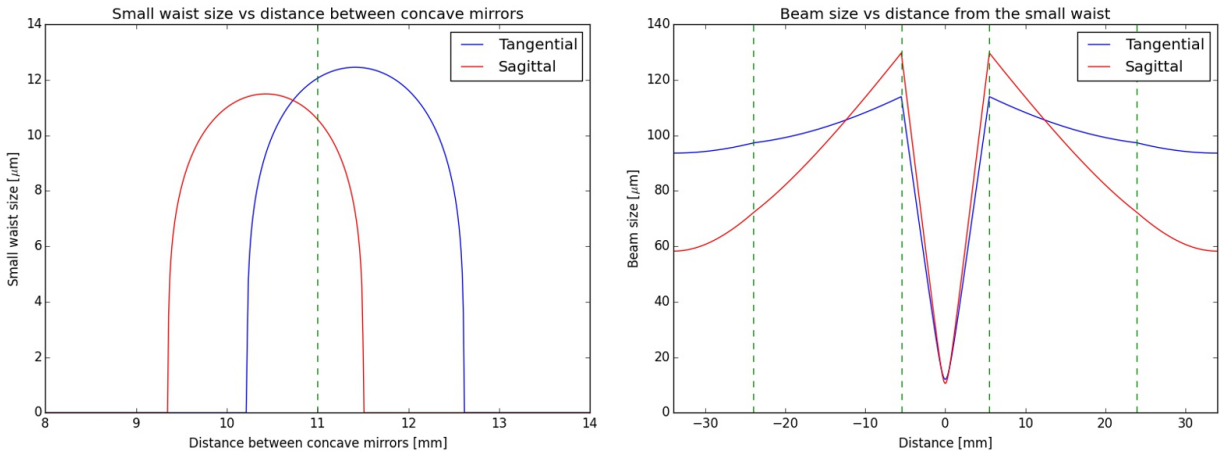

Figure 4.2: **Cavity stability**. (left) Waist size for x-axis (red, sagittal) and y-axis (blue, tangential) as a function of the distance between the lower mirrors. The overlapping region is where the cavity is stable. (right) Beam size vs. distance relative to the small waist. The small waist is about 10 μm x 12 μm and the large waist is about 60 μm x 90 μm.

axis and the y-axis are different. As a result, the modes are described by separate q_x and q_y parameters, obeying separate ABCD matrices (this is the case for "orthogonal" astigmatism, which applies to our planar cavity).

The size of the x-waist and the y-waist as a function of the distance between the lower mirrors is plotted in Fig. 4.2. An astigmatic cavity is stable only if both the x-waist and the y-waist are non-zero; hence, according to the plot, our cavity admits a small region of stability around the distance of 11 mm. Figure 4.2 also shows the beam size of a TEM_{00} mode as a function of the distance away from the small waist for a fixed distance of 11 mm between the lower mirrors.

The astigmatism also affects the Gouy phase, which in tun affects the transverse mode spacing. Figure 4.3 shows the resonant frequencies of the TEM_{mn} modes, relative to the frequency of the TEM_{00} mode, again as a function of the distance between the lower mirrors. Note that there is a special distance for which the ratio of the y-Gouy phase over the x-Gouy phase is a rational fraction, leading to a degeneracy for $\text{TEM}_{m,n+2} = \text{TEM}_{m+1,n}$. Moreover, it turns out that this distance is also the distance where the x-waist and the y-waist have the same size. Thus, any stable running-wave cavity must necessarily possess such a degenerate

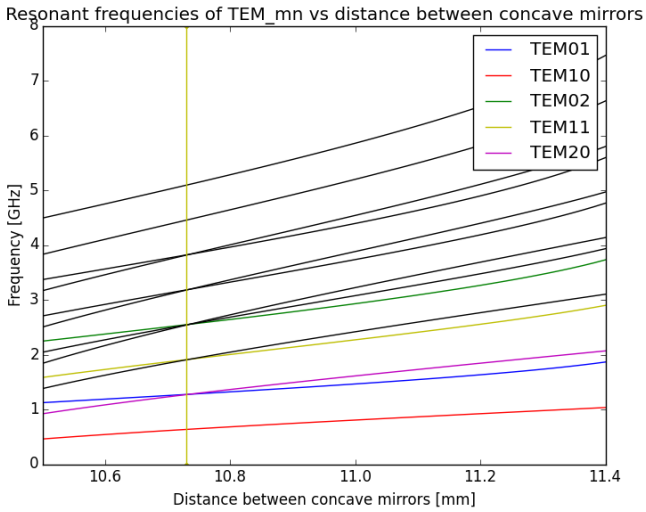

Figure 4.3: **Transverse mode frequencies vs distance between the lower mirrors**. The frequencies are relative to that of TEM_{00}. At the distance of 10.7 mm, different TEM_{mn} modes start to cross. Unlabeled high-order modes in the sequence are also shown.

configuration. We tune our cavity to this length of 10.7 mm.

4.2.3 Cavity construction

Spacer

A 3D model of the cavity was drawn up using SolidWorks, as shown in Fig. 4.4. The spacer, the material that holds the mirrors in place, would be made of type 316 stainless steel (generally known to be the least magnetic type). Four tunnels are bored for the mirrors. The mirrors, once inserted into the tunnels, are held tightly against the embankments with pushers from behind. The tunnels were only about 70% enclosed, leaving the tops open, in order to facilitate plugging the mirrors in and out of the tunnels.

The spacer is asymmetric in the direction perpendicular to the cavity plane. The side where the tunnel tops are exposed has most of the material near the beam path removed. The opposite side has a deep groove so that a heating wire can wrap around the spacer. By supplying current through the wire, we can heat and expand the spacer over about 5λ, which is an extremely sensitive means of tuning the cavity length.

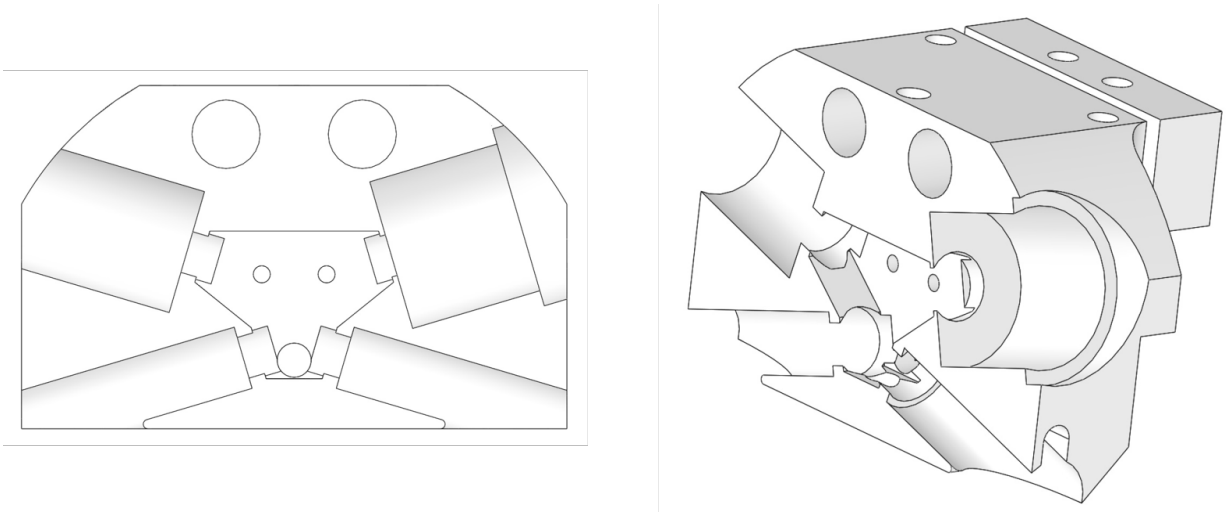

Figure 4.4: **Model of the cavity**. (left) Front view. (right) Angled side view.

Initial cavity designs were quickly tested by use of a 3D printer (Flashforge Creator), which allowed rapid prototyping with successive design tweaks; see Fig. 4.5. Successful tests with the plastic cavity were followed by a stainless steel cavity machined by an external vendor (Owens Industries). When the finished cavity arrived, the tolerance for the tunnel diameters turned out to be slightly off by about a half of a thousandth of an inch, so we milled down the tunnels via lapping with a fine mud solution in the student machine shop.

Mirror preparation

For the lower mirrors, the substrates were made by Laseroptik and the optical coatings were applied by Advanced Thin Films. For the upper mirrors, both the substrates and the coatings were from Laseroptik. Extreme caution was taken to treat the mirrors, especially the ultrahigh reflective lower mirrors, with utmost care so as not to spoil their finesse. Any dust spotted on the surface was gently removed with an air blower. Other residues were removed either with a liquid polymer or an application of acetone and methanol, although it is unclear if these methods were successful. It is fair to say that mirror reflectivity is a more or less sacred quantity.

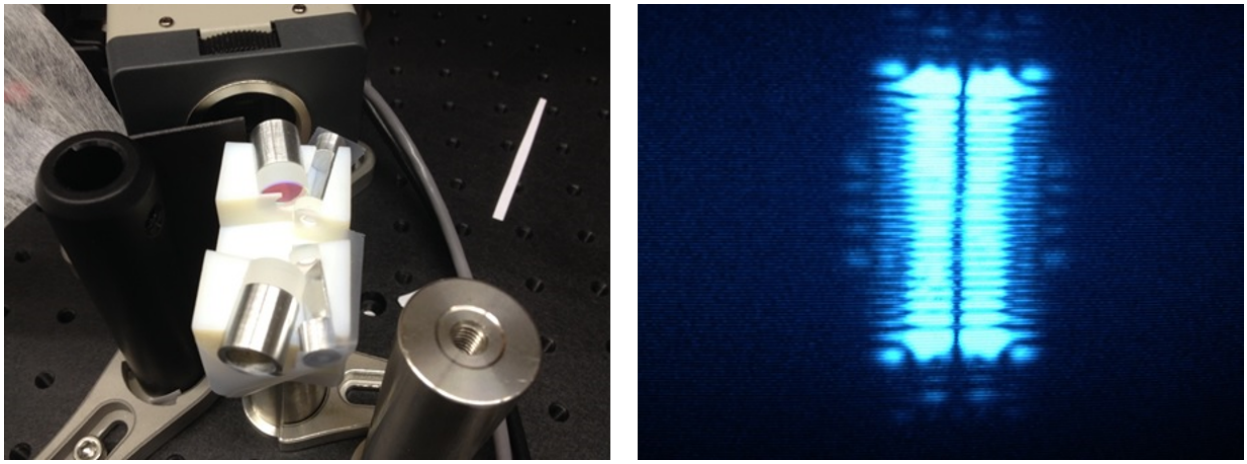

Figure 4.5: **Plastic cavity**. The cavity design went through rapid prototyping with a 3D printer. (left) A plastic cavity with mirrors inserted. (right) An example extremely high transverse mode transmitted out of the cavity and captured on a camera.

Piezoelectric transducer

In order to be able to tune the cavity length, one of the upper mirrors is mounted on piezoelectric transducer (PZT). We manually ground the height of the 10-mm-diameter, ceramic piezo with a sand paper from 10 mm to 5 mm, so that the overall cavity structure would fit within the allowed volume inside the vacuum chamber. Vacuum wires were attached onto the inner and outer surfaces of the piezo. During the experiment, applying a high voltage to the piezo would allow us to scan the cavity length over more than one free spectral range. See Fig.4.6 for the photograph of the piezo-mounted mirror in the cavity.

4.2.4 Electric field filter

We have pointed out the importance of mitigating the effect of the stray electric field on the atoms. Initially, we believed that the biggest source of the field would be the piezo, since we would be applying to it up to 1 kV. Thus, we chose to surround the small waist with a stainless steel "efilter" with 1-mm-wide tunnels for the intracavity beams.

The actual physical location of the 10-μm waist is not precisely known, due to the machining tolerances of the cavity. In order to find it, we churned out myriad 3D-printed plastic

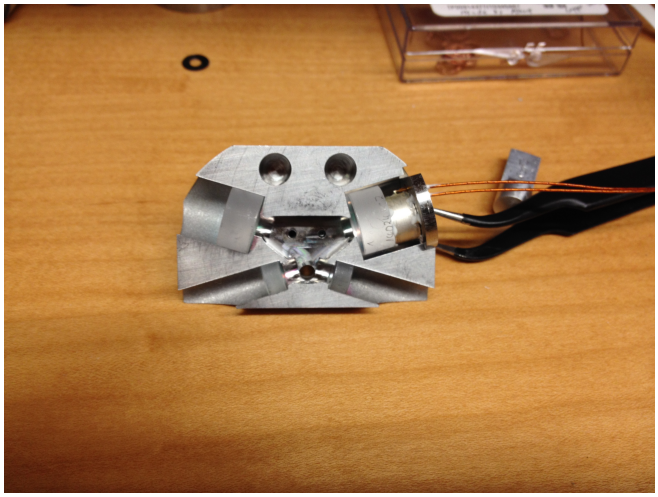

Figure 4.6: **Inserting the mirrors into the spacer**. The upper right mirror has been epoxied to a piezo, and the piezo to a stainless steel wafer, and the wafer to the spacer.

efilters that covered a large parameter space of various widths, heights, and lengths of the efilter, centered at an unknown coordinate relative to the fixed features of the spacer. We eventually selected a design that did not affect the cavity finesse, i.e., it did not cut off any portion of the intracavity Gaussian beam. The final efilter, made of stainless steel, was machined in the student machine shop using the CNC.

We pre-empt the experimental results discussed later to state that this efilter design did not work as it gave us a large EIT linewidth. It turns out that the stray electric fields come from any nearby surface, even metallic, due to the adsorption of rubidium atoms that fill the whole vacuum chamber ("They are like sand... they get everywhere," according to our postdoc). The build-up of atomic dipoles on the surfaces was exasperated by the fact that the atoms were so close to the efilter walls.

After the initial experimental runs, we removed the efilter and replaced it with a PCB board with metal pads, the idea being that the voltages applied to the pads could be used to cancel the fields. The resulting EIT signal was significantly better, though still not narrow enough to observe nonlinearity (g_2). Finally, a second-generation cavity was built, where the focus was on having the waist far away from any surface. The EIT result discussed later comes from this second-generation cavity (picture not shown).

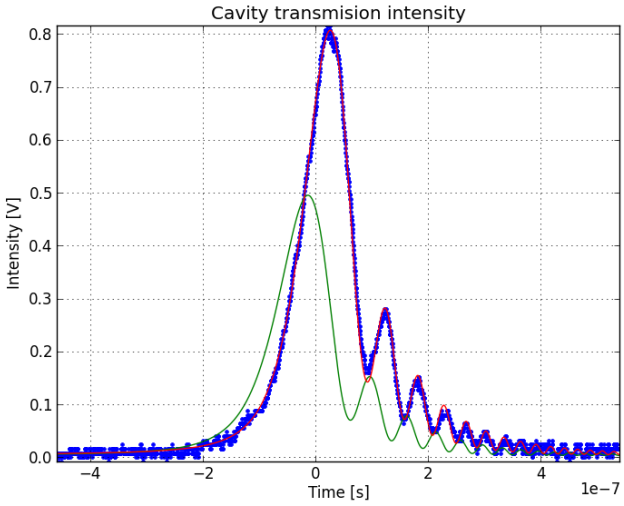

Figure 4.7: **Cavity ringdown**. The cavity ringdown spectrum can be fit to obtain the finesse of the cavity. To get the spectrum, we quickly scan across the cavity resonance, either with the laser or the cavity piezo. The cavity transmission then exhibits a series of constructive and destructive interference from the light leaking out of the cavity, all within an envelope of exponential decay.

4.2.5 Characterization

Once assembled, we tested the cavity outside the vacuum chamber and measured its finesse. After mode-matching into the cavity, we performed a ringdown measurement [36] and measured the fineese to be about 2500. Figure 4.7 shows a typical cavity ringdown spectrum.

To tune the cavity length to the degeneracy point, we inserted thin sheets of stainless steel, cut into annular rings, between the lower mirrors and the embankments, increasing the mirror separation. Once the mirrors were glued, we further tuned the cavity length with the heating wire until TEM_{01} and TEM_{20} modes became degenerate. Figure 4.8 shows the cavity transmission of the degenerate pair of modes captured by a CCD camera.

We also measured the polarization of the transmitted light and saw that it was 97 % right-handed and 3 % left-handed circular. The circular polarization of the cavity field was unexpected, but it pointed to our cavity being slightly nonplanar, probably due to the free-hanging, piezo-mounted mirror drooping under gravity. This drooping would later cause 20 MHz difference between the resonant frequencies of TEM_{01} and TEM_{20}.

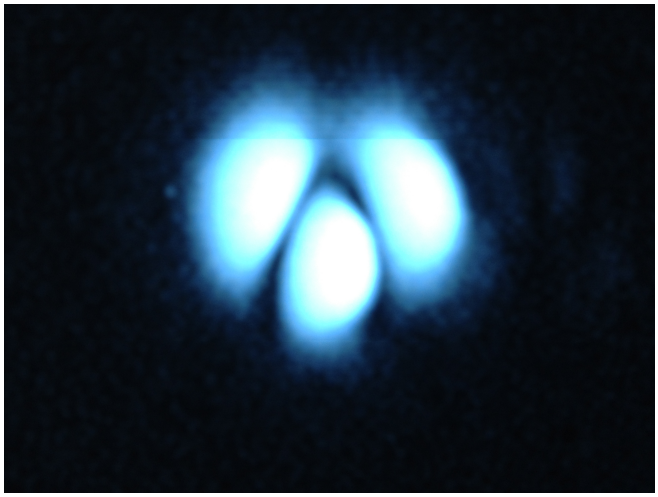

Figure 4.8: **Degenerate $\mathbf{TEM}_{01}$ and $\mathbf{TEM}_{20}$.** The degeneracy appears in the camera as the interference of cavity fields rather than intensities.

Finally, the entire structure was mounted to a vacuum chamber flange and placed inside the vaccum chamber; see Fig. 4.9.

4.3 Experimental sequence

Before the start of an experimental run, we turn on the getters, which proceed to fill the vacuum chamber with rubidium atoms. Then, we stabilize the cavity length to a 1560-nm transfer laser, which can be tuned near the atomic transition (see Appendix C for cavity locking). The transfer laser itself is locked to an ultrastable glass cavity housed in a specialized chamber. The getters, when first turned on, proceed to heat up the cavity structure, which subsequently expands and shifts the cavity resonances. It takes about four hours for the cavity to reach an equilibrium temperature, at which point we perform our measurements (later we installed an infrared laser in a feedback loop to significantly reduce this waiting period).

Each sequence begins by loading the magneto-optical trap (MOT), which collects ^{87}Rb atoms from the surrounding vapor gas at the center of the vacuum chamber. Then, a crossed dipole trap (a moving 784-nm standing wave formed from a retro-reflected beam), acting as

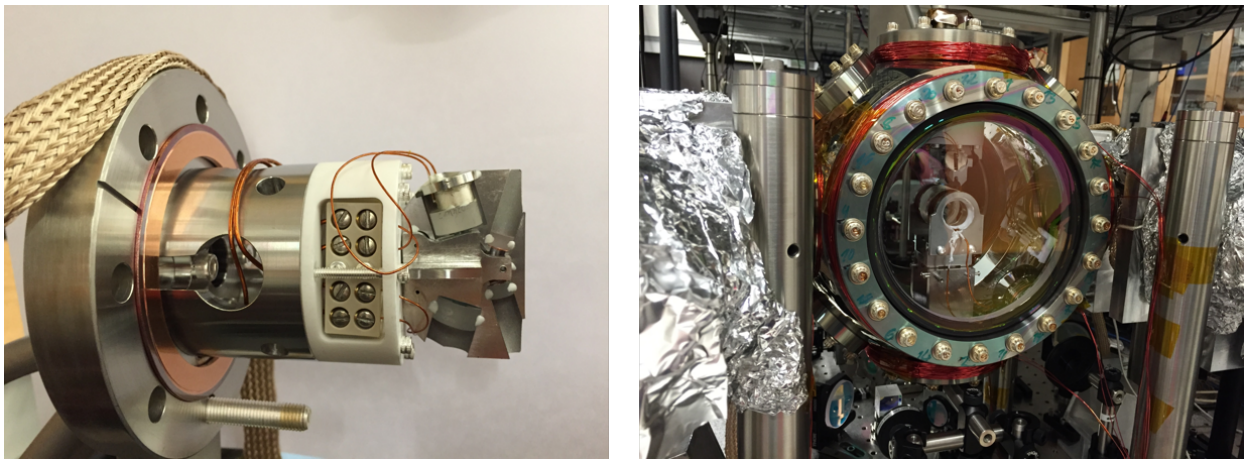

Figure 4.9: **Cavity assembled and mounted**. (left) The cavity was mounted to the vacuum chamber flange through a macor piece for electrical isolation. (right) The cavity mounted above the MOT coils inside the vacuum chamber.

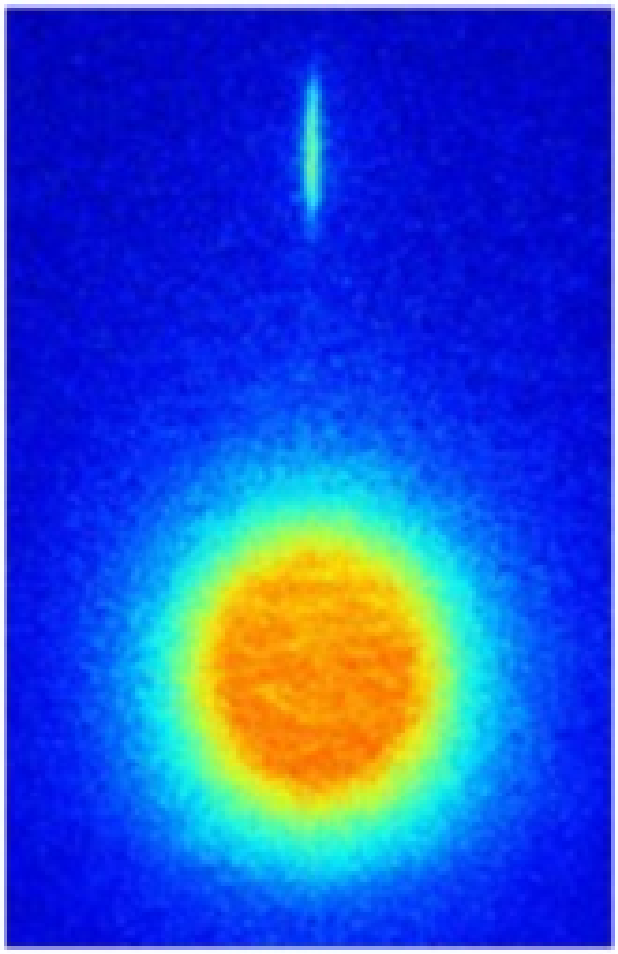

Figure 4.10: **Florescence image of the atoms**. Both the MOT and the sample of atoms in the optical conveyor belt are shown.

an optical conveyor belt, vertically transports a sample of the laser-cooled atoms, about 10^5, up into the small waist of the cavity, located 27 mm above the MOT. See Fig. 4.10 for the fluorescence image of the atoms in the conveyor belt and the MOT.

Once the atoms are in the small waist, the control beam is turned on, and the probe beam is swept across the atomic transition over 1 ms. The transmitted light is then collected and measured by a single-photon counting module (SPCM), or two SPCMS in a Hanbury Brown-Twiss setup in the case of the $g_2(\tau)$ measurement.

In order to observe single-photon nonlinearity, a vertical "slicing beam" with a TEM_{10} spatial profile is shone on the atoms in the small waist before sweeping the probe beam. The slicing beam selectively depumps all atoms in the profile to the $F = 1$ state and leaves only a thin slice of atoms in the $F = 2$ state, ensuring that the atomic ensemble is within the Rydberg blockade volume.

4.4 Experimental results

Our experimental probe is the transmitted light from the cavity. We couple the 780-nm probe laser through an upper mirror and observe the light coming out of the other upper mirror. The 780-nm probe laser is tuned to the D2 transition of ^{87}Rb, driving the atoms from $|g\rangle = |5S_{1/2}, F = 2, m_F = 2\rangle$ to $|e\rangle = |5P_{3/2}, F = 3, m_F = 3\rangle$. The counter-propagating control laser, entering through a lower mirror, couples $|e\rangle \to |r\rangle = |nS_{1/2}, J = 1/2, m_J = 1/2\rangle$. For $|r\rangle$, we worked mostly with $n = 40$. See Fig. 4.11 for the cavity diagram and the 3-level atomic energy ladder.

4.4.1 Vacuum Rabi splitting

When the atomic ensemble is probed with only the probe laser and without the control laser, the characteristic vacuum Rabi splitting (VSR) is observed, indicating strong atom-cavity coupling. Figure 4.12 shows a 2D plot of a series of VRS as a function of the vertical

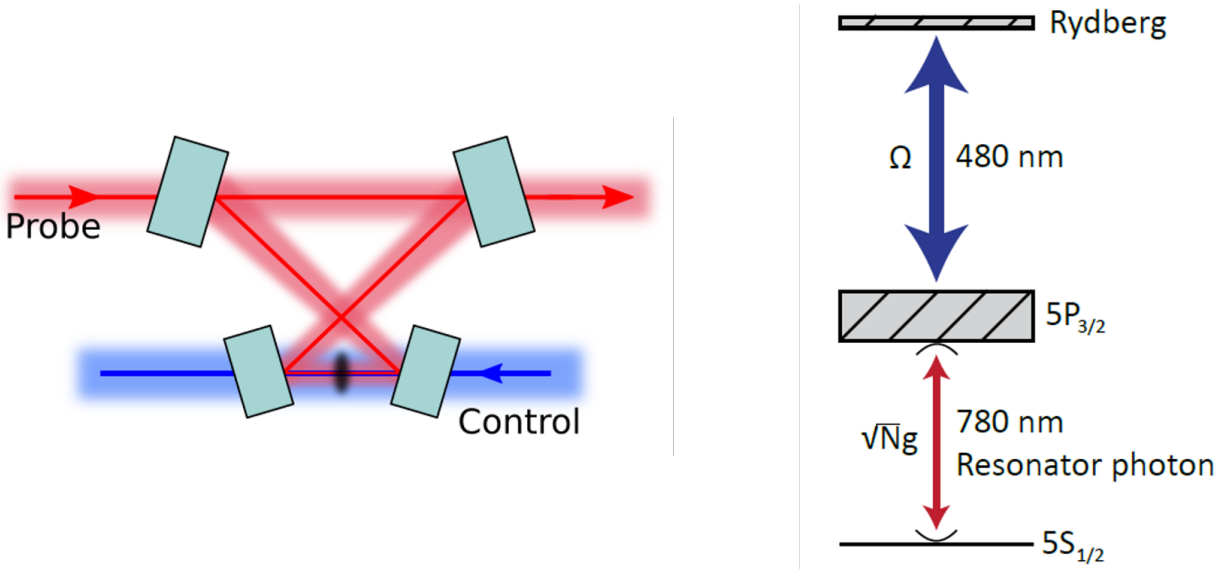

Figure 4.11: **Experimental lasers and energy level diagramt**. (left) The probe beam and the control beam counter-propagate to minimize Doppler broadening. (right) The energy level diagram of the atoms. The thickness of the level represents the linewidth (inverse lifetime).

transport distance and the probe laser detuning. Split modes appear whenever the atoms, carried by the optical conveyor belt, cross the light, occurring at both small and large waists as well as another crossing point in between. The inset shows the result of parking the atoms in the small waist and detuning the cavity as the probe laser is swept. The shift in the frequencies of the VRS peaks demonstrates the avoided crossing between the dressed modes, as predicted from Chapter 3.

Fitting to the VRS gives the collective vacuum Rabi frequency $G = g\sqrt{N}$. From knowing the single atom-cavity Rabi frequency g from the cavity parameters, we can calculate the number of atoms participating in the collective excitation.

4.4.2 EIT

When the control laser is turned on, the atomic ensemble undergoes the EIT transition as the probe laser is swept. Figure 4.13 shows a typical cavity transmission with three eigenstates: two broad bright-state polaritons and one narrow dark-state polariton. The composition of

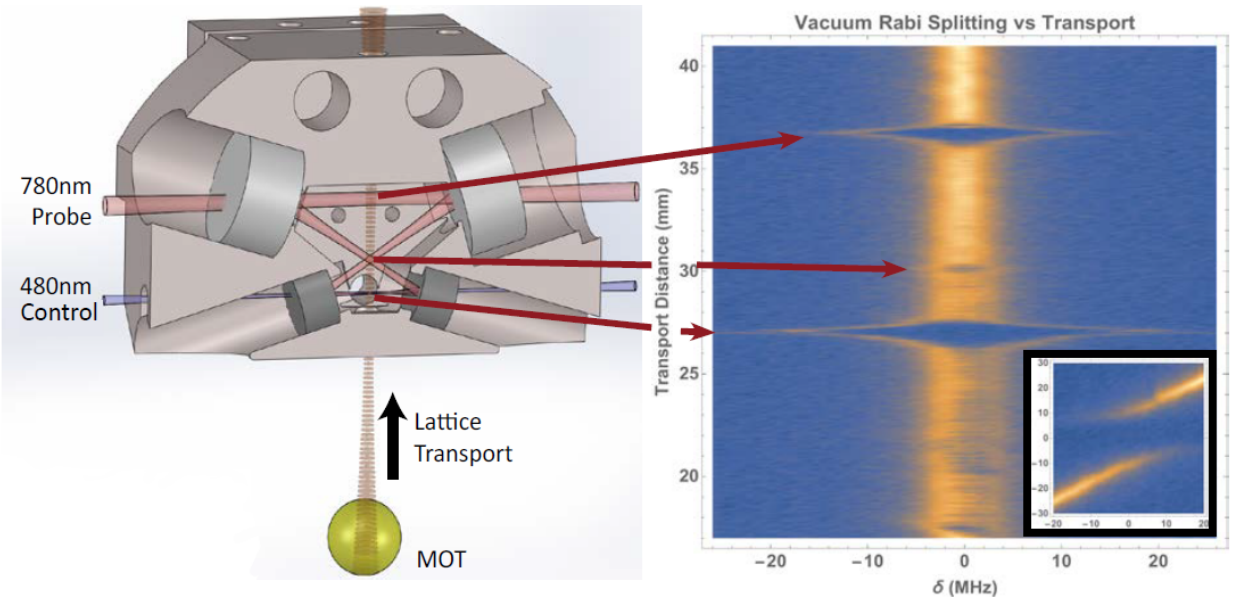

Figure 4.12: **VRS**. The VRS cavity transmission vs. vertical transport distance shows VRS at three locations: two waists and a cross point in the middle.

the dark state is given by

$$|D\rangle = \cos\theta\,|G\rangle - \sin\theta\,|R_c\rangle \tag{4.1}$$

where the dark-state rotation angle $\theta \equiv \tan^{-1} G/\Omega$ (see Chapter 3). Thus, by controlling the ratio of the probe and control laser intensities, we can decide to what extent the polariton is a Rydberg excitation and to what extent it is a cavity photon.

We then explored the EIT spectrum as a function of the cavity detuning. Figure 4.14 shows a 2D plot of a series of EIT signals, where each vertical slice is the cavity transmission of the probe laser. As the cavity is detuned, the bright polaritons shift just as the VRS states do, since they are mostly comprised of cavity photons. The shift of the dark polariton, however, is noticeably smaller. This is the "compression" of the dark-state polariton spectrum, indicative of the slowdown of dynamics due to their atomic component.

Following Equation 4.1, the energy and the inverse lifetime of the dark-state polariton to

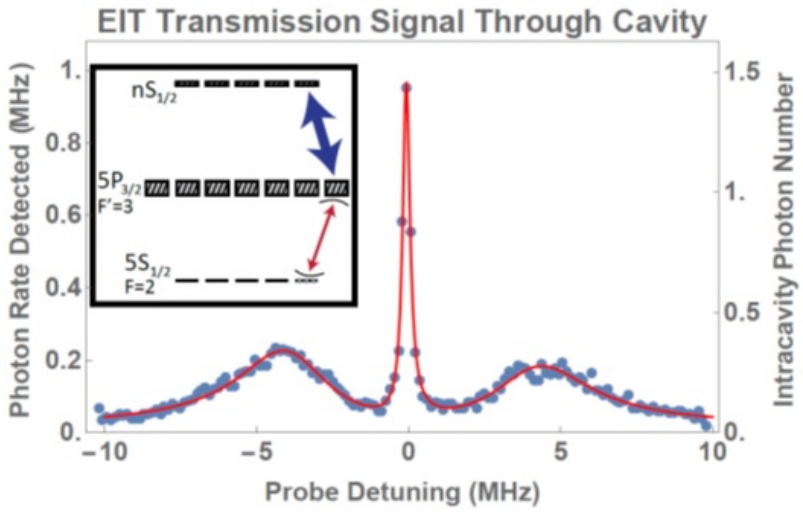

Figure 4.13: **EIT**. The EIT signal shows the characteristic broad bright-state polaritons and a narrow dark-state polariton.

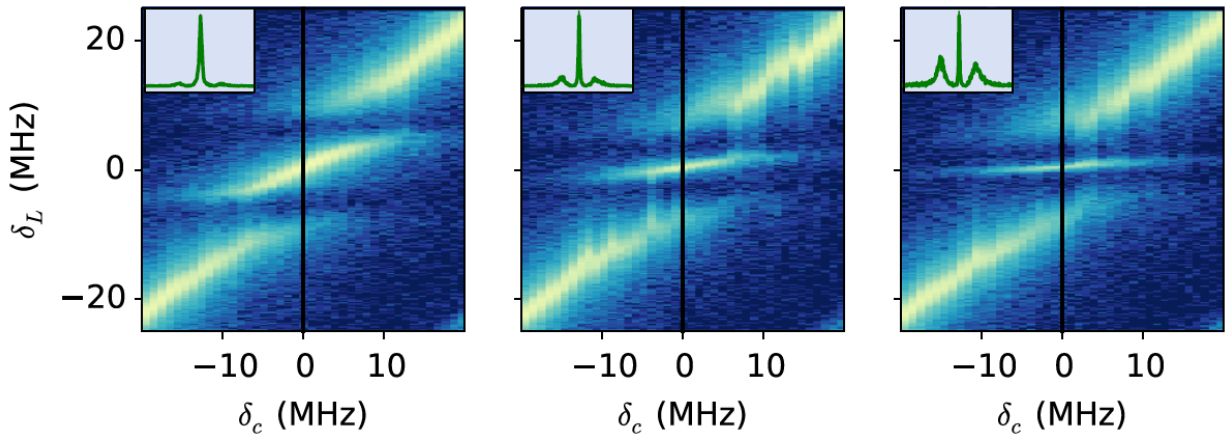

Figure 4.14: **EIT spectra vs cavity detuning**. As the cavity is detuned, the dark polariton energy shifts. (left to right) dark-state rotation angle = 43, 62, and 72 degrees. The insets show the EIT spectrum at zero cavity detuning, as in the previous figure.

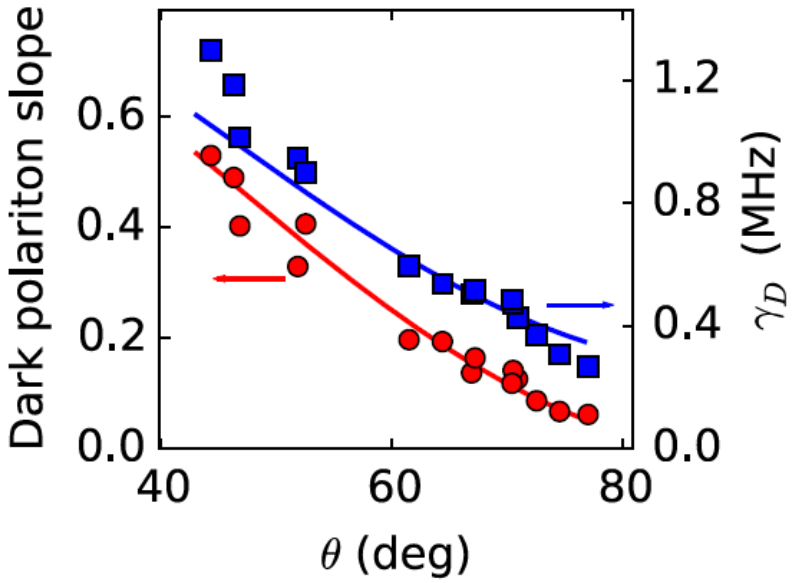

Figure 4.15: **Energy and lifetime vs. dark-state rotation angle**. Both the frequency shift and the inverse lifetime are proportional to the slope of the dark polariton's shift vs. cavity detuning, $\cos^2\theta$.

first order are given by

$$\delta_D \approx \delta_c \cos^2\theta + \delta_R \sin^2\theta \tag{4.2}$$

$$\gamma_D \approx \kappa \cos^2\theta + \gamma_R \sin^2\theta \tag{4.3}$$

where $\delta_{c,R}$ are the detunings and κ, γ_R are the inverse lifetimes of the cavity and the Rydberg level, respectively. Figure 4.15 shows the slope for the dark-state frequency shift, as well as the inverse lifetime, as a function of the dark-state rotation angle. That the experimental results and the theoretical predictions agree very well attests to that fact that the cavity Rydberg polaritons are truly composite particles.

Finally, we tuned the cavity to the degeneracy near the TEM_{10} and TEM_{02} degeneracy point and observed the cavity transmission using a multi-mode fiber. Individually, the cavity modes are 20 MHz apart. Figure 4.16 shows that the dark polaritons are separated by much less than this difference, again due to the compression from strong matter-light mixing. In this case, $\Delta\delta_D \approx \Delta\delta_c \cos^2\theta = 2.3$ MHz.

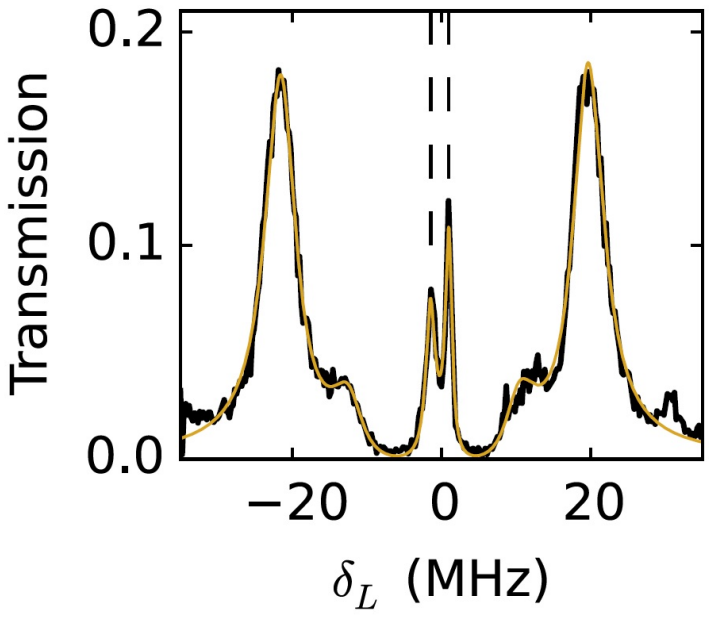

Figure 4.16: **Multimode EIT with TEM$_{10}$ and TEM$_{02}$.** The spectrum shows that dark polariton energies from the TEM10 and TEM02, whose cavity components are separated by 20 MHz, have been pulled in much closer, due to the frequency compression, to about 2.3 MHz. The two bright polaritons from each of the modes can also be seen in the spectrum.

4.4.3 Photon statistics: $g_2(\tau)$

The smoking gun for single-photon nonlinearity is in the coincidence measurement of the intensity correlation function $g_2(\tau)$. Our initial measurement revealed no such nonlinearity, since there was too much inhomogeneous broadening from the stray electric fields and we could only reach about $n = 40$ for the Rydberg level. In the second-generation cavity, we improved the design by replacing the previous efilter and keeping the atoms as far away from any surface as possible. The resulting $g_2(\tau)$ measurement for $n = 100$ is shown in Fig. 4.17. At $\tau = 0$, g_2 is less than 0.3. The g_2 signal shows both sub-Poissonian statistics ($g_2(0) < 1$) and anti-bunching ($g_2(0) < g_2(\tau)$), which point to the production of explicitly non-classical light.

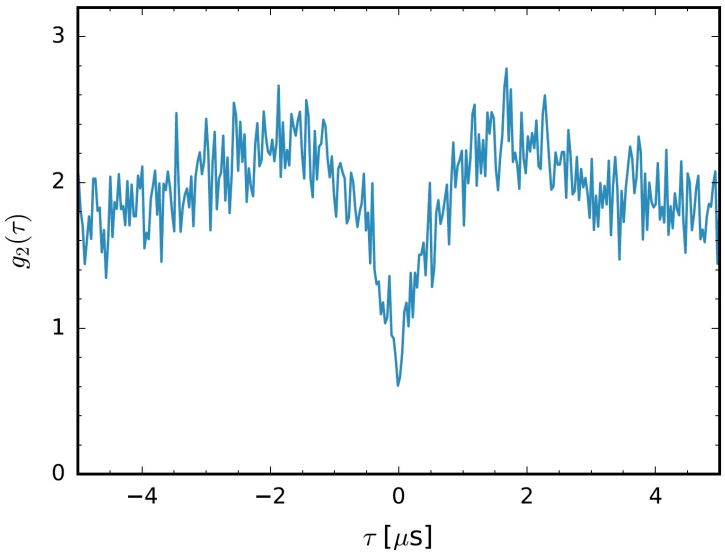

Figure 4.17: **Measurement of $g_2(\tau)$.** Whereas the characteristic dip has been observed in several free-space Rydberg EIT experiments, this is the first such observation in an optical cavity.

4.5 Conclusion

The real power of an optical cavity is in its modes! It is the degeneracy of modes that gives rise to manybody physics. Our demonstration of multimode EIT in our first cavity and single-photon nonlinearity in the second sets the stage for the study of polariton-polariton scattering and other multimode, quantum nonlinear physics. For instance, if we inject light into one mode of the cavity, what will the transmitted light look like? Of course, the key to preserving the polaritons intact as they interact is the strong coupling, which we have achieved in our cavity.

The measurement of spatial g_2 in a degenerate cavity can reveal how the polaritons with strong, long-range interactions organize themselves. The spatial order that appears for a small number degenerate modes is one that has been imposed externally. To observe spontaneous crystallization, we require large degeneracy. This will mean we would need a slew of new technology for mode injecting, mode sorting, high-spatio-temporal-resolution imaging, etc. The subject of mode injecting will be discussed in the next chapter.

Another interesting idea is to make a twisted cavity, where the degenerate Laguerre-Gauss

modes can be mapped to a Landau level, a topic also covered next. The combination of the Landau level with interaction from Rydberg polaritons points the way to experimentally probing fractional quantum Hall physics. Exciting opportunities lie ahead!

CHAPTER 5
PROBING THE CAVITY WITH A HOLOGRAPHIC SPATIAL LIGHT MODULATOR

5.1 Introduction

The ability to transform one field of light into another is an important tool with wide-ranging applications. For instance, during the cavity Rydberg experiment in Chapter 4, we used a phase plate to convert a fundamental TEM_{00} into the TEM_{10} "slicing" beam. Other possible examples of beam shaping include creating a blue-detuned, donut-shaped field for trapping atoms or injecting light into a specific transverse mode of an optical cavity. It is with the latter application in mind that we implement a spatial light modulator.

Phase plates and photographic films have long been used for wavefront manipulation, but swapping them in and out of fast-evolving experiments is tedious and labor-intensive. More importantly, optical aberrations that distort the wavefront are almost always present in any physical setup, and they must be compensated to produce the diffraction-limited result - a task difficult to accomplish with phase plates alone. A better solution is to employ an electronically controllable spatial light modulator (SLM), whose pixels can be switched on or off individually. It is this robustness that allows SLMs to be used holographically, combining beam shaping [37] and adaptive optics [38] in a single device.

In this chapter, I describe the implementation of a digital micromirror device (DMD) as a holographic SLM and its application for coupling light into optical cavities. The phase-correcting procedure is based on the prior work demonstrated for a quantum gas microscope by the Greiner group [39]. After explaining how to make bitmap holograms and compensate for optical aberrations, I present the results of the DMD-based cavity mode injector. Finally, I give a brief overview of one major application of the work in creating synthetic Landau levels for cavity photons [40].

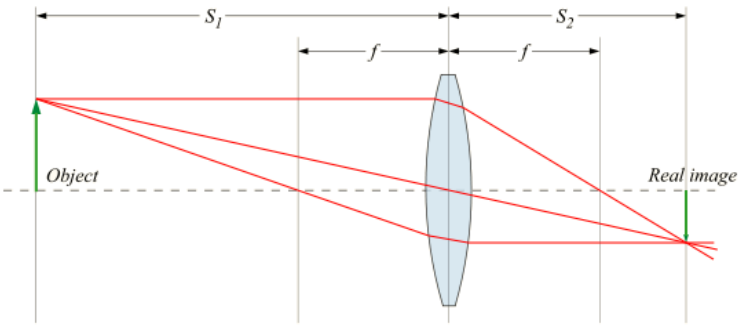

Figure 5.1: **Imaging with in ray optics.** The thin lens formula in imaging with a converging lens is a small-wavelength approximation ($\lambda \to 0$) that ignores diffraction. Image from Wikipedia.

5.2 Beam shaping with the DMD

5.2.1 Some Fourier optics

Beam shaping, which transforms one complex field into another, is closely related to imaging, which is a mapping between an "object" and an "image". In ray optics, the mapping between the intensities, located at the object plane and the image plane of a thin converging lens, is given by

$$I(\vec{x}_o) \to I(\vec{x}_i) = I(m\vec{x}_0) \tag{5.1}$$

where $\vec{x}_{o,i}$ denote the coordinates of the object and the image, and the magnification is given by $m = -S_2/S_1$; see Fig. 5.1. The image is an exact reproduction of the object with only a change in scale.

Of course, a fundamental aspect of light is diffraction, and as such the propagation of light through an optical system is more accurately handled by the Kirchhoff diffraction theory, which embodies the Huygens-Fresnel principle of the primary wave and secondary wavelets. Another language that describes diffraction is Fourier optics, which takes advantage of the fact that an optical system is both linear and space-invariant. In particular, a thin lens

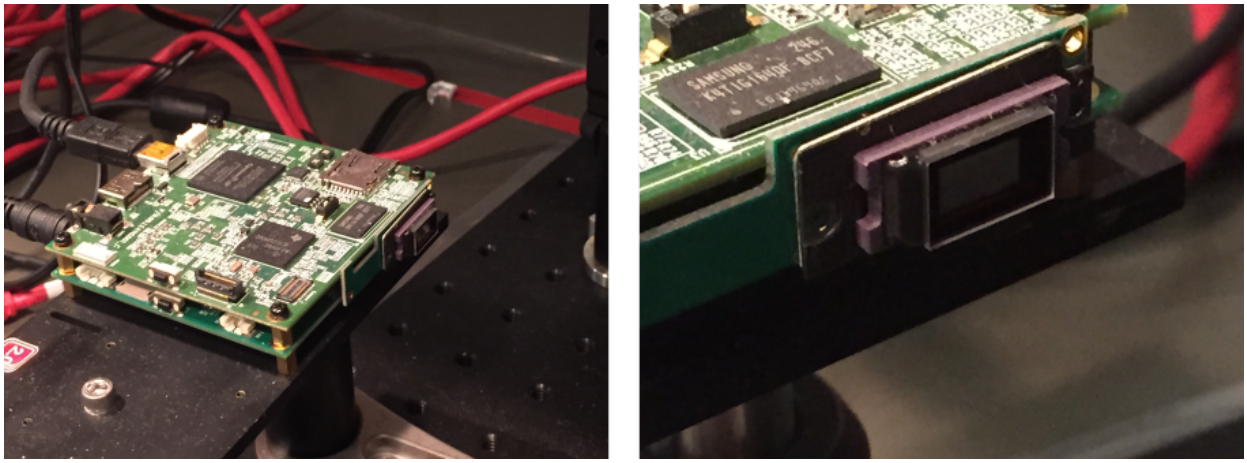

Figure 5.2: **Photographs of the DMD.** The DMD consists of tiny mirrors on a 6.6 mm x 3.7 mm chip. (left) It comes packaged as part of Texas Instruments DLP3000; some disassembly is required to expose the chip itself. (right) Closer view of the chip.

performs a 2D Fourier transformation:

$$g(x,y) \to G(f_x, f_y) = \mathcal{F}\{g\} = \int g(x,y) e^{-2\pi i(f_x x + f_y y)}\, dxdy \tag{5.2}$$

where g and G are the complex fields at the "Fourier plane" and the image plane, respectively, located one focal length away on either side of the lens. Thus, creating a desired beam profile requires calculating its inverse Fourier transform and "displaying" it - via a spatial light modulator - on the Fourier plane.

5.2.2 Digital micromirror device

The DMD (Texas Instruments DLP3000) is a 2D array of 684 x 608 square micro-electro-mechanical aluminum mirrors, with a side length of 7.6 μm. Each mirror is held by a yoke that orients it in either of two angled positions at ± 12 degrees. The tilted positions, maintained by electrostatic forces, indicate either "on" or "off". Unlike liquid crystal displays, the DMD mirrors do not require refreshing, thus offering a truly static image - an important criterion in many atomic physics experiments. See Fig. 5.2 for the photographs of our DMD and Fig. 5.3 for a cartoon model of a single mirror of the DMD.

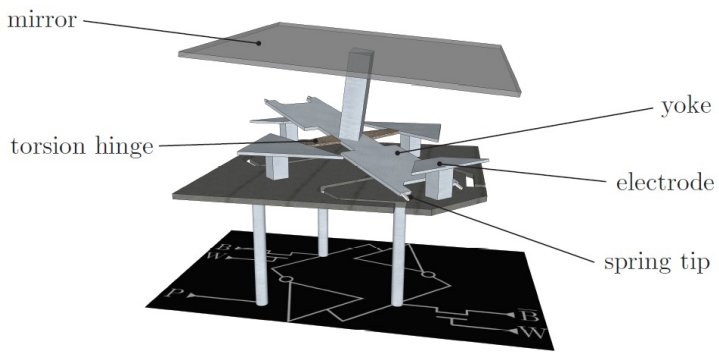

Figure 5.3: **Cartoon model of one DMD mirror.** The 7.6 μm x 7.6 μm aluminum mirror is held by a mechanical yoke, which fixes it at $\pm$ 12 degrees. Image from Ref. [41].

5.2.3 Holographic spatial light modulation

Although at first glance it seems impossible for the DMD, which can only display a binary amplitude image, to produce a complex field, this can be done with holography. Figure 5.4 shows how 1D gratings can modulate both the phase and the amplitude of the incident plane wave. Constructive interference occurs when the grating slits have their phases separated by an integer number of 2π. Shifting the locations of the grating slits correspondingly shifts the phase of the outgoing beam, while the width of the slits affects its intensity. Finally, changing the grating's periodicity changes the outgoing beam's direction.

The procedure for creating a hologram is as follows. First, we calculate the complex field whose Fourier transform would give us the desired beam profile in the image plane. The phase of the field becomes encoded in the phase of the grating via

$$g(x, y) = \cos(k_x x + k_y y + \phi(x, y)) \tag{5.3}$$

where x, y refer to the individual mirror coordinates on the DMD.

It remains to bring forth the actual gratings to life by deciding which mirrors should be on and off. The straightforward way is to compare the grating phase to the re-scaled field amplitude:

$$p(x, y) = |k_x x + k_y y + \phi(x, y)| \leq w(x, y) \tag{5.4}$$

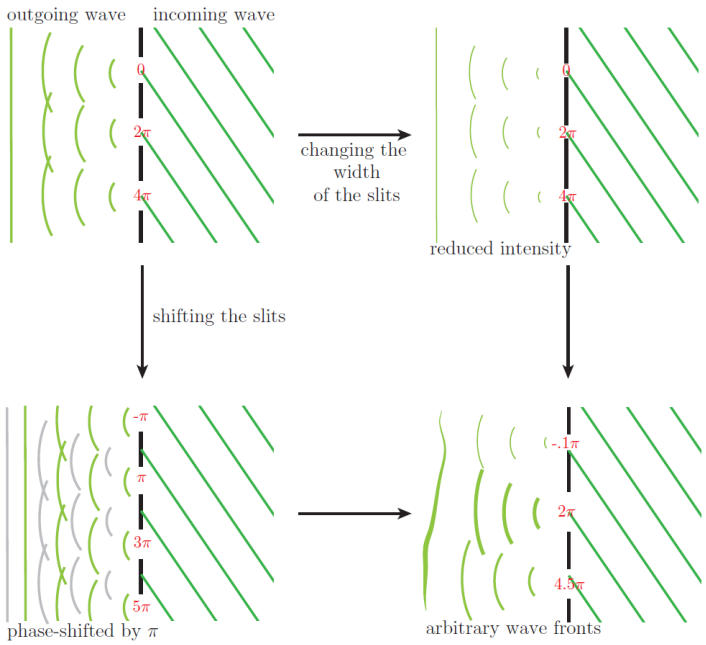

Figure 5.4: **Holography with 1D gratings.** Gratings can be used to modulate both the phase and the amplitude of the incident light. Image from Ref. [41].

where p is a binary map. Actually, because the individual mirrors have a finite size, the above equation introduces two errors: the grating effects from the mirrors themselves and a limit to the maximum spatial resolution. Instead, we employ the following probability function (see Ref. [41]), which tends to smooth out the distribution of on/off mirrors:

$$\text{Prob}(x,y) = \frac{1}{2}\left[\tanh(a[\phi(x,y) + w(x,y)/2]) + \tanh(a[w(x,y)/2 - \phi(x,y)])\right] \tag{5.5}$$

where a determines the sharpness of the grating slits.

5.2.4 Initial beam shaping test with LG modes

The DMD can produce arbitrary phase features such as phase steps and vortices, which are required to make higher-order Hermite-Gauss or Laguerre-Gauss modes. The equation for the LG modes is

$$LG_p^l(r) \propto r^{|l|} L_p^l\left(2\frac{r^2}{w^2}\right) e^{-r^2/w^2} e^{il\phi} \tag{5.6}$$

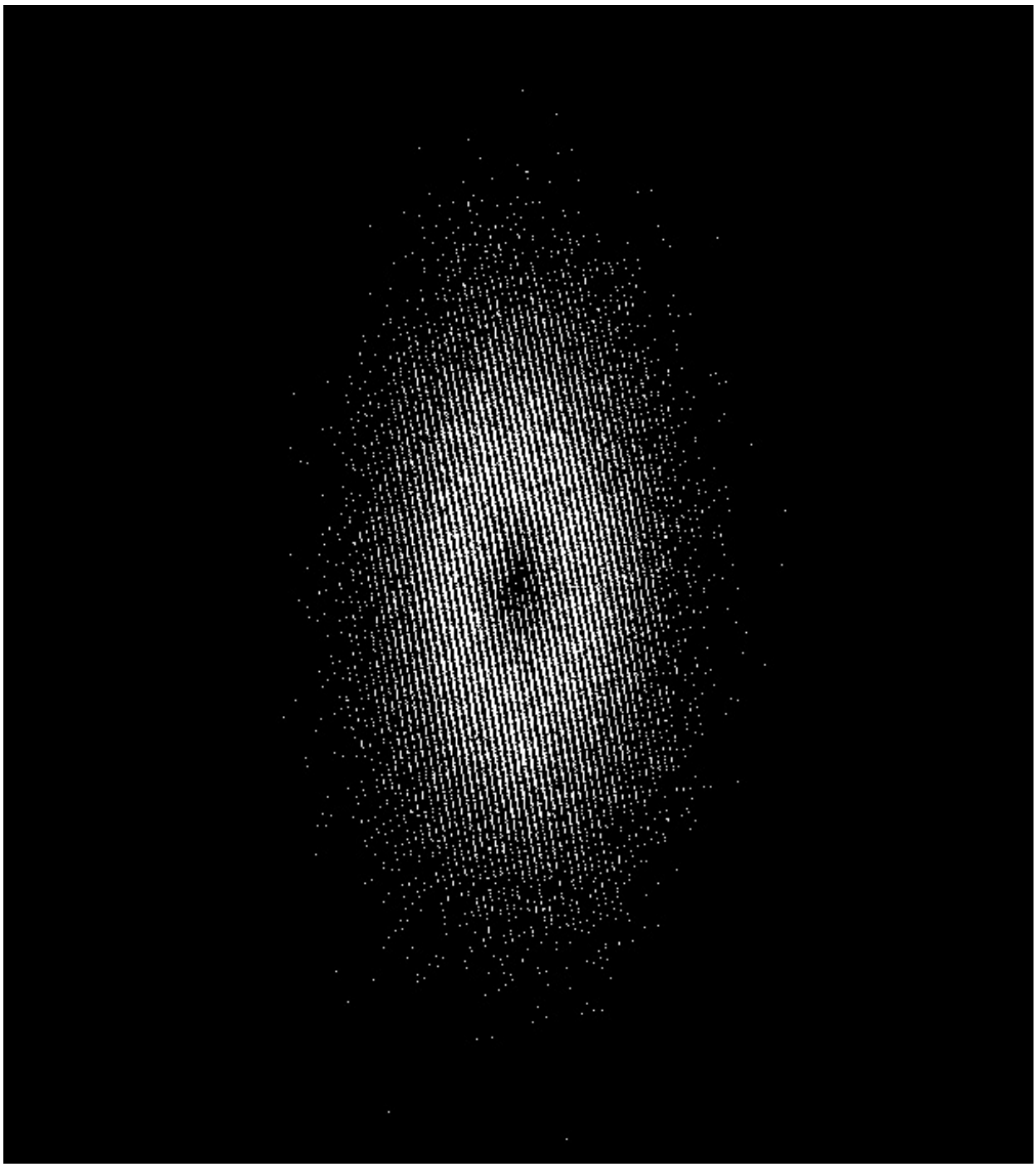

Figure 5.5: **Hologram of LG_{01}.** In the 684 x 608 bitmap image we display on the DMD, the white pixels represent "on" mirrors and the black "off". This hologram of the LG_{01} mode exhibits the characteristic central node as well as a "fork" in the gratings where the branch cut in the phase occurs.

where w is the waist size and L_p^l are the generalized Laguerre polynomials. The index l is called the winding number, and $(p+1)$ is the number of radial nodes. The term $r^{|l|}$ is responsible for the characteristic node in LG modes with $l \neq 0$. Furthermore, the azimuthal term $e^{il\phi}$ is responsible a helical wavefront: the phase variation along a closed loop around the center is $2\pi l$. For this reason, LG modes carry orbital angular momentum, in addition to spin (polarization) angular momentum, and they have received increasing interest in applications such as multi-dimensional entanglement and quantum communication [42].

Figure 5.5 shows a typical hologram of the LG_{01} mode that we display on the DMD. The hologram is encoded in the 684 x 608 bitmap image, where the white pixels denote the mirrors that are "on" and the black pixels denote those that are "off". Besides the expected node in the center of the profile, there is also a fork-like feature, or dislocation, where one grating slit bifurcates into two slits, signifying a branch cut.

Next, we displayed the hologram for LG_{55} and imaged the resulting diffraction pattern on the image plane on a CCD camera; see Fig. 5.6. Although the main features like the concentric rings were present, the central node appeared stretched, indicating an imperfect mode distorted by optical aberrations. In the following section, we discuss the phase-correcting procedure.

5.3 Compensating optical aberrations with the DMD

5.3.1 The origin and effect of optical aberrations

The essence of Chapter 2 has been the Gaussian beams, which are the solutions of the paraxial wave equation. They are the starting point from which I described the theory of light propagation through optical elements and optical cavities. However, the paraxial approximation, in which the wavevector of a beam makes a negligibly small angle θ with the

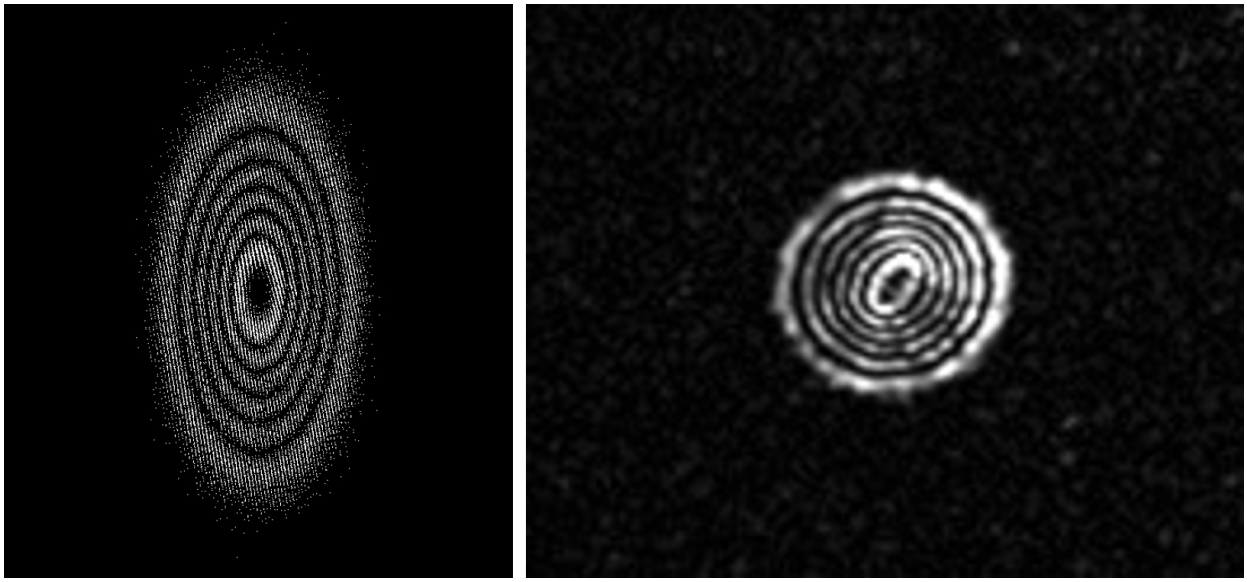

Figure 5.6: **Hologram and image of LG_{55}.** (left) The hologram displayed on the DMD. The bitmap appears stretched because of the DMD's rectangular shape. (right) The resulting diffraction pattern on the image plane captured with a CCD camera. Optical aberrations distort the field, yielding an imperfect mode.

optical axis, is an ideal condition that ignores higher-order terms in the expansion of $\sin\theta$:

$$\sin\theta = \theta - \frac{\theta^3}{3!} + \frac{\theta^5}{5!} + O(\theta^7) \tag{5.7}$$

The higher-order terms give rise to what are known as optical aberrations. Specifically, the third-order terms result in the famous Seidel aberrations, which include astigmatism, coma, and spherical aberrations. Along with defocus and tilt that come from misalignment, these aberrations bend and distort the wavefront of the transiting light, reducing its spatial coherence.

The effect of the aberrations can be better understood in the Fourier optics picture. The diffraction-limited image is formed by the superposition of all point-spread functions convolved with the object (up to the numerical aperture). Optical aberrations cause phase distortions, which in turn decrease the intensity of the interference between the frequency components arriving at the image plane. The result is a re-distribution of power in the image, or blurring, which is undesirable in most AMO applications. In particular, for cavity

mode-matching, the presence of aberrations sets a limit to the efficiency with which we can couple incident power into a particular mode.

The highlight of the holographic spatial light modulation is the use of the DMD to not only dynamically realize arbitrary beam profiles but to measure and correct all phase distortions in the path of the beam to much less than 2π.

5.3.2 Creating a phase map

We can compensate the phase distortions caused by aberrations wholesale by applying a phase map to the DMD prior to displaying the relevant hologram for the desired beam profile. To calculate this map, we again place the DMD in the Fourier plane of an optical system and a CCD camera on the image plane. As a result of Fourier decomposition, as the collimated beam reflecting off of the DMD propagates through the system, the spatial positions on the Fourier plane are converted to angles of plane waves arriving at the image plane. The angles in turn correspond to frequency components. By displaying a series of gratings on different areas of the DMD and measuring the corresponding phase in the image plane, we can measure the total phase delays caused by the aberrations.

The algorithm is as follows.

1. Divide the DMD area into a grid of smaller patches, e.g. 21 x 21. Display one grating in the center patch to serve as the reference and another grating on a specific patch.

2. Shine a collimated beam on the DMD, covering its entire surface. The reflected beams from the two gratings are combined with a lens and results in an interference pattern in the image plane. Record the interference pattern with a CCD camera and measure the sum of the intensity in a small designated area (smaller than the length of an interference fringe), thus using the camera as a pinhole.

3. To acquire the phase, we resort to phase shifting interferometry [43]. We record three images per patch, each with the patch's grating shifted by $2\pi/3$. The three measured

intensity values are used to calculate the phase:

$$p = -\frac{1}{3}\left(I_{2\pi/3} + I_{4\pi/3} - 2I_0\right) + \frac{i}{\sqrt{3}}\left(I_{2\pi/3} - I_{4\pi/3}\right) \tag{5.8}$$

$$\Delta\phi = \arg[p] \tag{5.9}$$

where p is the phasor for that particular patch and $\Delta\phi$ is the aberrations-induced phase delay.

4. Once $\Delta\phi$ has been determined for all the patches, perform phase unwrapping to pin down the absolute phase and then interpolate/extrapolate to the rest of the 684 x 608 mirrors, resulting in a complete phase map for the DMD.

Supplied with the phase map, we can subtract it from any hologram we display on the DMD from now on. If g denotes the original hologram of the desired beam profile, then the modified hologram becomes

$$g(x,y) = \cos(k_x x + k_y y + \phi(x,y)) \rightarrow \cos\left(k_x x + k_y y + \phi(x,y) - \Delta\phi(x,y)\right) \tag{5.10}$$

where ϕ is the phase of the Fourier transform.

In the following section, we apply the procedure outlined above step-by-step to create a phase map, which is used to improve the beam profile in free space as well as mode-matching into an optical cavity.

5.4 Cavity mode-matching with the DMD

5.4.1 Experimental setup

Figure 5.7 shows the overall experimental setup. The DMD sits on the left-hand side, illuminated with an expanded and collimated 780-nm laser beam. A 2-inch-diameter lens that we call the diffraction lens is placed one focal length f away from the DMD while an

Figure 5.7: **Experimental setup.** (left) Overall optical setup. (right) A test three-mirror cavity. The cavity geometry is an equilateral triangle. The plastic spacer was made with a 3D printer.

iris is also placed f away on the other side of the lens. Thus, the DMD and the iris are in the Fourier plane and the image plane, respectively. The iris is required to block unwanted diffraction orders.

Next, we image the image plane. A $4f$ imaging lens focuses the light at the iris onto a CCD camera (Point Grey Flea). With the gratings displayed on the two patches of the DMD, one in the center and the other one in a corner, the physical positions of the lenses and the camera are manually adjusted on the optical breadboard until the camera shows a completely overlapping interference pattern.

The phase-correcting procedure, as well as other DMD functions, is run with Python. At the beginning of the image acquisition, all bitmap images to be displayed on the DMD are created in parallel. Then, for each patch, the three shifted gratings are displayed in sequence. After each grating, the Python code soft-triggers a function generator (Keithley), which in turn hard-triggers the CCD camera to save an image. Once all the images have been acquired, the code proceeds with the calculation of the phase map.

The rest of the experimental setup involves imaging the diffracted pattern at the position of the iris onto the waist of a test cavity, thus directly coupling the light from the DMD hologram into a specific cavity mode. A separate laser, already coupled into the cavity, is

used to facilitate optical alignment. The cavity transmission is imaged with another CCD camera and measured with a photodiode for mode-resolved spectroscopy.

5.4.2 Calculating the phase map

Figure 5.8 shows example holograms displayed on the 3 x 3 DMD patches and the corresponding images captured on the camera with the iris open. The interference pattern appears in the first diffraction order. During an actual phase map acquisition, the iris is closed around this pattern. For each patch, three holograms with shifted phase are produced in sequence, and the corresponding intensities calculated from a small region in the interference fringe; see Fig. 5.9.

Once the phase delays (mod 2π) for all the phases have been determined, we must "unwrap" them to determine their absolute values. Unwrapping is done by taking a higher density of patch data and extrapolating from these to the rest using smooth slopes from neighboring points. Figure 5.10 shows a simulation of unwrapping where the phases vary linearly.

We may repeat the whole procedure again, but this time with the phase map applied, so that we can check its effect. Figure 5.11 shows two examples of the phase landscape before and after applying the phase map. The color is in units of 2π, or one λ. In the first example, the original phase profile appears quadratic, indicating that the aberration is mostly coming from defocus, while in the second example, the profile is mostly linear, and hence, it points to tilt as the main source of aberration. Note that after applying the phase map, the residual phase delays are reduced to less than $\lambda/5$. The procedure may now be repeated yet again, refining the phase map to further remove these residues, but most times, the first phase map is enough.

Now that we have the phase map, we can apply it to actual beam shaping. Figure 5.12 shows again LG_{55} in free space captured with the camera in the image plane. This time, both images without and with the phase map are shown.

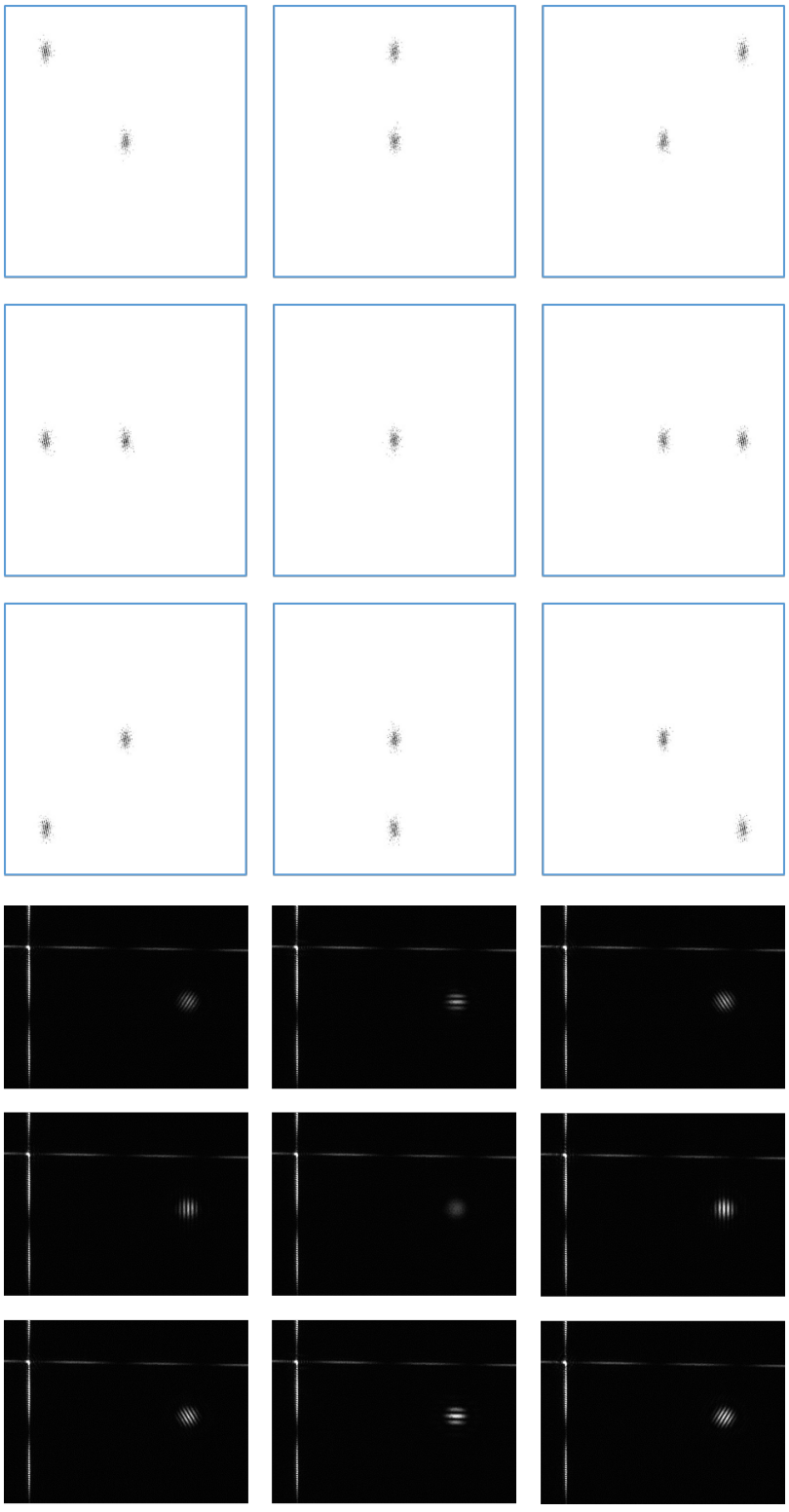

Figure 5.8: **Patch holograms and interference images.** (top) Hologram pairs displayed on the DMD patches for phase map acquisition. The center patch serves as the reference for calculating the phase. (bottom) The resulting interference pattern in the image plane.

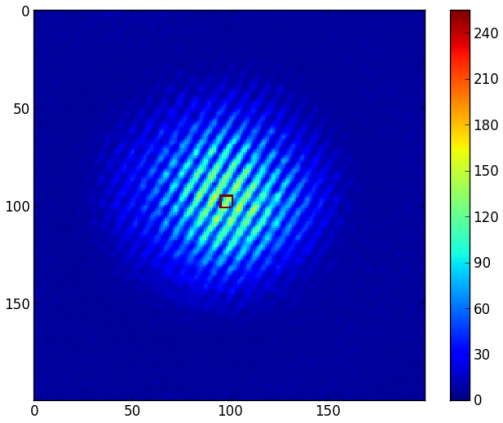

Figure 5.9: **Closed iris image.** A fixed small region (red square) of the interference pattern is used to calculate the intensity and subsequently the phase delay.

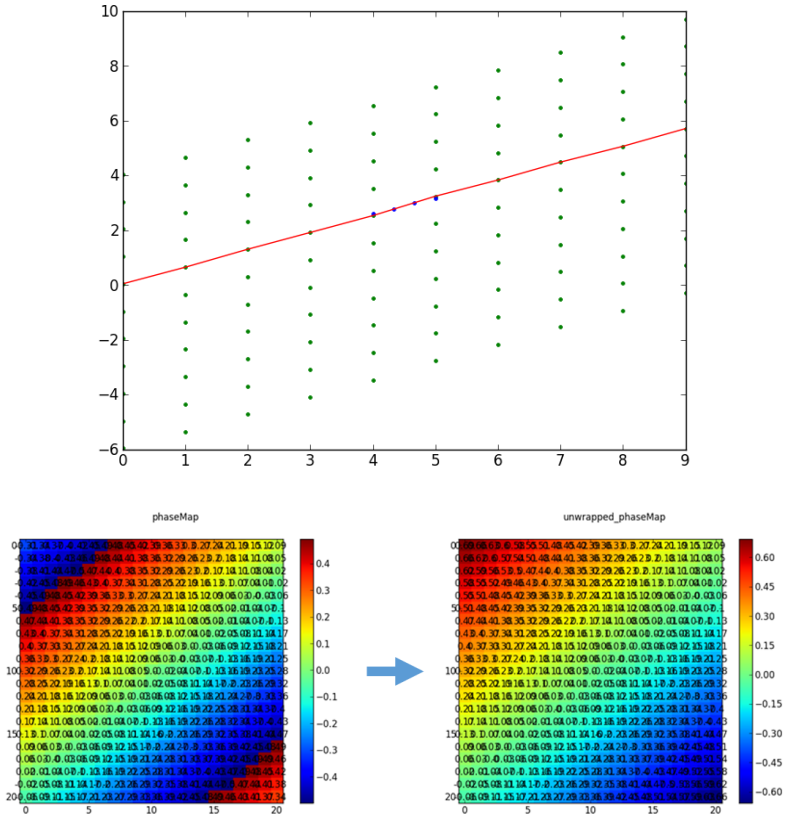

Figure 5.10: **Unwrapping the phase.** (top) Phase unwrapping is required to remove the $2\pi n$ uncertainty and determine the absolute value. The plot shows a row of patch data, with a series of vertical displacements by 2π. Starting with the blue data points, we can extrapolate by following the smooth slopes. (bottom) Before and after phase unwrapping.

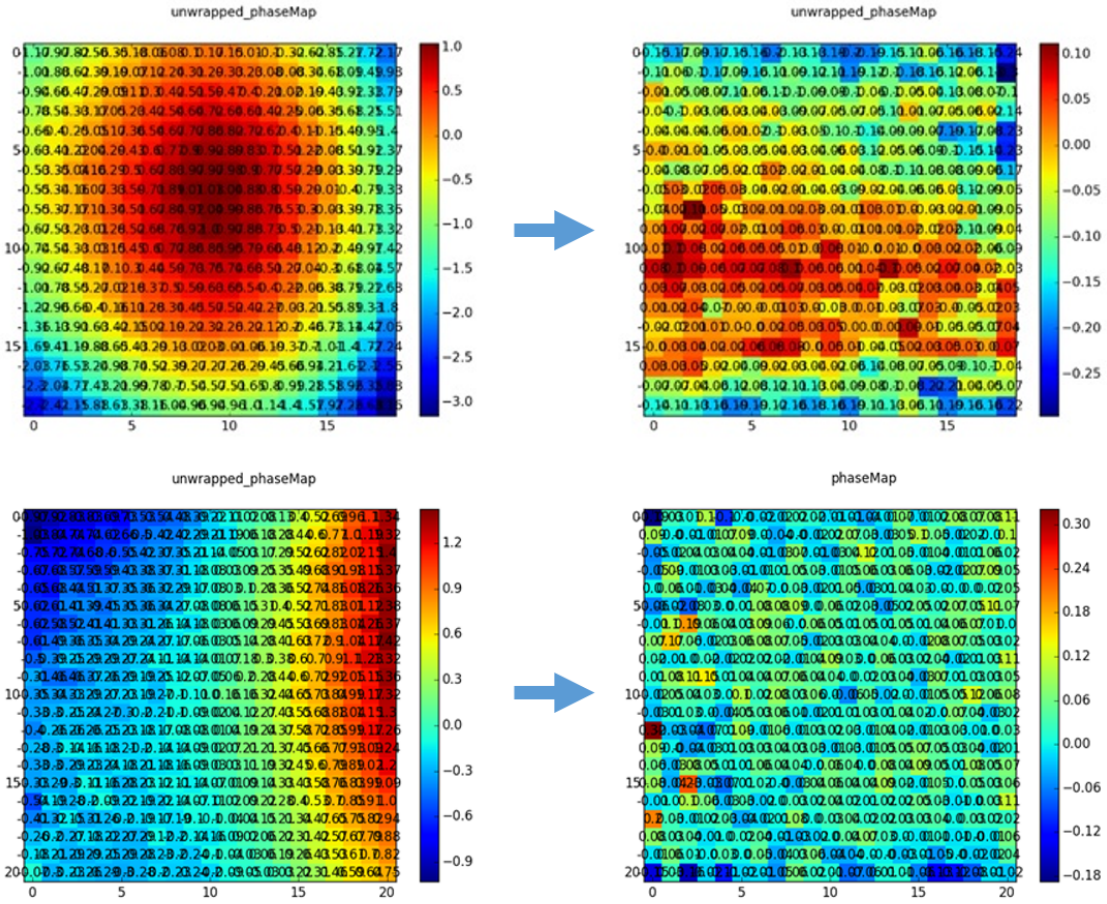

Figure 5.11: **Phase profile before and after applying the phase map.** In the first example (top), the phase is mostly quadratic, indicating the camera is out of focus. In the second (bottom), it is mostly linear, indicating the camera has been tilted relative to the optical axis. After applying the phase map, the phase profile across the DMD becomes much flatter; remaining residues can be fixed with further phase corrections.

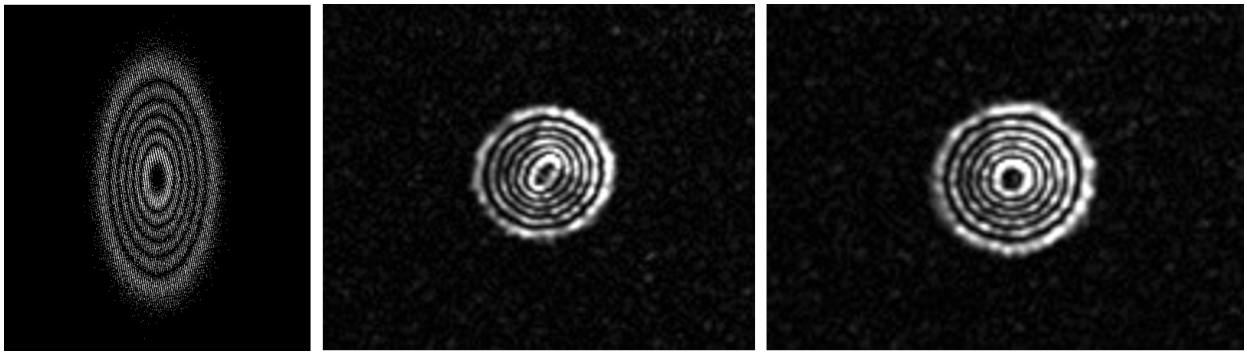

Figure 5.12: **Effect of the phase map on free-space beam shaping**. (left) Hologram of LG_{55}. (middle) Image without the phase map. (right) Image with the phase map.

5.4.3 Coupling into higher-order transverse modes

The original purpose of a holographic SLM has been to probe different modes of an optical cavity. It turns out that an optical cavity is also the most convenient way to quantitatively test the purity of the modes produced by the DMD. A cavity is a filter, decomposing the incident light into a spectrum of its modes. Thus, the success of the DMD beam shaping can be gauged by measuring the amount of power coupled into the intended specific cavity mode. Conversely, the amount of power coupled into unwanted cavity modes is a measure of the DMD's limit.

The setup is shown in Fig. 5.7. We display the Fourier transform of the cavity mode modified by the phase map on the DMD and couple the coherently reflected light into the cavity. Because the phase map we calculated is not an absolute in-situ measurement, i.e. the optical path that the phase map is calculated is only partially overlapping with that from the DMD to the cavity waist, further optimization is required for best cavity mode-matching. We manually adjust the hologram's waist sizes, as well as defocus and tilt, until the power in the desired mode is maximized. Figure 5.13 shows mode-matching into TEM_{10}, with up to 99.2% extinction for all other modes (the height of the next tallest peak is 0.8% of that for TEM_{10}).

Once we mode-match into one mode successfully, coupling into any other transverse mode is an easy task; we simply type in single commands in the computer terminal. See Fig. 5.14 for increasingly higher-order Hermite-Gauss modes.

It is not hard to imagine employing a DMD, in conjunction with a feedback loop, to automate mode-matching for every optical cavity. The caveat is that most of the incident laser power is lost in unwanted diffraction orders. For the cavity Rydberg polariton, for example, the polariton composition depends on the intensities of the probe and control lasers, and so we cannot afford to waste any laser power. On the other hand, for applications that are insensitive to the power, such as the one we will discuss next, the DMD proves to be a robust, invaluable tool.

Figure 5.13: **Coupling into $\mathbf{TEM_{10}}$.** (left) A photograph of mode-resolved spectroscopy of the cavity transmission. The CCD camera image is shown on a CRT monitor. (right) After fine-tuning the cavity waists, defocus, and tilt, up to 99.2% of the transmitted light is from the TEM_{10} mode.

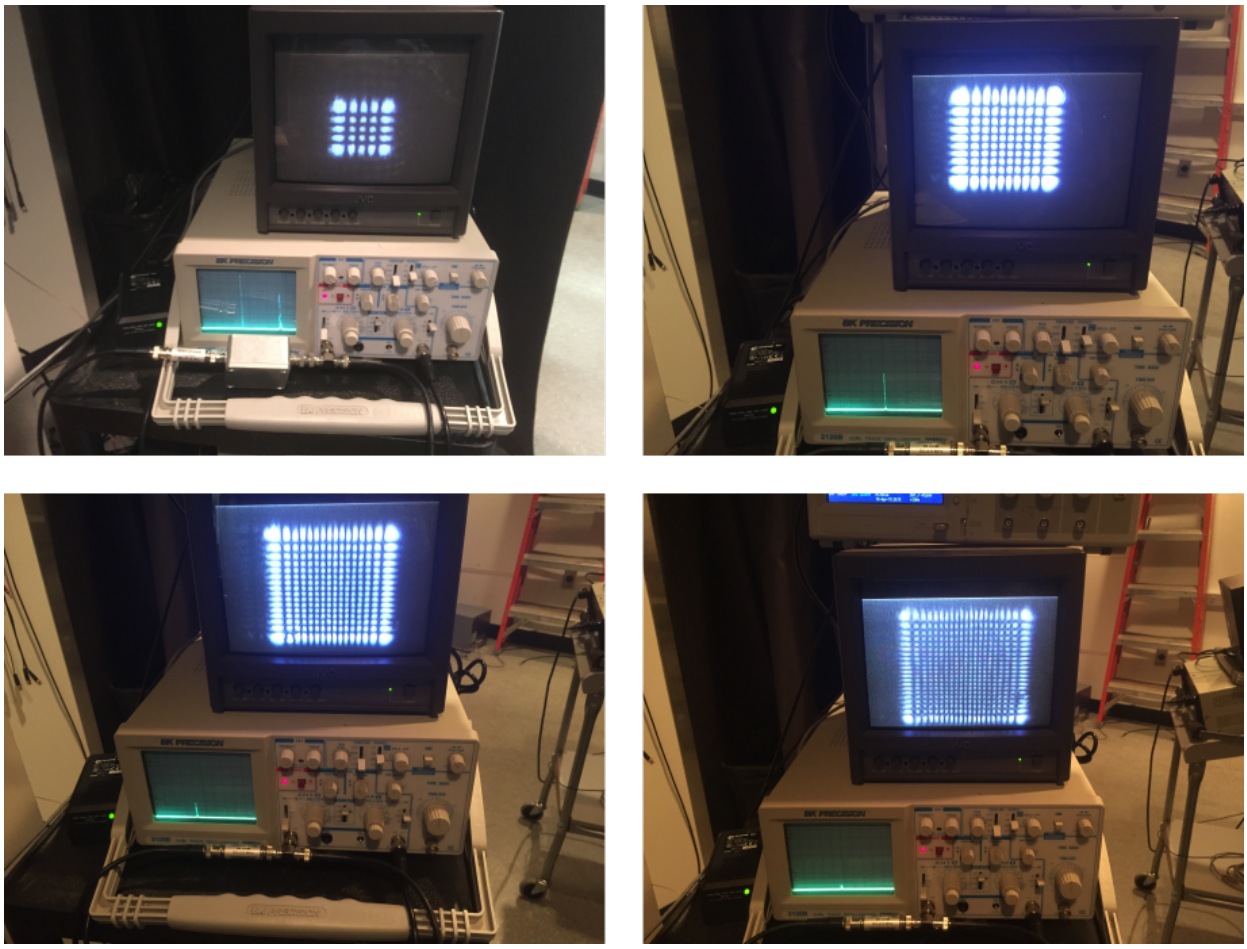

Figure 5.14: **Coupling into higher-order HG modes.** Photographs of the cavity transmission: going clockwise from top left, TEM_{44}, TEM_{99}, $TEM_{15,15}$, and $TEM_{20,20}$.

5.5 Application: synthetic Landau levels for photons

In this section, I give a brief overview of our application of the DMD in the demonstration of a synthetic magnetic field for continuum photons. The role of the DMD is to facilitate mode-matching into the Laguerre-Gauss modes of a twisted cavity, employing the aforementioned phase-correcting scheme. Greater details to this work can be found in Ref. [40].

5.5.1 A quick background

The physics of the quantum Hall effect hinges on the Lorentz force on a charged particle moving through a magnetic field. A synthetic magnetic field can result for photons traveling in a twisted, nonplanar cavity. Upon a round trip, both the photons' field and polarization get rotated by the twist angle. The polarization rotation merely lifts the degeneracy between the circularly polarized modes. The image rotation, on the other hand, introduces two effects: Coriolis and centrifugal forces.

To map the photons in the twisted cavity to the 2D electrons in a magnetic field, the centrifugal force must be cancelled. In the rotating frame, the Fock-Darwin Hamiltonian of the system is given as

$$H = \frac{1}{2m}\left(\mathbf{p} - \frac{(qB)^{\text{syn}}}{2}\right)^2 + \frac{1}{2}m\omega_{\text{trap}}^2\mathbf{r}^2 \tag{5.11}$$

where ω_{trap} is the harmonic trapping frequency. When the cavity is tuned such that the harmonic trap supplied by the curvature of the mirrors exactly cancels the centrifugal force, only the Coriolis force, equivalent to the Lorentz force, remains. Then, the cavity modes become degenerate, and the Hamiltonian describes massive particles in Landau levels with energy $\hbar\omega_c\left(n + \frac{1}{2}\right)$.

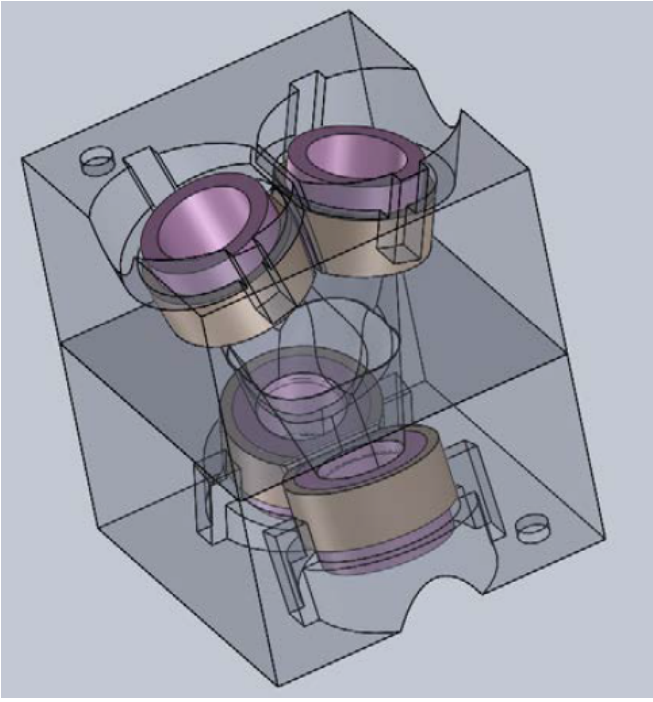

Figure 5.15: **Twisted cavity schematic.** The cavity consists of four mirrors that lie in a stretched tetrahedral configuration. The intracavity field rotates about the optical axis on every round trip.

5.5.2 Experimental results

A twisted, nonplanar optical cavity is one in which the cavity mirrors are not all on the same plane; see Fig. 5.15 for a schematic of the cavity spacer. The cavity eigenmodes are Laguerre-Gauss modes, hence the absolute need for the DMD for injecting light. During the experiment, the length of the cavity is tuned until the modes become degenerate in frequency; see Fig. 5.16 for a cartoon of the modes' energy levels.

As the cavity is tuned across the degeneracy point, its mode-resolved spectrum after injecting individual Lagurre-Gauss modes is measured. Figure 5.17 shows the spectra patched together vs the amount of the cavity length tuned, relative to the degeneracy point. We can see that the mode spacing becomes denser, hits degeneracy, and then less dense again.

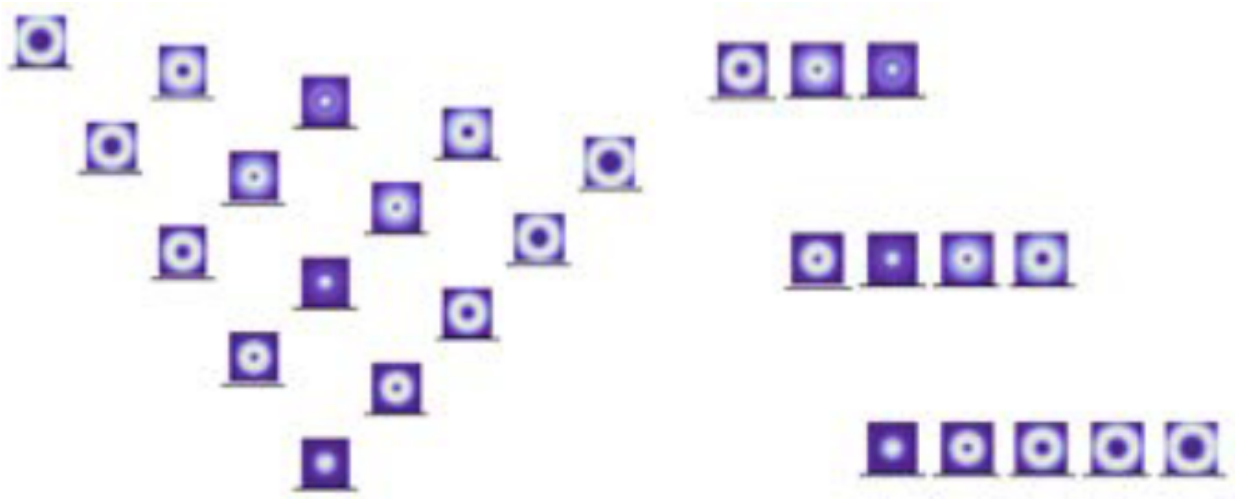

Figure 5.16: **Energy level diagram of the twisted modes.** Upon twisting the cavity (left to right), the modes become degenerate, forming a ladder of Landau levels.

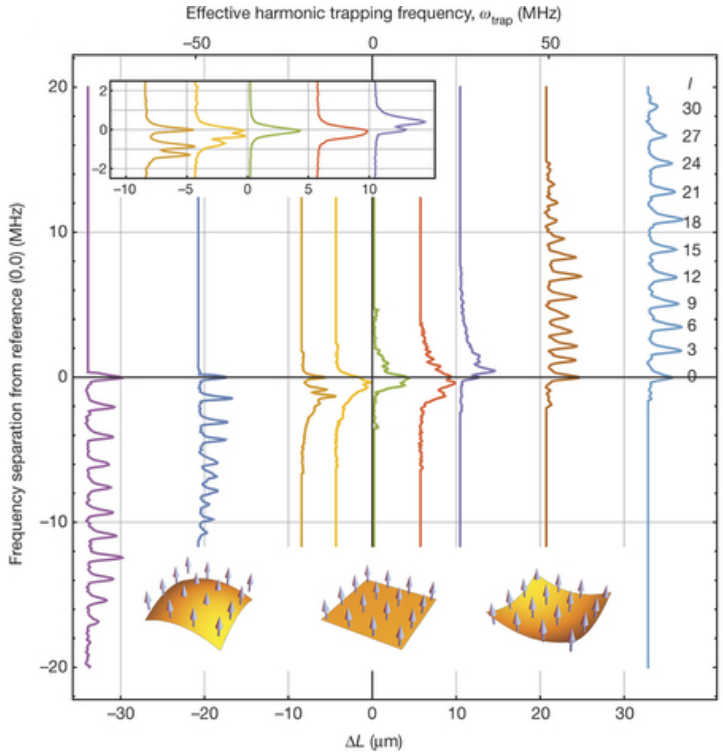

Figure 5.17: **Measured mode spectra** (main) The frequency data of individual LG modes vs cavity length tuned have been patched together to show the complete spectra. As the cavity length (twist) is tuned, the modes go through a degeneracy point, up to the weak level repulsion due to mirror imperfections. (inset) The low-order LG modes become degenerate within the cavity linewidth ($\kappa = 2\pi \times 200$ kHz).

5.6 Conclusion

The next step for the twisted cavity experiment will be to add interactions to the system, via Rydberg EIT, to break the time-reversal symmetry and advance toward realizing the Laughlin wavefunction, thought to be the ground state of a system exhibiting fractional quantum Hall physics. It is the versatility of the DMD, combining adaptive optics with beam shaping, that opens the door to numerous hitherto unexplored frontiers in AMO experiments.

CHAPTER 6

STABILIZING THE CAVITY WITH AN FPGA-BASED FIR FILTER

6.1 Introduction

Active stabilization is a crucial tool for applications spanning physics and engineering. Lasers, resonators, interferometers, and even noise-canceling headphones employ closed-loop feedback for noise suppression and real-time control. In the case of noise suppression, the range of frequencies that the feedback can counteract is set by the "reaction time": the delay between when a system first detects noise and when it responds to the appropriate control input [44]. The upper limit of this range is called the unity gain frequency, or bandwidth.

In controlling mechanical systems, one rarely achieves the time-delay limited bandwidth due to the presence of acoustical resonances. These low-frequency vibrational modes, ranging between a few Hz and several hundred kHz, are accompanied by large phase shifts that can turn the negative feedback positive, resulting in spontaneous oscillation of the system. The most widely used control mechanism, the proportional-integral-derivative (PID) controller, can cancel a single resonance, but in practice the complexity involved with fine-tuning, along with the necessity of rolling off the derivative gain at high frequency, leads many experimenters to omit derivative feedback and accept lower bandwidth [44].

This bandwidth limitation due to the resonances have led a number of groups to modify the mechanical structure itself to either damp the resonances or push them to higher frequencies. In stabilizing a femtosecond laser cavity with piezoelectric transducer (piezo) fiber-stretchers, Sinclair et al. damp numerous "violin-like" resonances between 1 kHz and 100 kHz with modeling clay and electrical tape [45]. Chadi et al. employ a side-clamping holder for their piezo [46], utilizing structural symmetry for enhanced common-mode rejection of longitudinal coupling, an idea that has benefited laser stabilization [47]. Briles et al. fill their copper actuator mount with lead [48]. These methods, while highly effective,

impose severe design constraints.

A more flexible approach is to modify the control law with inversion-based optimal control: the control input is filtered with the inverse of the system's dynamic response to avoid exciting the mechanical resonances [44]. This technique has been successfully employed to accelerate the step-response outside of the loop [49, 50, 51, 52], but has yet to be applied to in-loop noise suppression. *feedforward* is not constrained by latency and may be precomputed offline. By contrast, *feedback* requires real-time, low-latency loop shaping.

With recent advances in field-programmable gate arrays (FPGAs), low-latency digital feedback has become a viable alternative to its analog counterpart, offering enhanced tunability and loop control. Yang et al., Schwettmann et al., and Sparkes et al. implement FPGA-based PID controllers [53, 54, 55], and Leibrandt et al. configure a notch filter to cancel the lowest-frequency mechanical resonance of a doubling cavity [56]. Compensating for more complex mechanical systems requires sophisticated loop shaping that may be digitally implemented with finite impulse response (FIR) or infinite impulse response (IIR) filters. While such FPGA-based filters have been demonstrated by a number of groups [57, 58, 59, 60], they have not been applied to noise suppression in acoustical systems.

In this chapter, I describe my work on a novel digital architecture for loop-shaping in acoustical feedback systems [61]. Harnessing the massive processing power of a state-of-the-art FPGA, we demonstrate a low-latency, 25,600-tap FIR filter capable of *precisely* canceling an arbitrary number of acoustical resonances (poles) and anti-resonances (zeros) below $\sim$100 kHz, thereby enhancing the noise-suppression bandwidth by more than an order of magnitude.

In Section 6.2, I summarize single-input-single-output feedback control, the restrictions on the system transfer function imposed by causality and time delay, and the FPGA FIR filter. In Section 6.4, I provide a step-by-step illustration of our technique: we measure the piezo-controlled, electro-optical transfer function of the high-finesse optical resonator from Chapter 4, generate an inverse filter, and demonstrate more than an order of magnitude

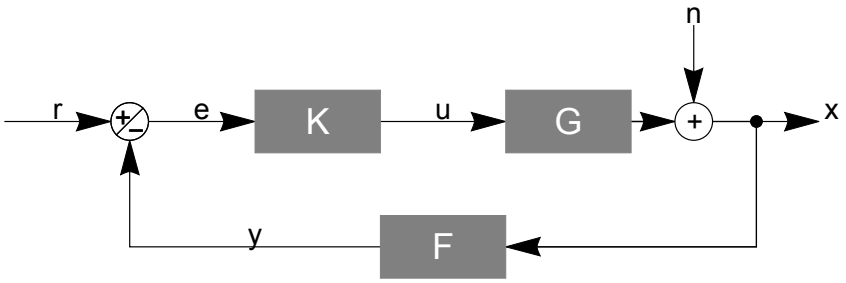

Figure 6.1: **Block diagram of a general feedback loop**. The output from the detector in the physical system G is fed into the FPGA-based FIR filter F, which conditions it to remove the acoustical resonances and anti-resonances. The analog feedback controller K (typically proportional plus integral gain) takes the difference between the filtered signal and the reference r and feeds it back into the system to stabilize it.

increase in feedback bandwidth. Finally, in Section 6.5 I conclude by exploring potential applications in areas beyond atomic and optical physics.

6.2 Brief introduction to feedback and control theory

Feedback, specifically negative feedback, is a form of self-regulation that takes the output of a system as part of its input, driving it with appropriate modifications, called the *control*, in order to keep the output at the desired level. It is a unifying concept in science, and it appears in a wide variety fields, including technology, biology, economics, etc. [62].

6.2.1 Feedback bandwidth and stability

Figure 6.1 shows the block diagram of a generic feedback loop. In such a diagram, arrows represent signals and blocks represent physical components that operate on the signals. The block term G denotes the physical system to be controlled, K denotes the controller, and F denotes the FPGA, a special digital filter that is the focus of this work. The signals r, e, u, n, x, and y denote the reference (set-point), the error, the system input, the noise, the system output, and the FPGA-modified output, respectively.

In the frequency domain, the effect of the noise on the output can be calculated as follows:

$$x = KGe + n \tag{6.1}$$

$$e = r - y \tag{6.2}$$

$$y = Fx \tag{6.3}$$

$$x = \frac{KG}{1 + KGF} r + \frac{1}{1 + KGF} n \tag{6.4}$$

The feedback suppresses noise by a factor $1/(1 + KGF)$ called the sensitivity [44]. The typical behavior of the sensitivity is decreasing suppression of the noise up to the unity gain frequency, where the magnitude of the loop gain $|KGF| = 1$. We define the feedback bandwidth to be equal to the unity gain frequency.

As can be seen from Equation (6.4), when $KGF \approx -1$, the system becomes unstable and undergoes spontaneous oscillations. This instability condition - unity loop gain with π phase - is met by acoustical resonances, which cause the phase and amplitude of KGF to vary violently within a small frequency range. We will thus need to quantitatively characterize the general frequency response of a physical system and suppress the resulting resonances to prevent the system from oscillating as it approaches unity gain.

6.2.2 Character of the physical system G

The transfer function of any linear system without a time delay (i.e. minimum phase [44]) can be written as a rational function of the frequency ω:

$$G(\omega) = \frac{M(\omega)}{N(\omega)} \tag{6.5}$$

where $M(\omega)$ and $N(\omega)$ are polynomials whose roots are called zeros and poles, respectively, of the system response. For a general physical system, the polynomials may be arbitrary as long as the corresponding impulse response function (time-domain Green's function, which

is the inverse Fourier transform of the frequency response) is both real and causal.

Realness of the time-domain impulse response implies that $G^*(\omega) = G(-\omega)$ for real ω [63]; thus, all poles and zeros of the Fourier-domain transfer function either occur on the imaginary axis or come in pairs reflected across the imaginary axis. To satisfy causality, the poles and zeros of a stable system must be located in the upper half of the complex ω-plane such that a contour integration yields a Green's function that is zero for $t < 0$ and nonzero for $t \geq 0$ [63].

Building upon these ideas, we factorize the transfer function of the physical system G with delay τ_G as:

$$G(\omega) = Ae^{i\omega\tau_G} \left[\frac{\prod_j \left(\omega - i\gamma_z^j\right)}{\prod_j \left(\omega - i\gamma_p^j\right)} \right] \left[\frac{\prod_k \left(\omega - \omega_z^k\right)\left(\omega + \omega_z^{k*}\right)}{\prod_k \left(\omega - \omega_p^k\right)\left(\omega + \omega_p^{k*}\right)} \right] \tag{6.6}$$

where A is a real amplitude, τ_G is a time delay, the products over j are over first-order zeros and poles, $\gamma_{z,p}$, and the products over k are over second-order zeros and poles, $\omega_{z,p}$. The latter are complex frequencies whose imaginary part is the linewidth of the corresponding pole or zero.

Given the system G and the controller K, the role of the FPGA is to implement a filter response F such that the loop gain KGF exhibits a smooth $1/\omega$ behavior whenever $|KGF|$ is within an octave of unity; this ensures that the phase of KGF is approximately $\pi/2$, and thus that the sensitivity $1/(1 + KGF)$ does not diverge.

6.2.3 Physical origin of resonances

Before I describe how we constructed our filter, let's take a short detour to explore how the resonances arise in a mechanical system and anticipate the kind of transfer function the filter must face.

The resonances (poles) and the anti-resonances (zeros) observed in the system transfer function arise from constructive and destructive interference between the normal mode of

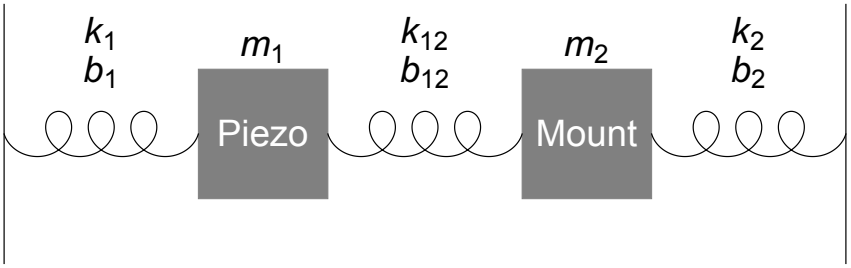

Figure 6.2: **Simple model: coupled damped harmonic oscillators.** Diagram of a model consisting of two coupled damped harmonic oscillators. Each oscillator m_i is held to a rigid wall by a spring with spring constant k_i and damping term b_i. The hybridization of the individual normal modes gives rise to a pole-zero pair and a separate pole in the transfer function of the piezo, and the order in which the paired pole and zero appear depends on the relative strength between k_{12} and b_{12}. In the real experiment, the piezo is epoxied to the back of a resonator mirror, and thus the noise response of the system can be directly mapped to the positional stability of the mirror/piezo.

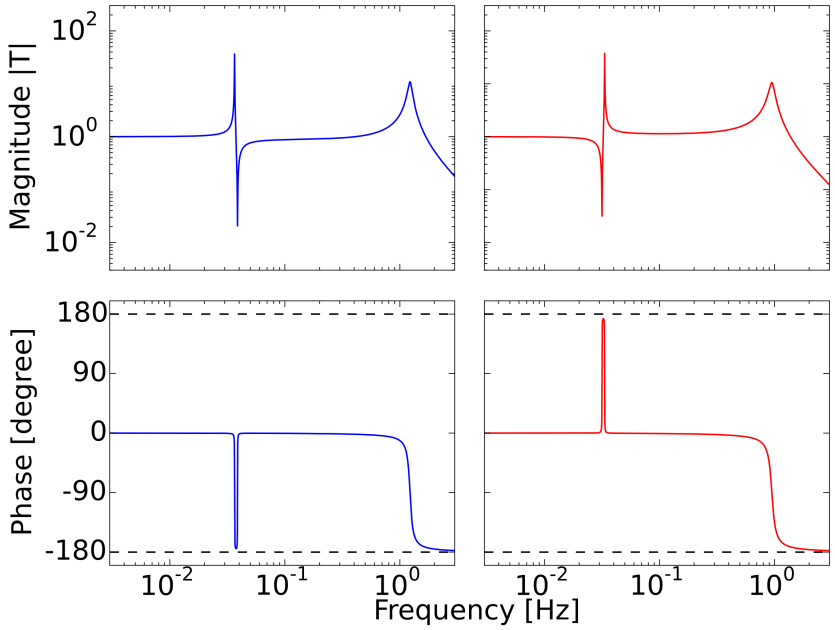

Figure 6.3:]

Model Transfer Function T**.** (*top*) Magnitude and *(bottom)* phase of the transfer function versus frequency. The interference between the piezo and the mount results in a pole-zero pair as well as a separate pole. (*left*) For real coupling ($k_{12} \gg b_{12}$), the pole appears before the zero. (*right*) For imaginary coupling ($k_{12} \ll b_{12}$), the zero appears before the pole. The poles and the zeros are accompanied by phase shifts of $-\pi$ and π, respectively.

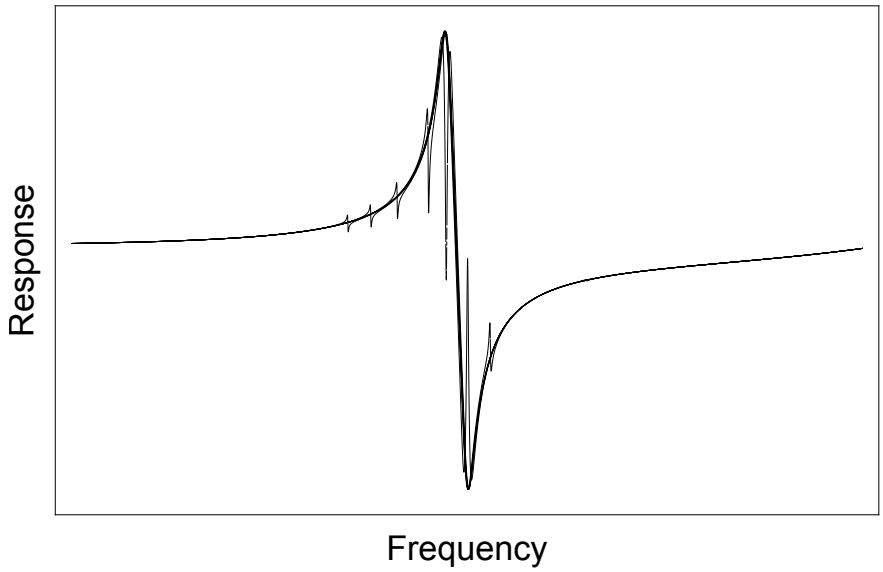

Figure 6.4: **Filtering of mount resonances by intervening components**. The plot shows the mechanical response of the piezo/mirror near the frequency of a primary mount resonance (black trace) to which it is directly coupled, and how that response is perturbed by a secondary mount resonance coupled to the piezo/mirror only indirectly, through the primary resonance (gray traces), as the frequency of this secondary resonance is scanned across the primary resonance. It is apparent this secondary mount resonance only impacts the response of the piezo/mirror when it falls atop the primary mount resonance, and is thus allowed to pass through.

the piezo and each normal mode of the mount structure. To see why, we study a simple model consisting of two coupled damped harmonic oscillators, with masses m_1 ("piezo") and m_2 ("mount"), connected to rigid walls by damped springs k_1 (b_1) and k_2 (b_2) and to each other with a damped spring k_{12} (b_{12}). See Figure 6.2 for the diagram of the model.

The transfer function T of the piezo is given by taking the first-row-first-column element of the 2×2 matrix

$$T(\omega) = \left[\left(K + iB\omega - M\omega^2 \right)^{-1} \right]_{00} \tag{6.7}$$

where $M = \begin{pmatrix} m_1 & 0 \\ 0 & m_2 \end{pmatrix}$, $B = \begin{pmatrix} b_1 & b_{12} \\ b_{12} & b_2 \end{pmatrix}$, $K = \begin{pmatrix} k_1 & k_{12} \\ k_{12} & k_2 \end{pmatrix}$, and the exponent denotes matrix inversion.

Figure 6.3 shows the magnitude and the phase of T for two cases: (*left*) $k_{12} \gg b_{12}$; (*right*) $k_{12} \ll b_{12}$. In both cases, the transfer function exhibits a pole-zero pair (due to the piezo-mount coupling) as well as an isolated pole (due to the piezo alone). The order in which the pole and the zero appear in the pair depends on the relative strength of the spring (k_{12}) versus the damping (b_{12}) coupling. In the former case, the coupling is mostly through displacement, and the pole appears before the zero. In the latter case, the coupling is mostly through damping (providing an additional π phase), and the zero appears before the pole. As expected, the poles and the zero are accompanied by phase shifts of $-\pi$ and π, respectively.

For the optical resonator, we observe that the resonances are almost *always* split, often multiply. The most obvious reason for this splitting is a broken symmetry of the system, resulting in two nearly degenerate resonances each coupled to the mirror location through the piezo. More broadly, however, it is clear that the most of the mounting structure is coupled to the piezo/mirror only through another piece of the mount to which it is *physically connected*. The resonances of these mechanical components are *shielded* from influencing the resonator length except when they happen to fall on top of, or near, the resonances of the intervening mount structure. This is illustrated in Figure 6.4, suggesting the resonance splitting is an anthropic effect – there are potentially mount resonances at all frequencies, but we only

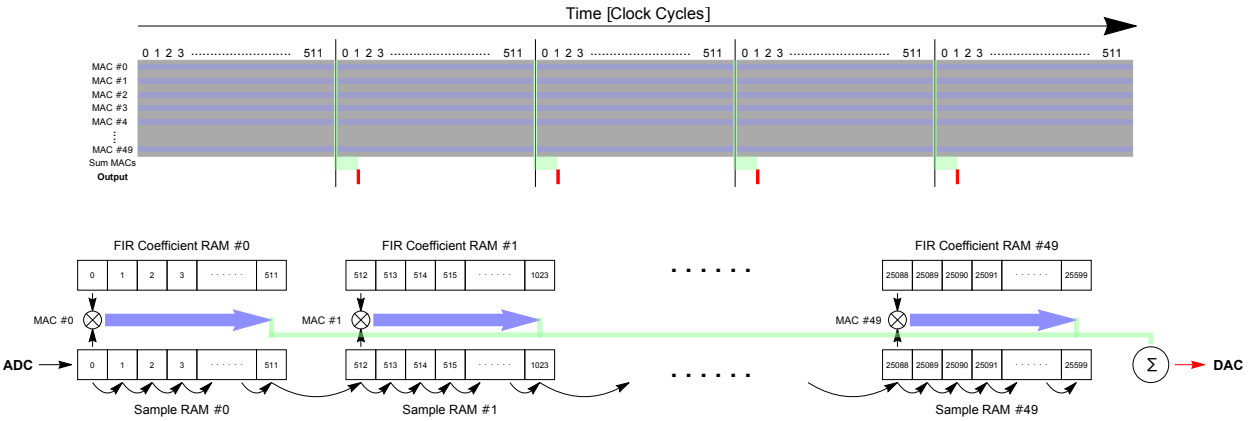

Figure 6.5: **FPGA FIR filter implementation**. The FIR filter is a real-time digital implementation of a temporal impulse response function. The last 25,600 values of a sampled input signal from an analog to digital converter (ADC) are multiplied by 25,600 user-defined filter coefficients, and the results are summed and sent to a digital to analog converter (DAC). This calculation is performed by 50 Multiply-ACcumulators (MACs) in parallel, each carrying out 512 multiplications and additions in series, which are then summed in series. (top) Timing diagram for the series-parallel FIR filter implementation in the FPGA. The ~ 512 clock cycles of each sample period are broken down, reflecting when the 50 parallel MACs are operating, and when their results are summed in series and output. (bottom) Connectivity diagram of the implementation, reflecting the 50 sample and coefficient RAMs, each connected to a MAC, and the path an input sample takes through the sample RAMs over time.

observe those occurring on top of the resonances that directly couple to the piezo.

While it is in principle possible to fit the measured system transfer function G with a physical model consisting of an arbitrary number of coupled damped harmonic oscillators, the mathematical model described by Equation 6.6 offers significant advantages: First, the mathematical model eliminates extraneous degrees of freedom (which masses are coupled together and how strongly, how much and by whom they are damped, and which we drive and detect), and we only fit to poles and zeros we are interested in, namely those that limit the feedback bandwidth. Second, the fitting is much faster as the functional form does not require a matrix inversion.

6.3 FPGA FIR filter

6.3.1 FPGA FIR filter

An FIR filter is a digital implementation of a discrete, time-domain Green's function [64]. A number of samples are convolved with an equal number of filter coefficients to produce a filter with compact support in time (hence *Finite* Impulse Response, FIR). The FIR filter and its z-transform (generalized discrete-time Fourier transform) [64] are given by:

$$y_n = \sum_{m=0}^{J_{max}-1} a_m x_{n-m} \tag{6.8}$$

$$\tilde{y}(z) = \left[\sum_{m=0}^{J_{max}-1} a_m z^m \right] \tilde{x}(z) \tag{6.9}$$

where $z = e^{i\omega\tau_s}$ and τ_s is the sampling period, x_n is the input sample at time $t = n \times \tau_s$ and y_n is the resulting output sample. τ_s determines the maximum frequency of the filter $(1/(2\tau_s))$, and the number of samples included in the filter J_{max} determines the spectral resolution $(1/(\tau_s J_{max}))$, and hence quality factor, of the poles and zeros of the filter. This filter is the time-domain implementation of an arbitrary Green's function $F(t) \approx \sum_{m=0}^{J_{max}-1} a_m Sq(t - m\tau_s)$, where $Sq(t)$ equals one if $t \in [0, \tau_s]$ and zero otherwise. $\tilde{y}(z)$ may be understood as the frequency (z) domain response of the system to a frequency-dependent drive $\tilde{x}(z)$; here the ω-dependence is implicit in the definition of z. Note that sampling already *imposes* a system time delay of $\tau_s/2$, half the sample period, implicit in equation 6.9.

It is important to understand why high-Q FIR filters require numerous taps (coefficients): a resonance of a linewidth $\Gamma = 1/\tau$ takes a time of several (say, n) τ to decay. Consequently, implementing such a resonance in an FIR filter (and thus in the time domain) requires coefficients that span that time interval $n \times \tau$. By the same token, to implement a resonance at a frequency f, the sampling frequency of the FIR filter must be at least $2 \times f$ to avoid aliasing. The upshot is that if the desired maximum realizable resonant feature in the filter is f_{max},

and the minimum linewidth that the filter can implement is γ_{min}, then for an FIR sampling frequency $f_s \approx 2f_{max}$, the number of coefficients must satisfy $N_{taps} \geq 2n \times f_{max}/\gamma_{min}$. This is true regardless of whether the highest frequency resonance is also the one exhibiting this smallest linewidth.

To implement multiple resonances in the same FIR filter, the coefficients for each isolated resonance are simply added together. The FIR filter may then emulate an arbitrary number of poles and zeros within the aforementioned constraints on feature frequencies and their linewidths. By contrast, an equivalent infinite impulse response (IIR) filter requires only as many taps as the number of poles and zeros in the desired filter function, but each operation must be performed to much higher accuracy to avoid numerical instability [64]. It is only the massively-parallel nature of the FPGA that makes low-latency FIR architectures possible.

We employ a filter with $J_{max} = 25{,}600$ coefficients (17-bit). The essential building block is the Multiply-ACcumulator (MAC), a physical (non-reconfigurable) component of an FPGA which can, within a single clock cycle, perform a signed, fixed-point multiplication, along with both pre- and post- additions. The filter is implemented using $N_{MAC} = 50$ MACS, operating in parallel, each realized in a single DSP48 slice in the FPGA, and each capable of carrying out $n_{op} = 512$ serial multiplications and additions within one sample period. This implementation yields a sampling rate $f_s = 243$ kHz $\approx \frac{f_{clock}}{n_{op}}$ and a delay of $\tau = 2.6$ μs $\approx \frac{1}{2f_s} + \frac{N_{MAC}}{f_{clock}}$, where the FPGA's clock rate is $f_{clock} = 125$ MHz. See Figure 6.5 for a diagram of the FIR implementation.

The FPGA is a commercial Red Pitaya board (redpitaya.com, ∼$240 at the date of publication) that contains a Xilinx Zynq 7010 SoC consisting of a Dual core ARM Cortex A9+ processor running network-enabled Linux as well as a 28k logic cell Artix-7 FPGA with 80 DSP48 slices and 2.1Mb BRAM, and 2 channel, 14-bit DAC/ADCs capable of sampling at 125MSPS. It is configured with custom Verilog-based firmware implementing the FIR filter. See Figure 6.6 for a photograph of the Red Pitaya board.

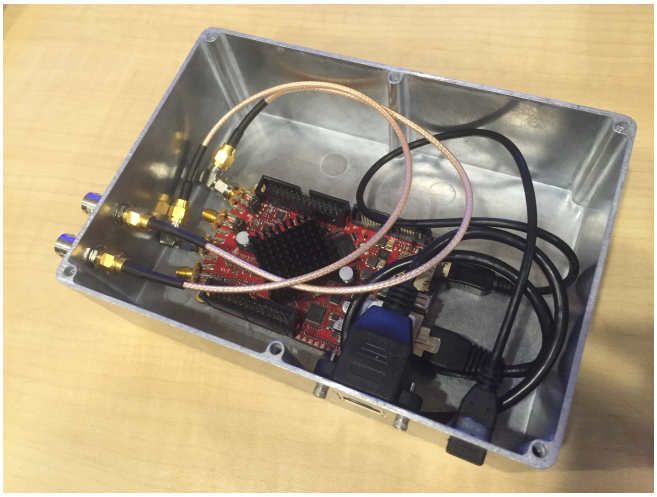

Figure 6.6: **FPGA**. The FPGA is a Red Pitaya board, shown here in a custom housing. On the left side are the input/output ports, for the raw and the modified output signals, x and y, respectively. On the right are the ports for an Ethernet cable and a power adapter.

6.3.2 Anti-aliasing filter

The discrete sampling of a continuous-time system output $x(t)$ at $f_s = 243$ kHz by the FPGA leads to aliasing: noise above the Nyquist frequency ($f_{Nyquist} = f_s/2$) is aliased into the base band. We therefore place an anti-aliasing low-pass filter before the ADC input of the FPGA. The corner frequency, $\omega_{corner} = 2\pi \times 100$ kHz, has been chosen to trade-off between suppressing aliased noise and the phase lag induced by the filter itself.

6.4 Application:

Canceling the acoustical resonances of an optical resonator

6.4.1 Description of the optical resonator

We apply the FIR filter to canceling the acoustical resonances present in a high-finesse optical cavity originally designed for the cavity Rydberg polariton experiment (see Chapter 4). To recap: In order to have a small waist size of about 10 μm, comparable to Rydberg blockade radius, the resonator consists of four mirrors in a bow-tie configuration, one of which is mounted on a single-layer piezo tube actuator. The piezo is affixed to a 2-mm

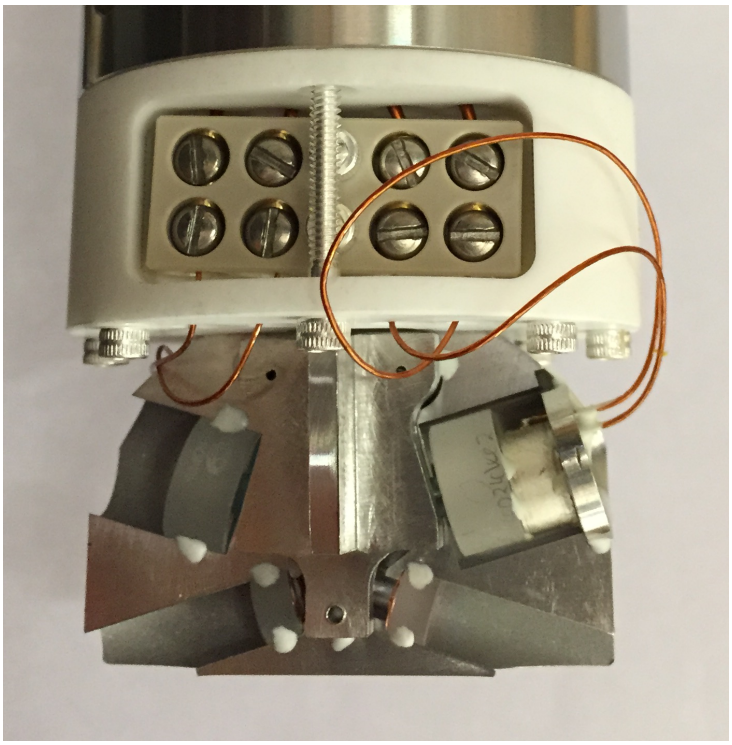

Figure 6.7: **Experimental optical cavity**. The cavity, shown here outside the vacuum chamber, consists of four mirrors in a bow-tie, running-wave configuration, one of which is mounted on a single-layer piezoelectric tube actuator. Because the cavity has been designed for a small waist, degenerate optical modes, and a large mirror separation, instead of mechanical rigidity or vibration isolation, it exhibits numerous low-frequency acoustical resonances that couple to the piezo, making this an ideal candidate for control using the digital FIR filter.

thick stainless-steel wafer, which is itself glued to a larger spacer. A separate stainless steel piece encloses the mode waist to suppress stray electric fields. All of these components, plus vacuum wires, give rise to numerous low-frequency acoustical resonances that couple to the actuator. See Fig. 6.7 for a photograph of the resonator.

The purpose of the piezo is to tune the length of the resonator, which is frequency-modulation locked (the transmission analog of the Pound-Drever-Hall method [65, 26], see Appendix C) to a stable external laser. The feedback controller is an analog proportional-integral (PI) controller, whose output is amplified by a high-voltage piezo-driver before reaching the piezo.

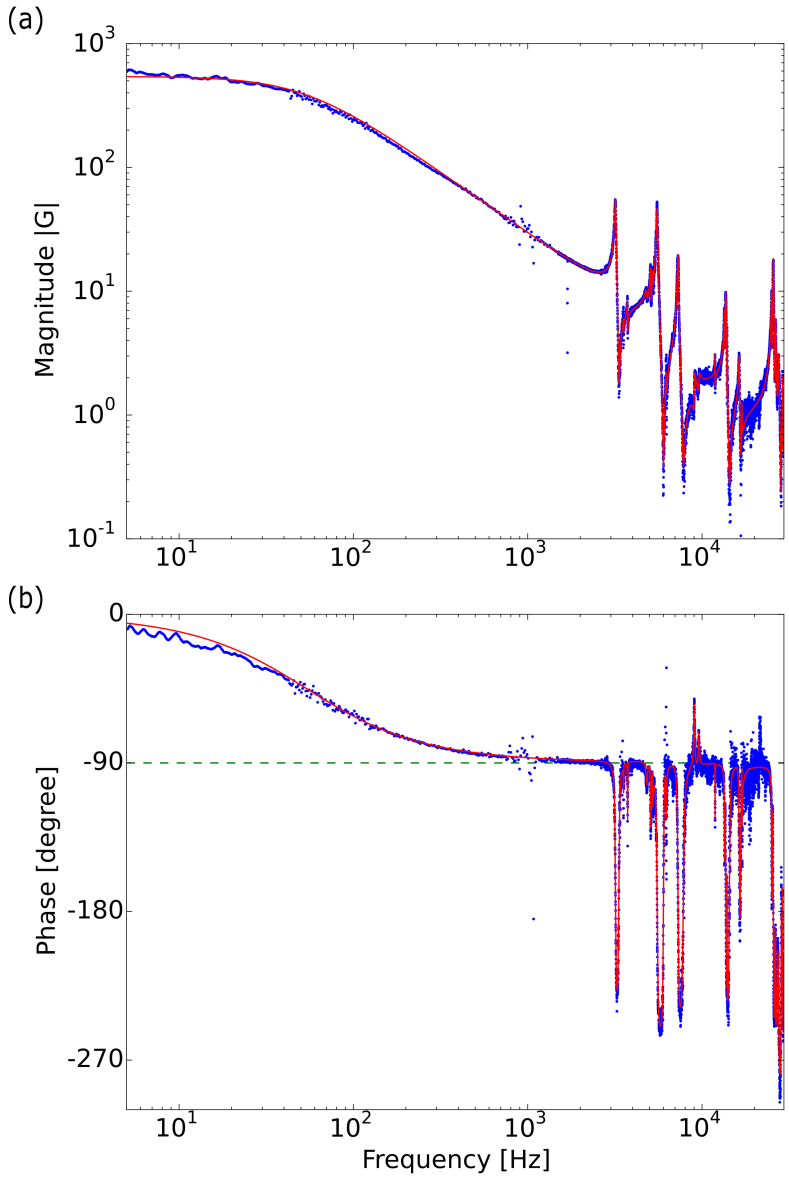

Figure 6.8: **System transfer function** G. (a) Magnitude and (b) phase of the system transfer function versus frequency. Here "system" refers to the piezo-driver, piezo, resonator mirror, photodiode, and down-converting mixer. The measured data (blue) agrees well with a fit (red) composed of a rational function of poles and zeros. The first-order imaginary pole (corner frequency $\omega_{piezo} = 2\pi \times 50$ Hz) is due to the piezo-actuator-piezo-driver low-pass circuit; its $\pi/2$ phase lag is marked with a dashed line in (b). The second-order poles and zeros, appearing in pairs, are the result of constructive and destructive interference between the piezo and mount modes. The phase lag within each pole-zero pair depends on the strength of the coupling between the piezo and the mount, and can be as large as π. The fit to the magnitude data in (a) provides a predicted phase fit in (b) that agrees well with the measured phase, indicating that the system exhibits negligible time delay over the measured frequency range.

6.4.2 Measurement of the system transfer function G

To measure the transfer function G of the full system comprised of the piezo-driver, piezo, mirror, resonator field, and detector, we modulate the reference signal r with a network analyzer (HP3577A) and simultaneously record the ratio of the detector output x over the controller output u, as a function of frequency. For strong modulation, $n \ll x$, and so $G = x/u$.

Figure 6.8 shows the magnitude and the phase of G, measured from 5 Hz to 30 kHz. We observe the first-order pole, coming from the output impedance of the piezo-driver ($\sim$1 MΩ) and the capacitance of the piezo ($\sim$4 nF), with a corner frequency of $\omega_{piezo} = 2\pi \times 50$ Hz. As expected, the phase lag of the first-order pole is $\pi/2$, marked by the dashed line in Figure 6.8b. Past the corner frequency is a $1/f$ decline, on top of which the mechanical resonances and the anti-resonances appear.

The resonances and the anti-resonances are second-order poles and zeros, which come with a phase shift of $-\pi$ and π, respectively. Experimentally, they occur in pairs, arising from the interference between the motion of the piezo and that of other mechanical parts of the resonator (the "mount"): the motion of the piezo excites mount modes, which can back-act on, and hence interfere with, the motion of the piezo itself. Constructive interference results in a pole, while destructive interference causes a zero. Within the pole-zero pair, the phase is nearly π or $-\pi$, depending on the order in which they occur. If the pole and the zero are too close together (if the mount mode is narrow and weakly coupled to the piezo), the phase lag between them is smaller than π. See supplementary information for a physical model of the resonances.

6.4.3 Extraction of the inverse filter parameters

We extract the frequencies and the linewidths of the acoustical resonances by fitting the measured system transfer function G to the minimum-phase mathematical model, Equation (6.6), with $\tau_G = 0$. Figure 6.8 shows the result of a least-squares fit to the magnitude,

Table 6.1: Fitted frequencies and linewidths of largest second-order poles and zeros of the system transfer function G, along with calculated Q values.

Poles			**Zeros**		
Frequency [Hz]	**FWHM [Hz]**	**Q**	**Frequency [Hz]**	**FWHM [Hz]**	**Q**
3190	30	110	3330	30	110
5530	60	90	6000	30	200
7290	70	100	7810	80	100
13700	110	120	14350	140	100
16350	100	160	16600	190	90
25530	400	60	28400	40	710

and plots both the magnitude (Fig. 6.8a) and the phase (Fig. 6.8b). The good agreement between the measured and the calculated phase indicates that the time delay τ_G in the physical system is negligible over the measured frequency range.

While we can fit a near-arbitrary number of features below f_{Nyq} (in Figure 6.8, we fit 28 pole-zero pairs), the most important features when it comes to increasing the feedback bandwidth are the largest poles and zeros. For the FIR filter, we identify and cancel ten pole-zero pairs, treating closely-spaced resonances as single spectral features. The result of this coarse-graining, apparent in all FIR-compensated response curves, is several dB of residual oscillation at the locations of each of the canceled features. In Table 6.1, we list the frequencies, linewidths, and mechanical Q's of six of the ten pairs, corresponding to those shown in Figure 6.8.

6.4.4 Implementation of the FIR filter

The inverse filter F that the FPGA FIR implements is computed by simply exchanging the second-order poles and zeros in G, that is, $F(\omega) = [G(\omega)]^{-1}$, excluding the time delay and the first-order pole. We then generate the filter coefficients a_m by sampling the analytical expression for F up to a maximum frequency f_s and performing an inverse discrete Fourier transform. Figure 6.9 shows the values of the filter coefficients for the inverse filter F.

Figure 6.10 demonstrates our ability to cancel specific poles and zeros of the transfer function G with the FIR filter. The left column shows the magnitude, and the right the

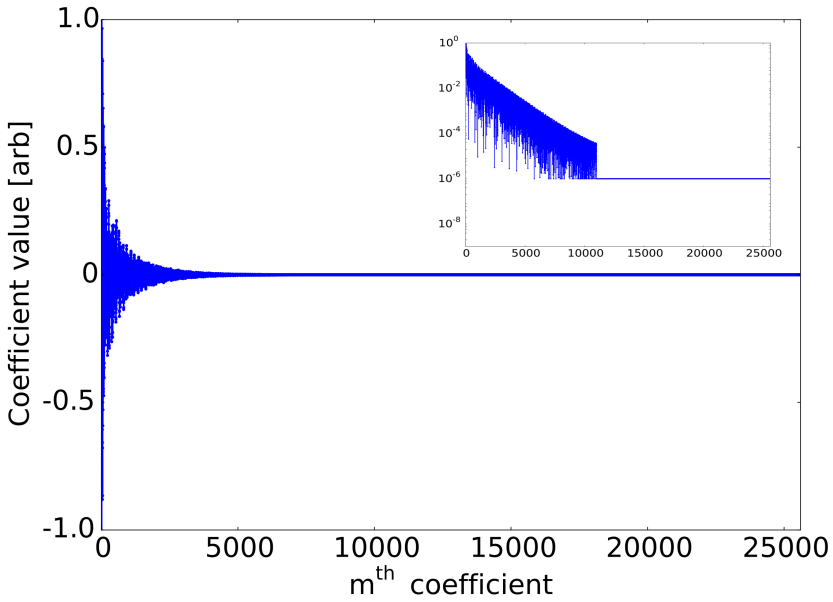

Figure 6.9: **FIR filter coefficients**. The 25,600 filter coefficients that are convolved with the output signal x. (*inset*) Absolute value of the filter coefficients on a log scale; values below quantization error have been truncated.

phase, of GF. The blue curve is the measured GF with $F = 1$, and the red curve is the measured GF, where F is the inverse filter (displayed in green). In Figures 6.10a-c, we selectively cancel each of the first three strongly-coupled mechanical modes; Figure 6.10d shows the cancellation of all six features.

Unlike the phase of the system transfer function G in Figure 6.8, the phase of GF in Figure 6.10 shows an increasing phase lag at higher frequencies, $\phi = \omega\tau$, arising from the $\tau = 2.6$ μs time delay caused by the sampling rate of FPGA FIR filter, as described in Section II.C.

6.4.5 Loop gain and sensitivity

Having canceled the acoustical resonances with the FIR filter, we increase the total gain in the feedback system and hence its bandwidth. We record the ratio of the filtered output y to the error signal e while modulating the reference signal r; then, the loop gain $KGF = y/e$,

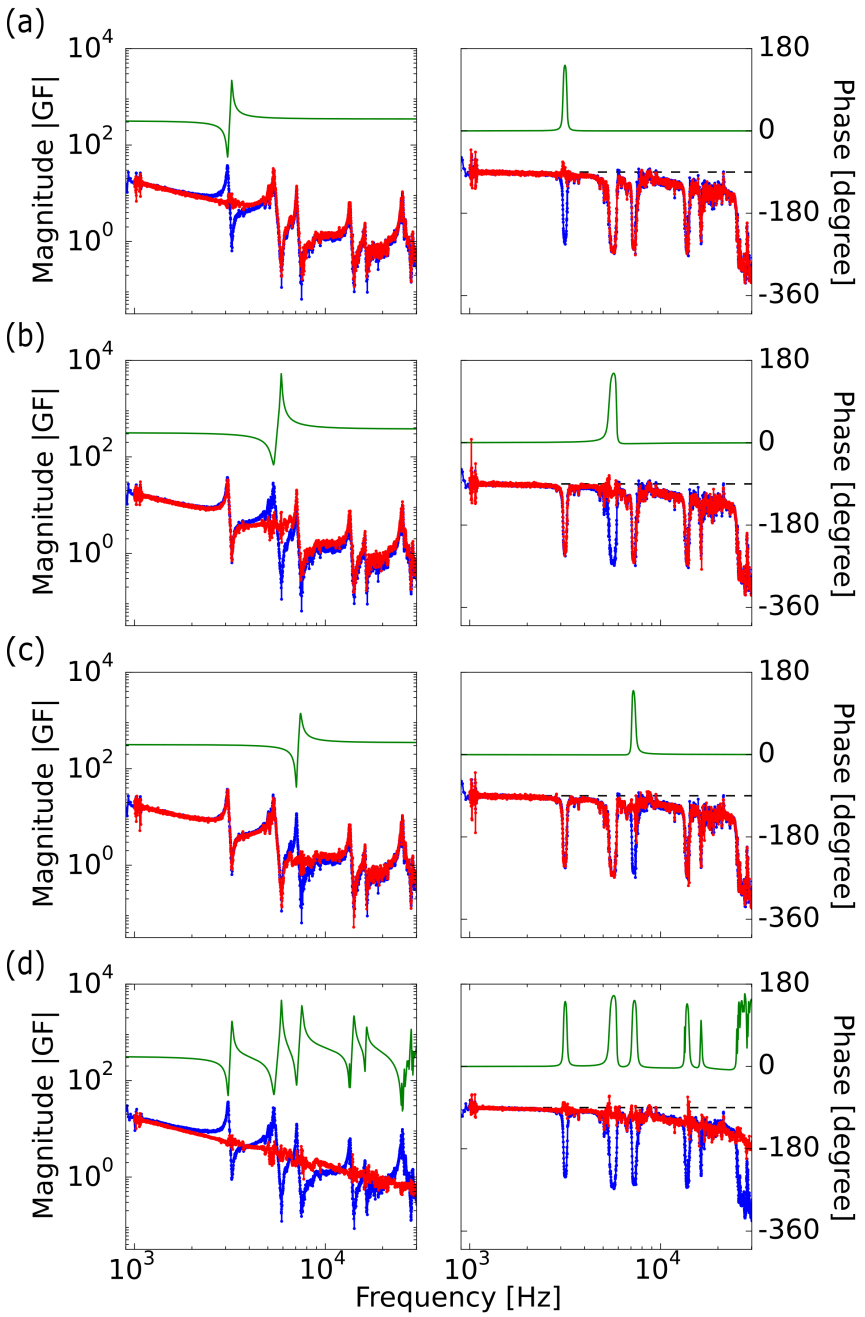

Figure 6.10: **Selective acoustical resonance cancellation using the FPGA FIR filter**. (a-c) Each of the first three pairs; (d) all six pairs. The magnitude and the phase of the measured transfer function GF with $F = 1$ (blue) and $F =$ inverse filter (red) are plotted. Also shown is the calculated transfer function of the inverse filter F (green), not including the 2.6-μs time delay in the digital filter. The magnitude of F has been offset from unity for clarity. The filter-induced time delay results in an increasing phase lag for higher frequency for the measured transfer functions, as shown by the divergence from the horizontal dashed line at -90 degrees.

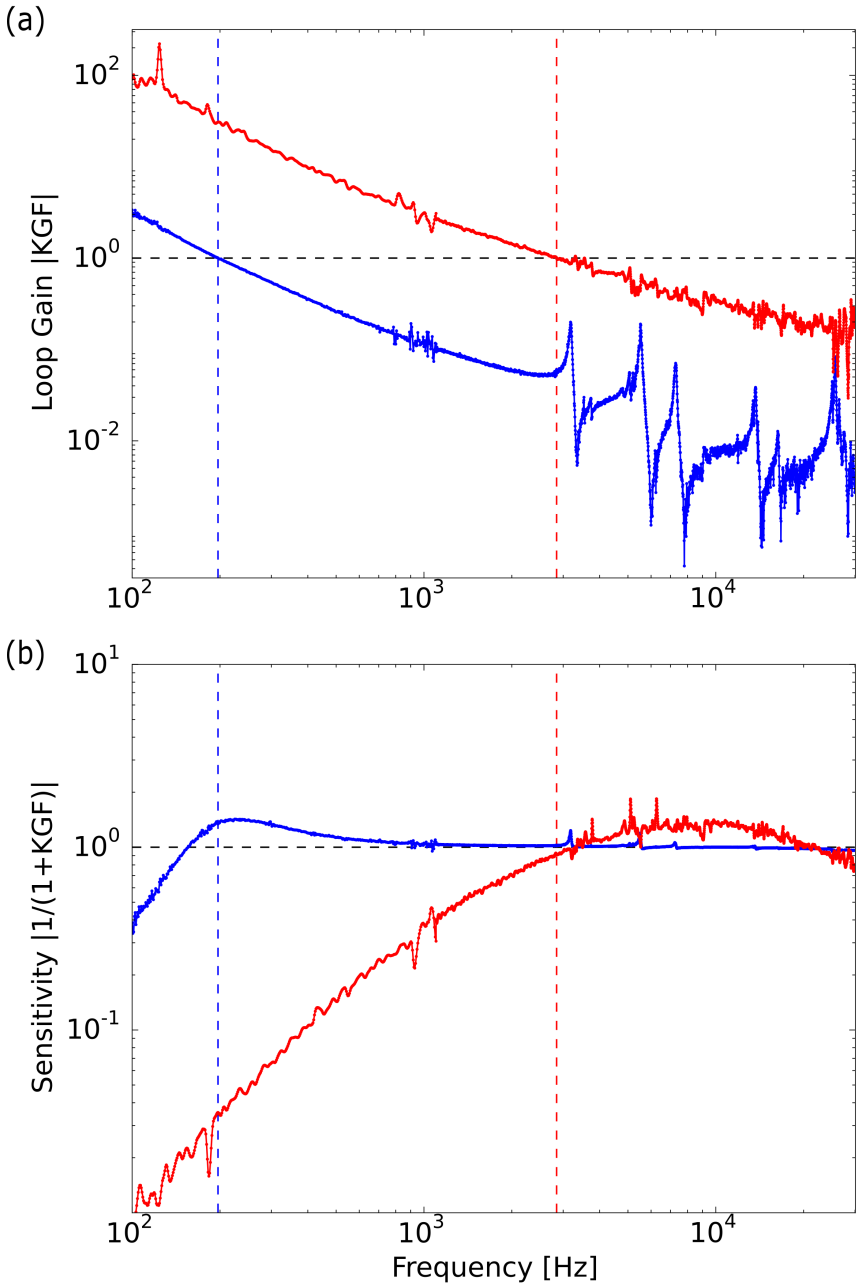

Figure 6.11: **Loop gain and sensitivity**. (a) Magnitude of KGF before (blue) and after (red) implementing the FIR filter to cancel the resonances and increasing the total gain. (b) Corresponding magnitude of the sensitivity (noise suppression factor) $1/(1+KGF)$ before (blue) and after (red). The sensitivity in the uncompensated system displays small peaks at each mechanical resonance; further increasing the total gain, without compensating for the mechanical resonances, would result in noise amplification, and ultimately oscillation, at these resonant frequencies. In both plots, the horizontal dashed line indicates unity gain, and the vertical dashed line indicates the bandwidth (unity gain frequency), which has been enhanced by more than an order of magnitude. The final gain and phase margins are 4 and 70°, respectively.

and the sensitivity $1/(1+KGF) = e/r$ (see supplementary information for the calculation of the sensitivity).

Figure 6.11 shows the magnitude of (a) the loop gain and (b) the sensitivity before (blue) and after (red) implementing the FIR filter and increasing the total gain. Note that the unity-gain bandwidth has been increased by more than an order of magnitude from 200 Hz to 2.8 kHz, marked by the vertical dashed lines.

Figure 6.11b shows the corresponding sensitivity. The noise suppression occurs up to the bandwidth and then saturates at unity, where a servo bump is observed. For the uncompensated configuration, the strong servo bump is the result of a mismatch between the corner frequencies of $K(\omega = 2\pi \times 200$ Hz) and $GF(\omega = 2\pi \times 50$ Hz), leading to excess phase lag at unity gain.

The maximum compensated bandwidth of 2.8 kHz is set by the presence of additional resonances beyond the Nyquist frequency of the FPGA FIR filter, including the piezo/mirror resonances (see supplementary information). The final gain and phase margins are 4 and 70°, respectively, indicating a robust lock [66].

6.4.6 Temporal drift of open-loop response

If the transfer function varies in time, the FIR filter coefficients must be adjusted accordingly. For our optical resonator, the resonances have high Q values and can shift by as much as a linewidth as the piezo voltage (and hence its stiffness) changes in response to temperature variation of the resonator mount [67].

The FPGA-based approach allows us to implement a complete, high-signal-to-noise vector network analyzer within Red Pitaya (similar to that distributed by the manufacturer, but independently implemented and integrated with the FIR filter), and use it to continuously characterize the system. In Figure 6.12, we plot the frequency response versus piezo voltage, tuned in-lock, over a period of hours, by heating the entire resonator structure with in-chamber heating coils. It demonstrates that the mechanical resonances shift by about

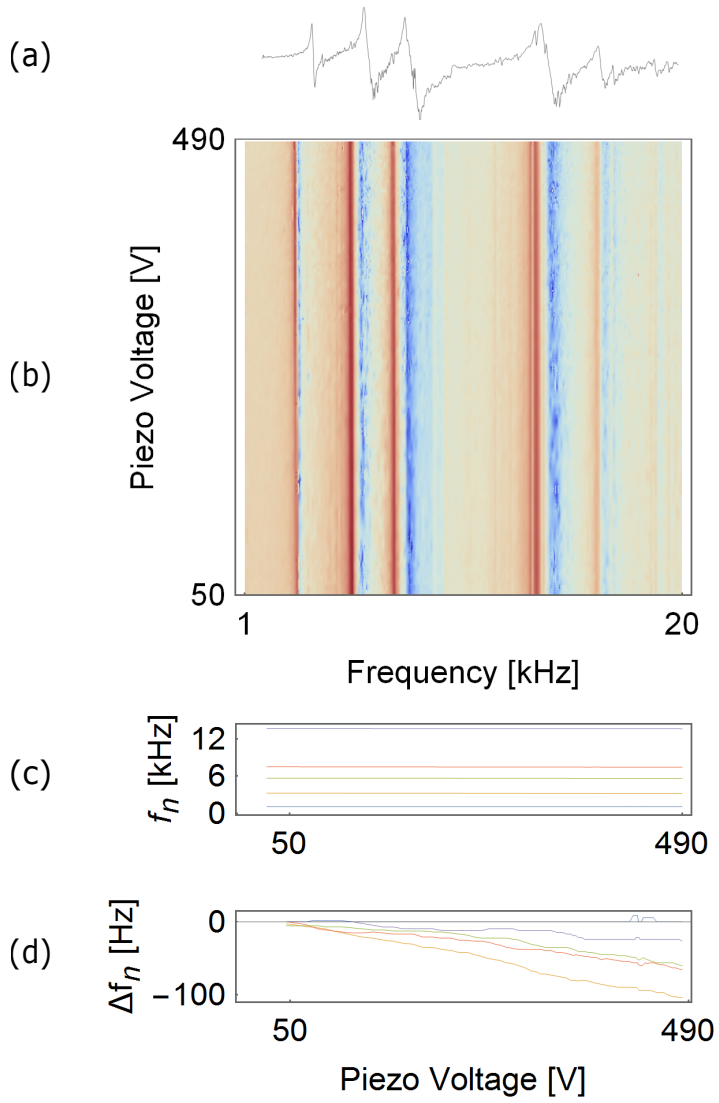

Figure 6.12: **Monitoring resonance drift with FPGA vector network analyzer. (a)** Sample spectrum measured with a VNA implemented within the FPGA, collected with a RBW of ~ 8 Hz, and 5-point boxcar video averaging. **(b)** We smoothly vary the piezo voltage by heating the resonator structure (with in-chamber heating wire) and observe the variation of the piezo resonance frequencies. All spectra have been multiplied by ω^2 to remove the overall piezo-driver and integrator induced rolloffs. The fine structure in (a) persists across (b), indicating that it is not noise, but is in fact a forest of weakly-coupled mechanical resonances and symmetry-broken splittings of primary resonances. **(c)** The frequencies of the dominant poles, extracted via peak finding, demonstrate coarse stability of resonance locations as the piezo voltage is tuned. **(d)** The fine variation of the pole locations, relative to their zero-piezo-voltage value and smoothed over five adjacent scans (piezo voltages) to reduce noise, demonstrates ~ 100 Hz of resonance tuning over the full piezo voltage range, which is comparable to the resonance linewidths.

one linewidth over the full piezo voltage range. Since the resonances can be continuously monitored by weak modulation of the feedback system while in lock, the FIR filter could be modified to track them in real time. The scan time of ~ 10 minutes is necessary to achieve sufficient signal-to-noise in a *full* high-resolution scan, which is amply fast for this task. In addition, this time can be substantially reduced by scanning only near the poles and zeros to be canceled. At a RBW of 10 Hz, we acquire ~ 3 points per second, and thus can realistically update the locations of all poles and zeros approximately once per minute.

6.4.7 Absolute noise in the system

Figure 7 in the main text shows the FIR filter's ability to cancel the acoustical resonances and increase the feedback bandwidth, resulting in the enhanced noise suppression factor. It does not demonstrate, however, that the system itself has actually become quieter (see discussion on the filter noise below). In Figure 6.13, we measure the absolute noise of a non-evacuated table-top resonator with and without incorporating the FIR filter (the previous four-mirror resonator has become unavailable since the initial paper submission). The top plot shows the sensitivity, as in Figure 6.11b in the main text. The noise suppression is enhanced by canceling the acoustical resonances with the FIR filter and increasing the feedback bandwidth from 2 kHz to 7 kHz. The red curve shows that imperfectly canceled features bumped above unity gain are amplified. The bottom plot shows the corresponding absolute noise in the system output x (*before* it gets conditioned by the FIR filter) as a function of frequency. For low frequency, an order-of-magnitude noise reduction is observed, demonstrating that the FIR filter has indeed made the system quieter.

6.5 Conclusion

We have demonstrated that a low-latency FPGA-based FIR filter is an extremely versatile tool for implementing sophisticated control schemes. With a sampling rate of ~ 250 kHz,

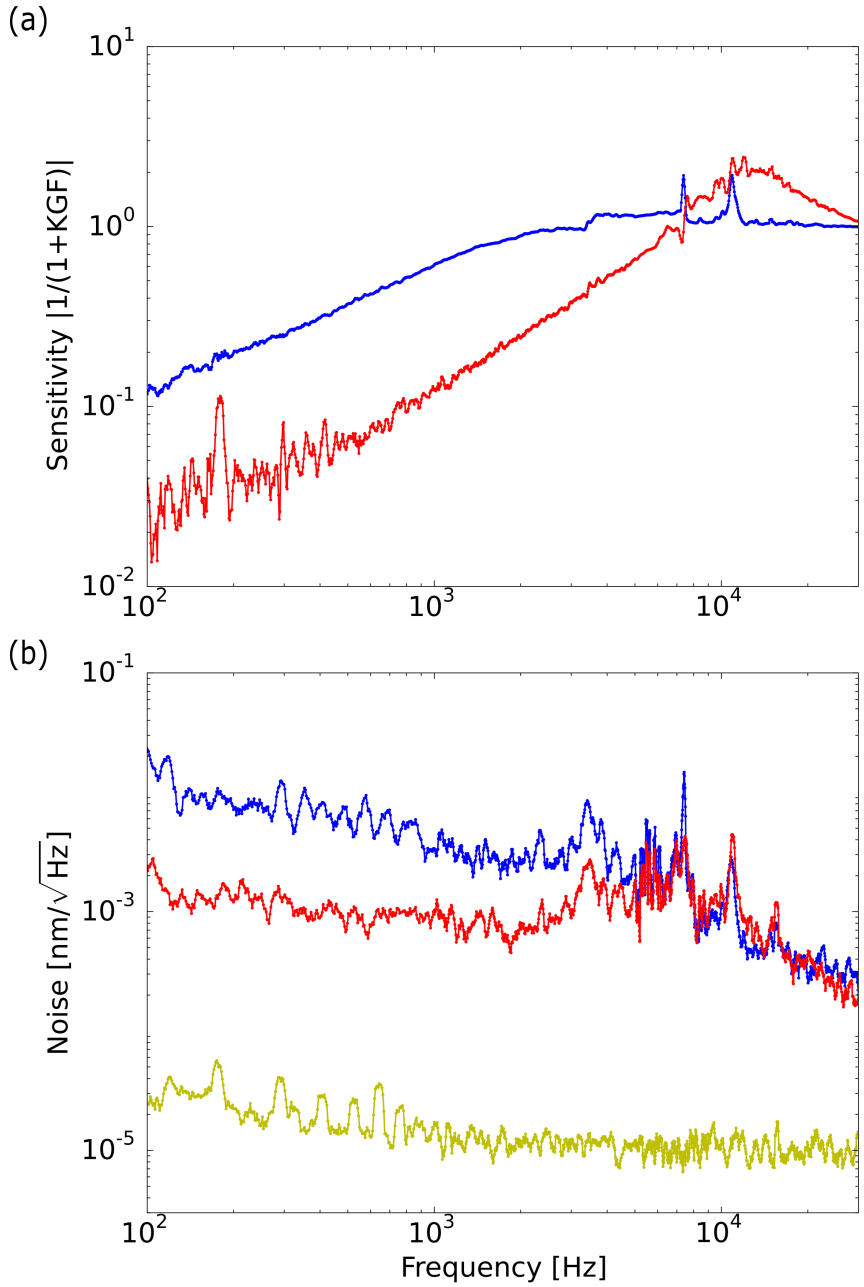

Figure 6.13: **Absolute noise reduction.** (top) Magnitude of the sensitivity $1/(1+KGF)$ without the FIR filter (blue, bandwidth $\sim$ 2 kHz) and with the FIR filter (red, bandwidth $\sim$ 7 kHz). (bottom) Corresponding absolute noise in the system output x without (blue) and with (red) the FIR filter. By canceling the resonances and increasing the bandwidth, the FIR filter yields about an order-of-magnitude noise reduction. The yellow curve indicates the detection noise floor with the incident optical power on the photodiode comparable to that while the system is in lock.

a memory time $\sim$ 0.1 seconds, and a delay of $\sim$ 2.6μs, the filter is capable of canceling numerous acoustical resonances, thereby enhancing mechanical noise suppression far beyond what is practical in an analog compensator. In addition to demonstrating the requisite FPGA FIR architecture, we introduce a minimal characterization scheme for the mechanical system that provides all parameters of the FIR filter in a single shot, implementing a VNA within the FPGA. We employ this approach to increase the noise-suppression bandwidth of a locked optical resonator by an order of magnitude.

Our approach is broadly applicable to many fields that employ actively stabilized mechanical systems, including atomic microscopy, where it could be used to enhance the stability of the scanning tip [68, 69] as an alternative to sophisticated flexures [70], and gravitational wave detection, where it could suppress noise in the seismic stacks [71, 72, 73]. The technique is directly extendable to higher frequency low-latency loop-shaping at the expense of suppression of either lower Q features or substantially larger FPGAs. The flexibility of this tool further suggests possibilities in control beyond the delay-limited bandwidth to provide narrowband, high-frequency noise suppression.

CHAPTER 7

OUTLOOK

We have demonstrated the first single-photon nonlinearity using Rydberg EIT in an atomic ensemble in an optical cavity. The single-body properties of the dark-state polariton have been characterized, including the frequency compression, as well as the temporal intensity correlation of the transmitted light, with $g_2(0) < 0.3$ and $g_2(0) < g_2(\tau)$, showing both sub-Poissonian and antibunched distribution of photons.

We have also observed multimode EIT using two nearly degenerate cavity modes. Combining Rydberg EIT with a twisted cavity with a Landau level of many degenerate modes should imbue the polaritons with an effective mass, allowing us to study polaritonic crystallization and emergent lattices as well as fractional quantum Hall physics.

The study of polariton-polariton scattering in future experiments should be greatly facilitated by the use of the DMD for selective mode injection whose coupling efficiency can reach more than 99%. Furthermore, exotic cavity configurations possessing numerous acoustical resonances could be feedback-stabilized using the FPGA-based FIR filter, for instance, from 200 Hz to more than 2 kHz, allowing us to rapidly switch probing between different cavity resonances within the same experimental sequence.

REFERENCES

[1] Mazurenko, A. *et al.* Experimental realization of a long-range antiferromagnet in the hubbard model with ultracold atoms. *arXiv preprint arXiv:1612.08436* (2016).

[2] Bloch, I., Dalibard, J. & Nascimbene, S. Quantum simulations with ultracold quantum gases. *Nature Physics* **8**, 267 (2012).

[3] Duan, L.-M., Demler, E. & Lukin, M. D. Controlling spin exchange interactions of ultracold atoms in optical lattices. *Physical review letters* **91**, 090402 (2003).

[4] Bloch, I., Dalibard, J. & Zwerger, W. Many-body physics with ultracold gases. *Reviews of modern physics* **80**, 885 (2008).

[5] Deng, H., Haug, H. & Yamamoto, Y. Exciton-polariton bose-einstein condensation. *Reviews of Modern Physics* **82**, 1489 (2010).

[6] Simon, J., Tanji, H., Thompson, J. K. & Vuletić, V. Interfacing collective atomic excitations and single photons. *Physical review letters* **98**, 183601 (2007).

[7] Akimov, A. *et al.* Generation of single optical plasmons in metallic nanowires coupled to quantum dots. *Nature* **450**, 402–406 (2007).

[8] Carusotto, I. & Ciuti, C. Quantum fluids of light. *Reviews of Modern Physics* **85**, 299 (2013).

[9] Fleischhauer, M., Imamoglu, A. & Marangos, J. P. Electromagnetically induced transparency: Optics in coherent media. *Reviews of modern physics* **77**, 633 (2005).

[10] Saffman, M., Walker, T. G. & Mølmer, K. Quantum information with rydberg atoms. *Reviews of Modern Physics* **82**, 2313 (2010).

[11] Pritchard, J. D. *et al.* Cooperative atom-light interaction in a blockaded rydberg ensemble. *Physical review letters* **105**, 193603 (2010).

[12] Gorshkov, A. V., Otterbach, J., Fleischhauer, M., Pohl, T. & Lukin, M. D. Photon-photon interactions via rydberg blockade. *Physical review letters* **107**, 133602 (2011).

[13] Dudin, Y. & Kuzmich, A. Strongly interacting rydberg excitations of a cold atomic gas. *Science* **336**, 887–889 (2012).

[14] Peyronel, T. *et al.* Quantum nonlinear optics with single photons enabled by strongly interacting atoms. *Nature* **488**, 57–60 (2012).

[15] Firstenberg, O. *et al.* Attractive photons in a quantum nonlinear medium. *Nature* **502**, 71–75 (2013).

[16] Kimble, H. J. Strong interactions of single atoms and photons in cavity qed. *Physica Scripta* **1998**, 127 (1998).

[17] Hood, C., Chapman, M., Lynn, T. & Kimble, H. Real-time cavity qed with single atoms. *Physical review letters* **80**, 4157 (1998).

[18] Boca, A. *et al.* Observation of the vacuum rabi spectrum for one trapped atom. *Physical review letters* **93**, 233603 (2004).

[19] Birnbaum, K. M. *et al.* Photon blockade in an optical cavity with one trapped atom. *Nature* **436**, 87–90 (2005).

[20] Chang, D. *et al.* Crystallization of strongly interacting photons in a nonlinear optical fibre. *Nature Physics* **4**, 884–889 (2008).

[21] Haroche, S. & Kleppner, D. Cavity quantum electrodynamics. *Physics Today* **42**, 24–30 (1989).

[22] Vahala, K. J. Optical microcavities. *Nature* **424**, 839–846 (2003).

[23] Reiserer, A., Ritter, S. & Rempe, G. Nondestructive detection of an optical photon. *Science* **342**, 1349–1351 (2013).

[24] Kimble, H. J. The quantum internet. *Nature* **453**, 1023–1030 (2008).

[25] Siegman, A. *Lasers* (University Science Books, 1986). URL `https://books.google.com/books?id=1BZVwUZLTkAC`.

[26] Black, E. D. An introduction to pound–drever–hall laser frequency stabilization. *American Journal of Physics* **69**, 79–87 (2001).

[27] Yuan, J. *et al.* Nonplanar ring resonator modes: generalized gaussian beams. *Applied optics* **46**, 2980–2989 (2007).

[28] Metcalf, H. J. & Van der Straten, P. *Laser cooling and trapping* (Springer Science & Business Media, 2012).

[29] Hulet, R. G., Hilfer, E. S. & Kleppner, D. Inhibited spontaneous emission by a rydberg atom. *Physical review letters* **55**, 2137 (1985).

[30] Haroche, S. & Raimond, J.-M. Cavity quantum electrodynamics. *Scientific American* **268**, 54–60 (1993).

[31] Shore, B. W. & Knight, P. L. The jaynes-cummings model. *Journal of Modern Optics* **40**, 1195–1238 (1993).

[32] Lee, J. *et al.* Demonstration of the jaynes-cummings ladder with rydberg-dressed atoms. *Physical Review A* **95**, 041801 (2017).

[33] Tanji-Suzuki, H. *et al.* Interaction between atomic ensembles and optical resonators: classical description. *arXiv preprint arXiv:1104.3594* (2011).

[34] Jia, N. *et al.* A strongly interacting polaritonic quantum dot. *arXiv preprint arXiv:1705.07475* (2017).

[35] Ningyuan, J. *et al.* Observation and characterization of cavity rydberg polaritons. *Physical Review A* **93**, 041802 (2016).

[36] Poirson, J., Bretenaker, F., Vallet, M. & Le Floch, A. Analytical and experimental study of ringing effects in a fabry–perot cavity. application to the measurement of high finesses. *JOSA B* **14**, 2811–2817 (1997).

[37] Lerner, V., Shwa, D., Drori, Y. & Katz, N. Shaping laguerre–gaussian laser modes with binary gratings using a digital micromirror device. *Optics letters* **37**, 4826–4828 (2012).

[38] Čižmár, T., Mazilu, M. & Dholakia, K. In situ wavefront correction and its application to micromanipulation. *Nature Photonics* **4**, 388–394 (2010).

[39] Zupancic, P. *et al.* Ultra-precise holographic beam shaping for microscopic quantum control. *Optics express* **24**, 13881–13893 (2016).

[40] Schine, N., Ryou, A., Gromov, A., Sommer, A. & Simon, J. Synthetic landau levels for photons. *Nature* **534**, 671–675 (2016).

[41] Zupancic, P. P. Dynamic holography and beamshaping using digital micromirror devices. *LMU Münich, Grainer Lab Harvard* **242** (2013).

[42] Mair, A., Vaziri, A., Weihs, G. & Zeilinger, A. Entanglement of the orbital angular momentum states of photons. *Nature* **412**, 313–316 (2001).

[43] Deutsch, B., Hillenbrand, R. & Novotny, L. Near-field amplitude and phase recovery using phase-shifting interferometry. *Optics express* **16**, 494–501 (2008).

[44] Bechhoefer, J. Feedback for physicists: A tutorial essay on control. *Reviews of Modern Physics* **77**, 783 (2005).

[45] Sinclair, L. *et al.* Invited article: A compact optically coherent fiber frequency comb. *Review of Scientific Instruments* **86**, 081301 (2015).

[46] Chadi, A., Méjean, G., Grilli, R. & Romanini, D. Note: Simple and compact piezoelectric mirror actuator with 100 khz bandwidth, using standard components. *Review of Scientific Instruments* **84**, 056112 (2013).

[47] Notcutt, M., Ma, L.-S., Ye, J. & Hall, J. L. Simple and compact 1-hz laser system via an improved mounting configuration of a reference cavity. *Optics letters* **30**, 1815–1817 (2005).

[48] Briles, T. C., Yost, D. C., Cingöz, A., Ye, J. & Schibli, T. R. Simple piezoelectric-actuated mirror with 180 khz servo bandwidth. *Optics express* **18**, 9739–9746 (2010).

[49] Singer, N., Singhose, W. & Kriikku, E. An input shaping controller enabling cranes to move without sway. In *ANS 7th topical meeting on robotics and remote systems*, vol. 1, 225–31 (1997).

[50] Croft, D. & Devasia, S. Vibration compensation for high speed scanning tunneling microscopy. *Review of Scientific Instruments* **70**, 4600–4605 (1999).

[51] Schitter, G. & Stemmer, A. Identification and open-loop tracking control of a piezoelectric tube scanner for high-speed scanning-probe microscopy. *Control Systems Technology, IEEE Transactions on* **12**, 449–454 (2004).

[52] Ha, C.-W., Rew, K.-H. & Kim, K.-S. Robust zero placement for motion control of lightly damped systems. *Industrial Electronics, IEEE Transactions on* **60**, 3857–3864 (2013).

[53] Yang, G., Barry, J., Shuman, E., Steinecker, M. & DeMille, D. A low-cost, fpga-based servo controller with lock-in amplifier. *Journal of Instrumentation* **7**, P10026 (2012).

[54] Schwettmann, A., Sedlacek, J. & Shaffer, J. P. Field-programmable gate array based locking circuit for external cavity diode laser frequency stabilization. *Review of Scientific Instruments* **82**, 103103 (2011).

[55] Sparkes, B. *et al.* A scalable, self-analyzing digital locking system for use on quantum optics experiments. *Review of Scientific Instruments* **82**, 075113 (2011).

[56] Leibrandt, D. & Heidecker, J. An open source digital servo for atomic, molecular, and optical physics experiments. *Review of Scientific Instruments* **86**, 123115 (2015).

[57] Do, T.-T., Kropp, H., Reuter, C. & Pirsch, P. A flexible implementation of high-performance fir filters on xilinx fpgas. In *Field-Programmable Logic and Applications From FPGAs to Computing Paradigm*, 441–445 (Springer, 1998).

[58] Evans, J. B. Efficient fir filter architectures suitable for fpga implementation. *IEEE Transactions on Circuits and Systems-Part II-Analog and Digital Signal Processing* **41**, 490–492 (1994).

[59] Chou, C.-J., Mohanakrishnan, S. & Evans, J. B. Fpga implementation of digital filters. In *Proc. ICSPAT*, vol. 93, 1 (Citeseer, 1993).

[60] Yoo, H. & Anderson, D. V. Hardware-efficient distributed arithmetic architecture for high-order digital filters. In *Acoustics, Speech, and Signal Processing, 2005. Proceedings.(ICASSP'05). IEEE International Conference on*, vol. 5, v–125 (IEEE, 2005).

[61] Ryou, A. & Simon, J. Active cancellation of acoustical resonances with an fpga fir filter. *Review of Scientific Instruments* **88**, 013101 (2017).

[62] Wiener, N. *The human use of human beings: Cybernetics and society*. 320 (Perseus Books Group, 1954).

[63] Dorf, R. C. *Modern control systems* (Addison-Welsey Publishing Company, Menlo Park, California, 1992).

[64] Oppenheim, A. V., Schafer, R. W., Buck, J. R. *et al. Discrete-time signal processing*, vol. 2 (Prentice Hall Englewood Cliffs, NJ, 1989).

[65] Drever, R. *et al.* Laser phase and frequency stabilization using an optical resonator. *Applied Physics B* **31**, 97–105 (1983).

[66] Mosk, A. Tutorial on experimental physics of ultracold gases. *Interactions in Ultracold Gases: From Atoms to Molecules* 215–256 (2005).

[67] Waanders, J. *Piezoelectric ceramics: properties and applications* (NV Philips' Gloeilampenfabrieken, 1991).

[68] Binnig, G. & Rohrer, H. The scanning tunneling microscope. *Scientific American* **253**, 50–69 (1985).

[69] Binnig, G., Quate, C. F. & Gerber, C. Atomic force microscope. *Physical review letters* **56**, 930 (1986).

[70] Kenton, B. J., Fleming, A. J. & Leang, K. K. Compact ultra-fast vertical nanopositioner for improving scanning probe microscope scan speed. *Review of Scientific Instruments* **82**, 123703 (2011).

[71] Abbott, B. *et al.* Observation of gravitational waves from a binary black hole merger. *Physical Review Letters* **116**, 061102 (2016).

[72] Hardham, C. *et al. Quiet hydraulic actuators for LIGO.* Ph.D. thesis, Stanford University (2005).

[73] Matichard, F. *et al.* Seismic isolation of advanced ligo: Review of strategy, instrumentation and performance. *Classical and Quantum Gravity* **32**, 185003 (2015).

[74] Simon, J. *Cavity QED with atomic ensembles* (Harvard University, 2010).

APPENDIX A

COUPLING EFFICIENCY BETWEEN TWO GAUSSIAN BEAMS

Coupling one Gaussian beam with another, which arises in both cavity mode matching and optical fiber coupling, requires matching both the beam size and the wavefront curvature. Here we derive the coupling efficiency between two TEM_{00} modes.

The general expression for the coupling between the modes $u_1(x)$ and $u_2(x)$ is given by

$$c = \frac{\left|\int u_1^*(x) u_2(x)\, dx\right|^2}{\int u_1^*(x) u_1(x)\, dx \int u_2^*(x) u_2(x)\, dx} \tag{A.1}$$

The normalized TEM_{00} is given by

$$u(r,z) = \left(\frac{2}{\pi w^2}\right)^{1/2} \exp\left[-\frac{r^2}{w^2} - ikz - \frac{i\pi r^2}{\lambda R} + i\tan^{-1}\left(\frac{z}{z_R}\right)\right] \tag{A.2}$$

where $w = w(z)$ and $R = R(z)$. In addition, it is assumed that the mode is cylindrically symmetric, i.e. there is no astigmatism.

We re-write the mode in terms of the q paramter and its reciprocal:

$$q = z + iz_R \tag{A.3}$$

$$\frac{1}{q} = \frac{1}{R} - i\frac{\lambda}{\pi w^2} \tag{A.4}$$

$$u(r) = \left(-\frac{2}{\lambda}\mathrm{Im}\left[\frac{1}{q}\right]\right)^{1/2} \exp\left[-i\frac{k}{2q}r^2 - ik\mathrm{Re[q]} + i\tan^{-1}\left(\frac{\mathrm{Re[q]}}{\mathrm{Im[q]}}\right)\right] \tag{A.5}$$

Due to the normalization, the terms in the denominator in Eq. 1.1 are unity, leaving

$$c = \left|\int_0^\infty u_1^*(r) u_2(r) 2\pi r\, dr\right|^2 \tag{A.6}$$

where we have used the xy symmetry to convert $dx\, dy \to 2\pi r\, dr$.

Proceeding with the conjugation under the integral:

$$u_1^*(r)u_2(r) = \exp\left[i\frac{k}{2}r^2\left(\frac{1}{\mathrm{Re}[q_1] - i\mathrm{Im}[q_1]} - \frac{1}{\mathrm{Re}[q_2] + i\mathrm{Im}[q_2]}\right) + id\right] \tag{A.7}$$

$$d = k\left(\mathrm{Re}[q_1] - \mathrm{Re}[q_2]\right) + \left\{\tan^{-1}\left(\frac{\mathrm{Re}[q_2]}{\mathrm{Im}[q_2]}\right) - \tan^{-1}\left(\frac{\mathrm{Re}[q_1]}{\mathrm{Im}[q_1]}\right)\right\} \tag{A.8}$$

Then, we make use of the following integral,

$$\int_0^\infty xe^{(a+ib)x^2+id}\,dx = -\frac{e^{id}}{2(a+ib)} \tag{A.9}$$

and note that d drops out upon performing the conjugate square.

Thus,

$$a = \frac{-k}{2|q_1|^2|q_2|^2}\left(|q_2|^2\mathrm{Im}[q_1] + |q_1|^2\mathrm{Im}[q_2]\right) \tag{A.10}$$

$$b = \frac{k}{2|q_1|^2|q_2|^2}\left(|q_2|^2\mathrm{Re}[q_1] - |q_1|^2\mathrm{Re}[q_2]\right) \tag{A.11}$$

and, after cancelling terms,

$$c = \frac{4\mathrm{Im}[q_1]\mathrm{Im}[q_2]}{|q_1|^2 + |q_2|^2 + 2\left(\mathrm{Im}[q_1]\mathrm{Im}[q_2] - \mathrm{Re}[q_1]\mathrm{Re}[q_2]\right)} \tag{A.12}$$

For counter-propagating beams, for which q_1 and q_2 at a specified z have been propagated from opposite directions, we need to flip the sign of the wavefront curvature R for one of the beams, or, in what amounts to the same thing, flip the sign of its real part: $\mathrm{Re}[q_2] \to -\mathrm{Re}[q_2]$. The coupling efficiency then becomes

$$c = \frac{4\mathrm{Im}[q_1]\mathrm{Im}[q_2]}{|q_1 + q_2|^2} \tag{A.13}$$

Note that the coupling is independent of the specific z-plane one chooses to evaluate the q parameters.

APPENDIX B

CALCULATIONS USING THE PERTURBATION THEORY FOR NON-HERMITIAN HAMILTONIANS

B.1 Introduction

Our experimental probe for the atom-cavity system is the cavity transmission, which is used to observe vacuum Rabi splitting, electromagnetically induced transparency, and photon statistics. In this appendix, I explicitly calculate the transmission and $g_2(0)$ for two- and three-level atoms coupled to single-mode cavities, using a generalized Jaynes-Cummings (sometimes called the Tavis-Cummings) model. The perturbation theory for non-hermitian Hamiltonians is described in Appendix B of Jonathan Simon's PhD thesis [74].

B.2 Perturbation theory

The n^{th}-order corrections to the unperturbed eigenvalues and eigenstates are related by

$$H^0 |\psi^n\rangle + V |\psi^{n-1}\rangle = \sum_{m=0}^{n} \epsilon^m |\psi^{n-m}\rangle \tag{B.1}$$

where H^0 is the unperturbed Hamiltonian and V is the perturbation.

The standard perturbation theory proceeds by performing a dot product of the above equation with unperturbed eigenvectors, relying on their orthogonality, $\langle\psi_i^0|\psi_j^0\rangle = \delta_{ij}$, to systematically find higher-order corrections $|\psi^n\rangle$. This orthogonality, however, is not guaranteed for eigenvectors of non-hermitian Hamiltonians.

Let $|\psi^0\rangle$ be an unperturbed eigenstate. We assume $|\psi^0\rangle$ is orthogonal to all higher-order corrections. Performing a dot product of $\langle\psi^0|$ with Equation B.1 and solving for ϵ^n:

$$\langle\psi^0| \left(H^0 |\psi^n\rangle + V |\psi^{n-1}\rangle = \sum_{m=0}^{n} \epsilon^m |\psi^{n-m}\rangle \right) \tag{B.2}$$

$$\epsilon^0 \langle\psi^0|\psi^n\rangle + \langle\psi^0| V |\psi^{n-1}\rangle = \epsilon^n \langle\psi^0|\psi^0\rangle + \sum_{m=1}^{n-1} \epsilon^m \langle\psi^0|\psi^{n-m}\rangle + \epsilon^0 \langle\psi^0|\psi^n\rangle \tag{B.3}$$

$$\epsilon^n = \langle\psi^0| V |\psi^{n-1}\rangle - \sum_{m=1}^{n-1} \epsilon^m \langle\psi^0|\psi^{n-m}\rangle \tag{B.4}$$

Now we solve for $|\psi^n\rangle$ in Equation 1.1:

$$H^0 |\psi^n\rangle + V |\psi^{n-1}\rangle = \epsilon^0 |\psi^n\rangle + \sum_{m=1}^{n} \epsilon^m |\psi^{n-m}\rangle \tag{B.5}$$

$$|\psi^n\rangle = X^{-1} \left(\sum_{m=1}^{n} e^m |\psi^{n-m}\rangle - V |\psi^{n-1}\rangle \right) \tag{B.6}$$

where $X^{-1} = (H^0 - \epsilon^0 I)^{-1}$ denotes an inverse matrix. Note that the inverse can act only on the subspace of eigenvectors excluding $|\psi^0\rangle$. Thus, we choose

$$X^{-1} \to X^{-1} Q \tag{B.7}$$

where $Q = I - |\psi^0\rangle \langle\psi^0|$ is an operator that projects onto the subspace orthogonal to $|\psi^0\rangle$.

Equations 1.4 and 1.6 form recursive relations, from which all high-order corrections can be computed. The first- and second-order corrections are:

$$\epsilon^1 = \langle\psi^0| V |\psi^0\rangle = 0 \quad (assume) \tag{B.8}$$

$$|\psi^1\rangle = X^{-1} Q \left(e^1 |\psi^0\rangle - V |\psi^0\rangle \right) \tag{B.9}$$

$$= - \left(X^{-1} Q \right) V |\psi^0\rangle \tag{B.10}$$

$$\epsilon^2 = \langle\psi^0| V |\psi^1\rangle - \epsilon^1 \langle\psi^0|\psi^1\rangle \tag{B.11}$$

$$= - \langle\psi^0| V (X^{-1} Q) V |\psi^0\rangle \tag{B.12}$$

$$|\psi^2\rangle = X^{-1} Q \left(e^1 |\psi^1\rangle + \epsilon^2 |\psi^0\rangle - V |\psi^1\rangle \right) \tag{B.13}$$

$$= \left(X^{-1} Q \right) V \left(X^{-1} Q \right) V |\psi^0\rangle \tag{B.14}$$

noting that $\epsilon^2 |\psi^0\rangle \to 0$ when acted on by Q.

B.3 Empty cavity

Let a single-mode cavity with resonant frequency ω_c and decay rate κ be weakly driven by a laser with frequency ω_l with coupling strength Ω. The Hamiltonian up to the second excitation manifold is given by

$$H = H^0 + V \tag{B.15}$$

$$= \begin{pmatrix} 2\omega_l & 0 & 0 \\ 0 & \omega_l + \omega_c - i\kappa/2 & 0 \\ 0 & 0 & 2(\omega_c - i\kappa/2) \end{pmatrix} + \Omega \begin{pmatrix} 0 & 1 & 0 \\ 1 & 0 & \sqrt{2} \\ 0 & \sqrt{2} & 0 \end{pmatrix} \tag{B.16}$$

where $|0\rangle = \begin{pmatrix} 1 \\ 0 \\ 0 \end{pmatrix}$, $|1\rangle = \begin{pmatrix} 0 \\ 1 \\ 0 \end{pmatrix}$, $|2\rangle = \begin{pmatrix} 0 \\ 0 \\ 1 \end{pmatrix}$ represent the cavity with zero, one, and two cavity photons, respectively.

Let the initial state be $|\psi^0\rangle = |0\rangle$. The first-order correction to the state is given by

$$|\psi^1\rangle = -\left(X^{-1}Q\right) V |\psi^0\rangle \tag{B.17}$$

$$= -\begin{pmatrix} \frac{1}{\tilde{\delta}_c} & 0 \\ 0 & \frac{1}{2\tilde{\delta}_c} \end{pmatrix} Q\,\Omega\,|1\rangle \tag{B.18}$$

$$= -\frac{\Omega}{\tilde{\delta}_c}|1\rangle \tag{B.19}$$

where $\tilde{\delta}_c = \omega_c - \omega_l - i\kappa/2$.

The second-order correction is

$$|\psi^2\rangle = -\left(X^{-1}Q\right)V|\psi^1\rangle \tag{B.20}$$

$$= \begin{pmatrix} \frac{1}{\tilde{\delta}_c} & 0 \\ 0 & \frac{1}{2\tilde{\delta}_c} \end{pmatrix} Q\frac{\Omega}{\tilde{\delta}_c}\left(\Omega|0\rangle + \sqrt{2}\Omega|2\rangle\right) \tag{B.21}$$

$$= \frac{\Omega^2}{\sqrt{2}\tilde{\delta}_c^2}|2\rangle \tag{B.22}$$

Thus,

$$|\psi\rangle = |\psi^0\rangle + |\psi^1\rangle + |\psi^2\rangle \tag{B.23}$$

$$= |0\rangle - \frac{\Omega}{\tilde{\delta}_c}|1\rangle + \frac{\Omega^2}{\sqrt{2}\tilde{\delta}_c^2}|2\rangle \tag{B.24}$$

B.3.1 Cavity transmission

For weak driving (small Ω), the transmitted field intensity is proportional to $\kappa|\langle 1|\psi\rangle|^2$. We fix the normalization by setting the intensity at resonance ($\omega_l = \omega_c$) to be unity:

$$\alpha\kappa|\langle 1|\psi\rangle|^2 = \alpha\kappa\frac{\Omega^2}{(\kappa/2)^2} = 1 \tag{B.25}$$

$$\alpha = \frac{(\kappa/2)^2}{\kappa\Omega^2} \tag{B.26}$$

Thus, the transmission as a function of the laser frequency is given by

$$I_T(\omega_l) = \frac{1}{1 + \left(\frac{\omega_c - \omega_l}{\kappa/2}\right)^2} \tag{B.27}$$

which is a Lorentzian distribution with the FWHM linewidth κ; see Fig. B.1.

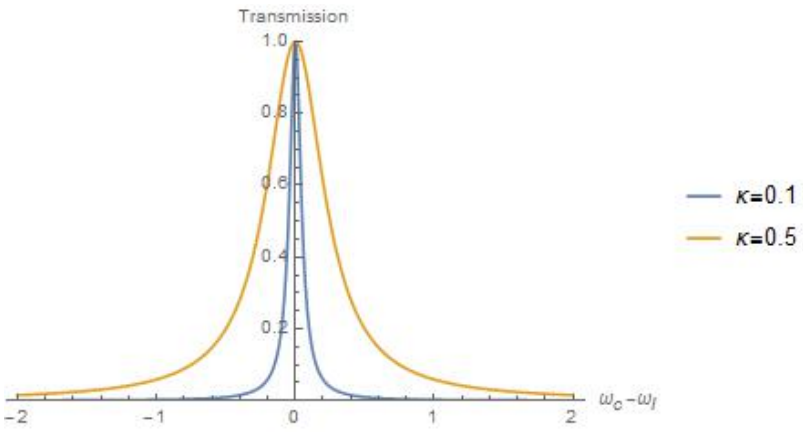

Figure B.1: **Transmission of an empty cavity** The transmission is a Lorentzian with the linewidth κ. Compare this to the cavity transmission in Chapter 2, which depicts a series of Lorentzians at each cavity resonance.

B.3.2 $g^{(2)}(0)$

The intensity autocorrelation at $\tau = 0$ is given by

$$g^{(2)}(0) = \frac{\langle a_c^\dagger a_c^\dagger a_c a_c \rangle}{\langle a_c^\dagger a_c \rangle^2} \tag{B.28}$$

$$= \frac{2\left|\langle 2|\psi\rangle\right|^2}{\left|\langle 1|\psi\rangle\right|^4} \tag{B.29}$$

$$= \frac{2(\Omega^4/2|\tilde{\delta}_c^2|^2)}{\Omega^4/|\tilde{\delta}_c^2|^2} \tag{B.30}$$

$$= 1 \tag{B.31}$$

which corresponds to that of coherent, *Poissonian* light.

B.4 One 2-level atom in a single-mode cavity

Now we add to the cavity a single two-level atom whose excited state has energy ω_e. The Hamiltonian up to the second excitation manifold is given by $H = H^0 + V$ (see Chapter 2) :

$$H^0 = \begin{pmatrix} 2\omega_l & 0 & 0 & 0 & 0 \\ 0 & \omega_l + \omega_c - i\kappa/2 & g & 0 & 0 \\ 0 & g & \omega_l + \omega_e - i\Gamma/2 & 0 & 0 \\ 0 & 0 & 0 & 2(\omega_c - i\kappa/2) & \sqrt{2}g \\ 0 & 0 & 0 & \sqrt{2}g & (\omega_c - i\kappa/2) + (\omega_e - i\Gamma/2) \end{pmatrix} \tag{B.32}$$

and

$$V = \Omega \begin{pmatrix} 0 & 1 & 0 & 0 & 0 \\ 1 & 0 & 0 & \sqrt{2} & 0 \\ 0 & 0 & 0 & 0 & 1 \\ 0 & \sqrt{2} & 0 & 0 & 0 \\ 0 & 0 & 1 & 0 & 0 \end{pmatrix} \tag{B.33}$$

where $|G\,0\rangle = \begin{pmatrix} 1 \\ 0 \\ 0 \\ 0 \\ 0 \end{pmatrix}$ denotes the ground-state atom and zero cavity photon, $|G\,1\rangle = \begin{pmatrix} 0 \\ 1 \\ 0 \\ 0 \\ 0 \end{pmatrix}$ denotes the ground-state atom and one cavity photon, $|E\,0\rangle = \begin{pmatrix} 0 \\ 0 \\ 1 \\ 0 \\ 0 \end{pmatrix}$ denotes the excited-state atom and zeo cavity photon, $|G\,2\rangle = \begin{pmatrix} 0 \\ 0 \\ 0 \\ 1 \\ 0 \end{pmatrix}$ denotes the ground-state atom and two cavity photons, and $|E\,1\rangle = \begin{pmatrix} 0 \\ 0 \\ 0 \\ 0 \\ 1 \end{pmatrix}$ denotes the excited-state atom and one cavity photon.

Now, $X = H^0 - \epsilon I$ and X^{-1} are

$$X = \begin{pmatrix} \tilde{\delta}_c & g & 0 & 0 \\ g & \tilde{\delta}_e & 0 & 0 \\ 0 & 0 & 2\tilde{\delta}_c & \sqrt{2}g \\ 0 & 0 & \sqrt{2}g & \tilde{\delta}_c + \tilde{\delta}_e \end{pmatrix} \tag{B.34}$$

$$X^{-1} = \begin{pmatrix} \frac{\tilde{\delta}_e}{\tilde{\delta}_c\tilde{\delta}_e - g^2} & \frac{-g}{\tilde{\delta}_c\tilde{\delta}_e - g^2} & 0 & 0 \\ \frac{-g}{\tilde{\delta}_c\tilde{\delta}_e - g^2} & \frac{\tilde{\delta}_c}{\tilde{\delta}_c\tilde{\delta}_e - g^2} & 0 & 0 \\ 0 & 0 & \frac{\tilde{\delta}_c + \tilde{\delta}_e}{2\tilde{\delta}_c(\tilde{\delta}_c + \tilde{\delta}_e) - 2g^2} & \frac{-\sqrt{2}g}{2\tilde{\delta}_c(\tilde{\delta}_c + \tilde{\delta}_e) - 2g^2} \\ 0 & 0 & \frac{-\sqrt{2}g}{2\tilde{\delta}_c(\tilde{\delta}_c + \tilde{\delta}_e) - 2g^2} & \frac{2\tilde{\delta}_c}{2\tilde{\delta}_c(\tilde{\delta}_c + \tilde{\delta}_e) - 2g^2} \end{pmatrix} \tag{B.35}$$

where $\tilde{\delta}_c = \omega_c - \omega_l - i\kappa/2$ and $\tilde{\delta}_e = \omega_e - \omega_l - i\Gamma/2$.

Let the initial state be $|\psi^0\rangle = |G\,0\rangle$. The first-order correction is

$$|\psi^1\rangle = -X^{-1}QV\,|\psi^0\rangle \tag{B.36}$$

$$= -X^{-1}Q\Omega\,|G\,1\rangle \tag{B.37}$$

$$= -\Omega\left(\frac{\tilde{\delta}_e\,|G\,1\rangle - g\,|E\,0\rangle}{\tilde{\delta}_c\tilde{\delta}_e - g^2}\right) \tag{B.38}$$

The second-order correction is

$$|\psi^2\rangle = -X^{-1}QV\,|\psi^1\rangle \tag{B.39}$$

$$= \Omega^2 X^{-1}Q\left(\frac{\tilde{\delta}_e\,|G\,0\rangle + \tilde{\delta}_e\sqrt{2}\,|G\,2\rangle - g\,|E\,1\rangle}{\tilde{\delta}_c\tilde{\delta}_e - g^2}\right) \tag{B.40}$$

$$= \Omega^2\left[\left(\frac{\sqrt{2}\tilde{\delta}_e}{\tilde{\delta}_c\tilde{\delta}_e - g^2}\right)\left(\frac{(\tilde{\delta}_c + \tilde{\delta}_e)\,|G\,2\rangle - \sqrt{2}g\,|E\,1\rangle}{2\tilde{\delta}_c(\tilde{\delta}_c + \tilde{\delta}_e) - 2g^2}\right)\right. \tag{B.41}$$
$$\left. + \left(\frac{-g}{\tilde{\delta}_c\tilde{\delta}_e - g^2}\right)\left(\frac{-\sqrt{2}g\,|G\,2\rangle + 2\tilde{\delta}_c\,|E\,1\rangle}{2\tilde{\delta}_c(\tilde{\delta}_c + \tilde{\delta}_e) - 2g^2}\right)\right]$$

B.4.1 Cavity transmission

$$I_T(\omega_l) \approx \alpha\kappa \left|\left(\langle G\,1| + \langle E\,1|\right)|\psi\rangle\right|^2 \tag{B.42}$$

$$= \alpha\kappa\Omega^2 \left|\frac{\tilde{\delta}_e}{\tilde{\delta}_c\tilde{\delta}_e - g^2}\right|^2 \tag{B.43}$$

where, as before, we fix the normalization by having $I_T(\omega_l = \omega_c = \omega_e) = 1$ at $g = 0$:

$$\alpha = \frac{(\kappa/2)^2}{\kappa\Omega^2} \tag{B.44}$$

Note that Equation B.43 retains its form under the following coordinate transformation: $\omega_e' = -\omega_c$, $\omega_c' = -\omega_e$, $\omega_l' = \omega_l - \omega_e - \omega_c$. This is just a manifestation of the degree of freedom inherent in picking the zero of the energy in the Hamiltonian. In our experiment, we sweep ω_l across the atomic transition, so it is common to go to the rotating frame of the atom and set $\omega_l' = \omega_l - \omega_e$ and $\omega_c' = \omega_c - \omega_e$, which yields

$$I_T(\omega_l') = \frac{(\kappa/2)^2\left[(\omega_l'^2 + (\Gamma/2)^2\right]}{\left[(\omega_c' - \omega_l')^2 + (\kappa/2)^2\right]\left[\omega_l'^2 + (\Gamma/2)^2\right] + g^4 + 2g^2\left[(\omega_c' - \omega_l')(\omega_l') + (\kappa/2)(\Gamma/2)\right]} \tag{B.45}$$

B.4.2 $g^{(2)}(0)$

$$g^{(2)}(0) = \frac{\langle a_c^\dagger a_c^\dagger a_c a_c\rangle}{\langle a_c^\dagger a_c\rangle^2} \tag{B.46}$$

$$= \frac{2\left|\langle g\,2|\psi_t\rangle\right|^2}{\left|\langle g\,1|\psi_1\rangle + \langle e\,1|\psi_2\rangle\right|^4} \tag{B.47}$$

Plots of $I_T(\omega_l)$ and $g^{(2)}(0)$ are shown above.

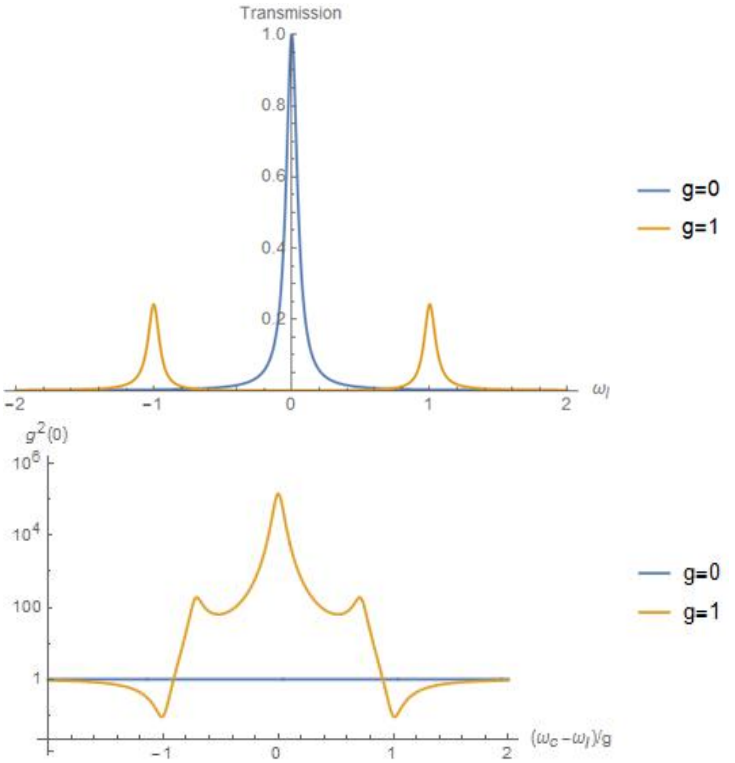

Figure B.2: **Transmission and $g_2(0)$ of a cavity containing one 2-level atom.** For both plots, the results of the empty cavity are also shown (blue). The transmission of the atom-cavity exhibits a splitting, which corresponds to the vacuum Rabi splitting; see Chapter 2. Also, $g_2(0)$ is no longer a simple Poissonian distribution.

B.5 N two-level atoms in a single-mode cavity

I first sketch what the Hamiltonian looks like for two atoms in the uncoupled basis and in the coupled basis (see Chapter 3) before proceeding to N atoms.

B.5.1 Two 2-level atoms in a single-mode cavity, uncoupled basis

$$X = \begin{pmatrix} \tilde{\delta}_c & g & g & 0 & 0 & 0 & 0 \\ g & \tilde{\delta}_e & 0 & 0 & 0 & 0 & 0 \\ g & 0 & \tilde{\delta}_e & 0 & 0 & 0 & 0 \\ 0 & 0 & 0 & 2\tilde{\delta}_c & \sqrt{2}g & \sqrt{2}g & 0 \\ 0 & 0 & 0 & \sqrt{2}g & \tilde{\delta}_c + \tilde{\delta}_e & 0 & g \\ 0 & 0 & 0 & \sqrt{2}g & 0 & \tilde{\delta}_c + \tilde{\delta}_e & g \\ 0 & 0 & 0 & 0 & g & g & 2\tilde{\delta}_e \end{pmatrix} \tag{B.48}$$

$$V = \Omega \begin{pmatrix} 0 & 1 & 0 & 0 & 0 & 0 & 0 & 0 \\ 1 & 0 & 0 & 0 & \sqrt{2} & 0 & 0 & 0 \\ 0 & 0 & 0 & 0 & 0 & 1 & 0 & 0 \\ 0 & 0 & 0 & 0 & 0 & 0 & 1 & 0 \\ 0 & \sqrt{2} & 0 & 0 & 0 & 0 & 0 & 0 \\ 0 & 0 & 1 & 0 & 0 & 0 & 0 & 0 \\ 0 & 0 & 0 & 1 & 0 & 0 & 0 & 0 \\ 0 & 0 & 0 & 0 & 0 & 0 & 0 & 0 \end{pmatrix} \tag{B.49}$$

B.5.2 Two 2-level atoms in a single-mode cavity, coupled basis

Let the states be$|g\,g\,0\rangle, |g\,g\,1\rangle, |+\,0\rangle, |-\,0\rangle, |g\,g\,2\rangle, |+\,1\rangle, |-\,1\rangle$, and $|e\,e\,0\rangle$, where

$$|+\,0\rangle = \frac{|e\,g\,0\rangle + |g\,e\,0\rangle}{\sqrt{2}} \tag{B.50}$$

$$|-\,0\rangle = \frac{|e\,g\,0\rangle - |g\,e\,0\rangle}{\sqrt{2}} \tag{B.51}$$

denote the superradiant and subradiant states, respectively.

$$X = \begin{pmatrix} \tilde{\delta}_c & \sqrt{2}g & 0 & 0 & 0 & 0 & 0 \\ \sqrt{2}g & \tilde{\delta}_e & 0 & 0 & 0 & 0 & 0 \\ 0 & 0 & \tilde{\delta}_e & 0 & 0 & 0 & 0 \\ 0 & 0 & 0 & 2\tilde{\delta}_c & 2g & 0 & 0 \\ 0 & 0 & 0 & 2g & \tilde{\delta}_c + \tilde{\delta}_e & 0 & \sqrt{2}g \\ 0 & 0 & 0 & 0 & 0 & \tilde{\delta}_c + \tilde{\delta}_e & 0 \\ 0 & 0 & 0 & 0 & \sqrt{2}g & 0 & 2\tilde{\delta}_e \end{pmatrix} \tag{B.52}$$

$$V = \Omega \begin{pmatrix} 0 & 1 & 0 & 0 & 0 & 0 & 0 & 0 \\ 1 & 0 & 0 & 0 & \sqrt{2} & 0 & 0 & 0 \\ 0 & 0 & 0 & 0 & 0 & 1 & 0 & 0 \\ 0 & 0 & 0 & 0 & 0 & 0 & 1 & 0 \\ 0 & \sqrt{2} & 0 & 0 & 0 & 0 & 0 & 0 \\ 0 & 0 & 1 & 0 & 0 & 0 & 0 & 0 \\ 0 & 0 & 0 & 1 & 0 & 0 & 0 & 0 \\ 0 & 0 & 0 & 0 & 0 & 0 & 0 & 0 \end{pmatrix} \tag{B.53}$$

The transmission and the intensity autocorrelation are identical to those calculated in the uncoupled basis.

B.5.3 N 2-level atoms in a single-mode cavity

Omitting uncoupling states, the remaining states are $|g\,g\,0\rangle, |g\,g\,1\rangle, |e+\,0\rangle, |g\,g\,2\rangle, |e+\,1\rangle$, and $|ee+\,0\rangle$, where

$$|e+\,0\rangle = \frac{|e\,g\,g\,...\,0\rangle + |g\,e\,g\,...\,0\rangle + ...}{\sqrt{N}} \tag{B.54}$$

$$|e+\,1\rangle = \frac{|e\,g\,g\,...\,1\rangle + |g\,e\,g\,...\,1\rangle + ...}{\sqrt{N}} \tag{B.55}$$

$$|ee+\,0\rangle = \frac{|e\,e\,g\,...\,0\rangle + |e\,g\,e\,...\,0\rangle}{\sqrt{N(N-1)/2}} \tag{B.56}$$

denote the superradiant superpositions. The normalization comes from the binomial coefficient (N choose 1 and N choose 2). Picking the superradiant state automatically uncouples other orthonormal states.

$$X = \begin{pmatrix} \tilde{\delta}_c & g\sqrt{N} & 0 & 0 & 0 \\ g\sqrt{N} & \tilde{\delta}_e & 0 & 0 & 0 \\ 0 & 0 & 2\tilde{\delta}_c & g\sqrt{2N} & 0 \\ 0 & 0 & g\sqrt{2N} & \tilde{\delta}_c + \tilde{\delta}_e & g\sqrt{2(N-1)} \\ 0 & 0 & 0 & g\sqrt{2(N-1)} & 2\tilde{\delta}_e \end{pmatrix} \tag{B.57}$$

$$V = \Omega \begin{pmatrix} 0 & 1 & 0 & 0 & 0 & 0 \\ 1 & 0 & 0 & \sqrt{2} & 0 & 0 \\ 0 & 0 & 0 & 0 & 1 & 0 \\ 0 & \sqrt{2} & 0 & 0 & 0 & 0 \\ 0 & 0 & 1 & 0 & 0 & 0 \\ 0 & 0 & 0 & 0 & 0 & 0 \end{pmatrix} \tag{B.58}$$

First-order transmission:

$$\langle a_c^\dagger a_c \rangle = \langle g\,1|\psi_1\rangle = \frac{\tilde{\delta}_e}{\tilde{\delta}_c\tilde{\delta}_e - g^2}\Omega \tag{B.59}$$

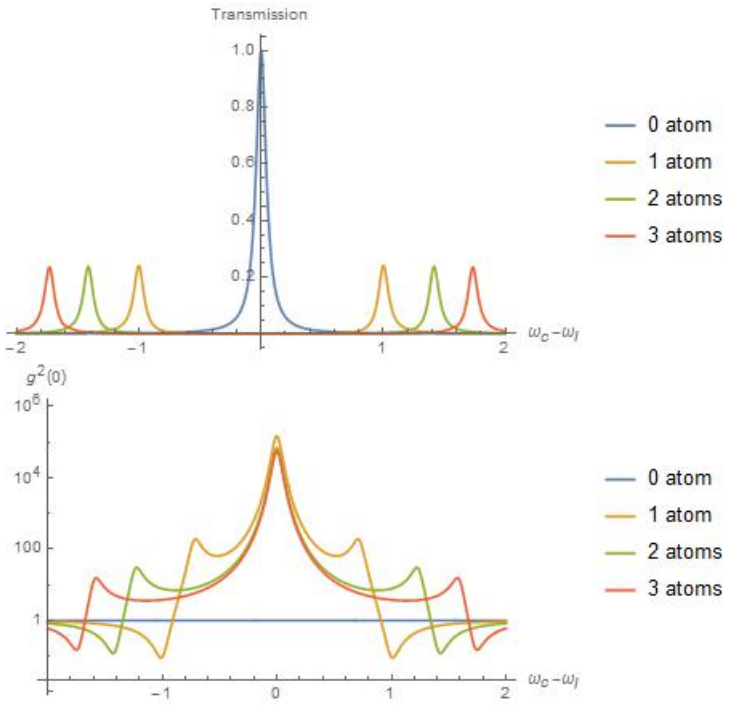

Figure B.3: **Transmission and $g_2(0)$ of a cavity containing N 2-level atoms.** The transmission shows that the vacuum Rabi splitting is given by $2g\sqrt{N}$, as expected.

$$T = \left(\frac{\kappa}{2}\right)^2 \left| \frac{\tilde{\delta}_e}{\tilde{\delta}_c \tilde{\delta}_e - (g\sqrt{N})^2} \right|^2 \tag{B.60}$$

B.6 One 3-level atoms in a single-mode cavity

$$X = \begin{pmatrix} \tilde{\delta}_c & g & 0 & 0 & 0 & 0 \\ g & \tilde{\delta}_e & \Omega_c & 0 & 0 & 0 \\ 0 & \Omega_c & \tilde{\delta}_r & 0 & 0 & 0 \\ 0 & 0 & 0 & 2\tilde{\delta}_c & \sqrt{2}g & 0 \\ 0 & 0 & 0 & \sqrt{2}g & \tilde{\delta}_c + \tilde{\delta}_e & \Omega_c \\ 0 & 0 & 0 & 0 & \Omega_c & \tilde{\delta}_c + \tilde{\delta}_r \end{pmatrix} \tag{B.61}$$

$$V = \Omega \begin{pmatrix} 0 & 1 & 0 & 0 & 0 & 0 & 0 \\ 1 & 0 & 0 & 0 & \sqrt{2} & 0 & 0 \\ 0 & 0 & 0 & 0 & 0 & 1 & 0 \\ 0 & 0 & 0 & 0 & 0 & 0 & 1 \\ 0 & \sqrt{2} & 0 & 0 & 0 & 0 & 0 \\ 0 & 0 & 1 & 0 & 0 & 0 & 0 \\ 0 & 0 & 0 & 1 & 0 & 0 & 0 \end{pmatrix} \tag{B.62}$$

where

$$\tilde{\delta}_c = \omega_c - \omega_l - i\kappa/2 \tag{B.63}$$

$$\tilde{\delta}_e = \omega_e - \omega_l - i\Gamma_e/2 \tag{B.64}$$

$$\tilde{\delta}_r = \omega_r - \omega_l - i\Gamma_r/2 \tag{B.65}$$

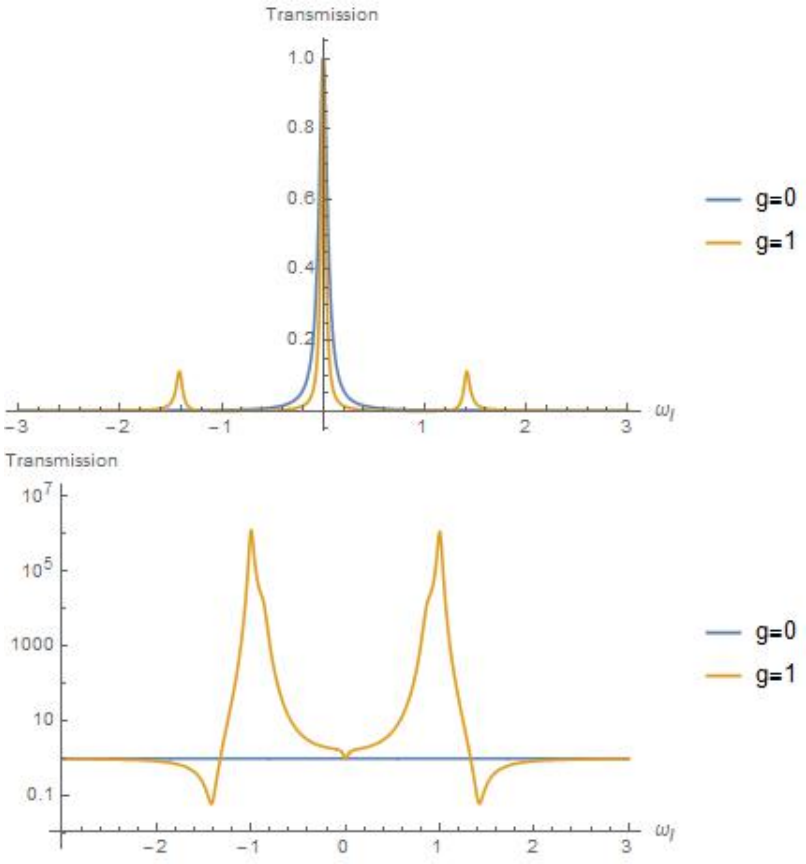

Figure B.4: **Transmission and $g_2(0)$ of a cavity containing one 3-level atom.** The transmission shows two broad bright states and one narrow dark state. The results for $g = 0$ (empty cavity) are also shown.

B.7 N 3-level atoms in a single-mode cavity

$$X = \tag{B.66}$$

$$\begin{pmatrix}
\tilde{\delta}_c & g\sqrt{N} & 0 & 0 & 0 & 0 & 0 & 0 & 0 \\
g\sqrt{N} & \tilde{\delta}_e & \Omega_c & 0 & 0 & 0 & 0 & 0 & 0 \\
0 & \Omega_c & \tilde{\delta}_r & 0 & 0 & 0 & 0 & 0 & 0 \\
0 & 0 & 0 & 2\tilde{\delta}_c & g\sqrt{2N} & 0 & 0 & 0 & 0 \\
0 & 0 & 0 & g\sqrt{2N} & \tilde{\delta}_c + \tilde{\delta}_e & \Omega_c & 0 & g\sqrt{2(N-1)} & 0 \\
0 & 0 & 0 & 0 & \Omega_c & \tilde{\delta}_c + \tilde{\delta}_r & g\sqrt{N-1} & 0 & 0 \\
0 & 0 & 0 & 0 & 0 & g\sqrt{N-1} & \tilde{\delta}_e + \tilde{\delta}_r & \sqrt{2}\Omega_c & \sqrt{2}\Omega_c \\
0 & 0 & 0 & 0 & g\sqrt{2(N-1)} & 0 & \sqrt{2}\Omega_c & 2\tilde{\delta}_e & 0 \\
0 & 0 & 0 & 0 & 0 & 0 & \sqrt{2}\Omega_c & 0 & 2\tilde{\delta}_r + V_{rr}
\end{pmatrix}$$

$$V = \Omega \begin{pmatrix}
0 & 1 & 0 & 0 & 0 & 0 & 0 & 0 & 0 & 0 \\
1 & 0 & 0 & 0 & \sqrt{2} & 0 & 0 & 0 & 0 & 0 \\
0 & 0 & 0 & 0 & 0 & 1 & 0 & 0 & 0 & 0 \\
0 & 0 & 0 & 0 & 0 & 0 & 1 & 0 & 0 & 0 \\
0 & \sqrt{2} & 0 & 0 & 0 & 0 & 0 & 0 & 0 & 0 \\
0 & 0 & 1 & 0 & 0 & 0 & 0 & 0 & 0 & 0 \\
0 & 0 & 0 & 1 & 0 & 0 & 0 & 0 & 0 & 0 \\
0 & 0 & 0 & 0 & 0 & 0 & 0 & 0 & 0 & 0 \\
0 & 0 & 0 & 0 & 0 & 0 & 0 & 0 & 0 & 0 \\
0 & 0 & 0 & 0 & 0 & 0 & 0 & 0 & 0 & 0
\end{pmatrix} \tag{B.67}$$

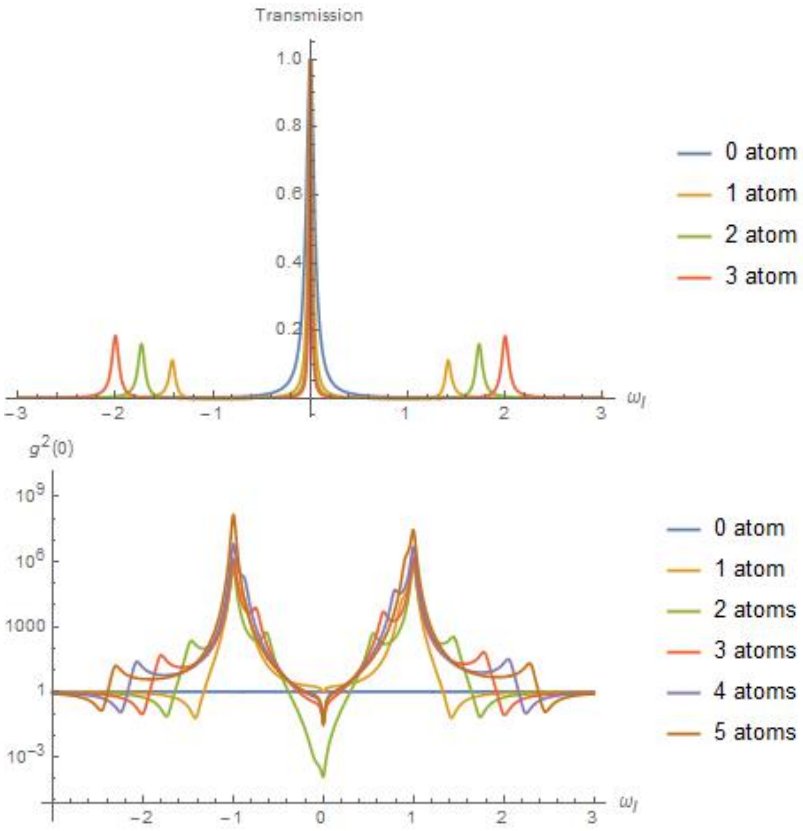

Figure B.5: **Transmission and $g_2(0)$ of a cavity containing N 3-level atoms.**

APPENDIX C

FEEDBACK STABILIZATION OF THE LASER FREQUENCY

C.1 Introduction

In this chapter, I describe the theory and the practice of locking a laser's frequency to that of a cavity (or vice versa), including the most widely-used Pound-Drever-Hall (PDH) technique. The generation of an error signal, along with the servo mechanism, is at the heart of feedback stabilization that is ubiquitous in AMO physics laboratories and beyond. For more details, see the excellent reference by Black [26].

C.2 Side-locking

The simplest method of frequency stabilization is side-locking (also called side-of-fringe or side-of-resonance locking). Here the error signal is just the cavity transmission across one of its resonances, and one puts the lock point to one side of a resonance peak. Then, frequency fluctuations in the laser result in proportional changes in the cavity's transmitted intensity. While side-lacking is quick and easy to set up, it suffers from a list problems:

1. Frequency and intensity fluctuations are coupled.

2. One cannot lock at the exact resonance frequency, since the error signal there cannot distinguish between positive or negative frequency noise.

3. The allowed range of frequency excursions is limited by the cavity linewidth.

4. The error signal is a DC signal and so it may exhibit significant amplitude noise.

Problem 1 can be solved by splitting a sample of the incident beam and subtracting it from the transmitted signal, but it involves additional optics and electronics in the setup. One might try to use the reflected beam instead, decoupling the frequency and intensity

fluctuations in a type of nulled lock-in detection, but then Problem 2 remains. On the other hand, note that whereas the transmitted and reflected beams are symmetric about the resonance, their slopes are antisymmetric.

C.3 Frequency modulation in transmission

The measurement of the slope, or the phase, of the beam can be done with frequency modulation. If we modulate the laser's frequency below the resonance, the resulting fluctuations in the transmitted intensity will be in phase, and if we modulate above the resonance, the fluctuations will be 180^{o} out of phase. The opposite holds when looking at the reflected intensity.

The modulated field incident on the cavity is given by

$$E_{inc} = E_0 e^{i(\omega t + \beta \sin \Omega t)} \tag{C.1}$$

where ω is the carrier frequency, Ω is the modulation frequency, and β is the modulation index. Note that for a monochromatic wave as in the present case, frequency modulation is equivalent to phase modulation.

Expanding the field in terms of Bessel functions, and assuming $\beta \ll 1$:

$$E_0 e^{i(\omega t + \beta \sin \Omega t)} = E_0 \sum_{-\infty}^{\infty} J_n(\beta) e^{i(\omega + n\Omega)t} \tag{C.2}$$

$$\approx E_0 \left[J_0(\beta) + 2i J_1(\beta) \sin \Omega t \right] e^{i\omega t} \tag{C.3}$$

$$= E_0 \left[J_0(\beta) e^{i\omega t} + J_1(\beta) e^{i(\omega+\Omega)t} - J_1(\beta) e^{i(\omega-\Omega)t} \right] \tag{C.4}$$

We see that in addition to the carrier, the frequency modulation has generated two sidebands with frequencies $\omega \pm \Omega$.

Let $F(\omega)$ denote the cavity transmission coefficient (see Chapter 1). The transmitted

field is

$$E_T = E_0 \left[F(\omega) J_0(\beta) e^{i\omega t} + F(\omega+\Omega) J_1(\beta) e^{i(\omega+\Omega)t} - F(\omega-\Omega) J_1(\beta) e^{i(\omega-\Omega)t} \right] \tag{C.5}$$

The transmitted intensity measured by the photodiode is $|E_T|^2$:

$$\begin{aligned} P_T = {} & P_c |F(\omega)|^2 + P_s |F(\omega+\Omega)|^2 + P_s |F(\omega-\Omega)|^2 \\ & + \sqrt{P_c P_s} \Big\{ F(\omega) F^*(\omega+\Omega) e^{-i\Omega t} - F(\omega) F^*(\omega-\Omega) e^{i\Omega t} \\ & + F^*(\omega) F(\omega+\Omega) e^{i\Omega t} - F^*(\omega) F(\omega-\Omega) e^{-i\Omega t} \Big\} \\ & + (2\Omega \text{ terms}) \end{aligned} \tag{C.6}$$

where $P_c = J_0^2(\beta) P_0$, $P_s = J_1^2(\beta) P_0$, and $P_0 = |E_0|^2$. The interference has given rise to a beat pattern between the carrier and the sidebands that contains the phase information (we neglect beating between sidebands themselves). Further simplification of this beat is as follows:

$$z = F(\omega) F^*(\omega+\Omega) - F^*(\omega) F(\omega-\Omega) \tag{C.7}$$

$$P_{beat} = \sqrt{P_c P_s} \left\{ z e^{-i\Omega t} + z^* e^{i\Omega t} \right\} \tag{C.8}$$

$$= \sqrt{P_c P_s} \left\{ \mathrm{Re}[z] e^{-i\Omega t} + i\mathrm{Im}[z] e^{-i\Omega t} + \mathrm{Re}[z^*] e^{i\Omega t} + i\mathrm{Im}[z^*] e^{i\Omega t} \right\} \tag{C.9}$$

$$= \sqrt{P_c P_s} \left\{ \mathrm{Re}[z] e^{-i\Omega t} + i\mathrm{Im}[z] e^{-i\Omega t} + \mathrm{Re}[z] e^{i\Omega t} - i\mathrm{Im}[z] e^{i\Omega t} \right\} \tag{C.10}$$

$$= 2\sqrt{P_c P_s} \left\{ \mathrm{Re}[z] \cos \Omega t + \mathrm{Im}[z] \sin \Omega t \right\} \tag{C.11}$$

The term z contains the phase information, but it turns out the only the cosine term has the right dispersion shape (for reflection, it is the sine term). We can isolate the cosine term by putting the signal through a mixer followed by a low-pass filter.

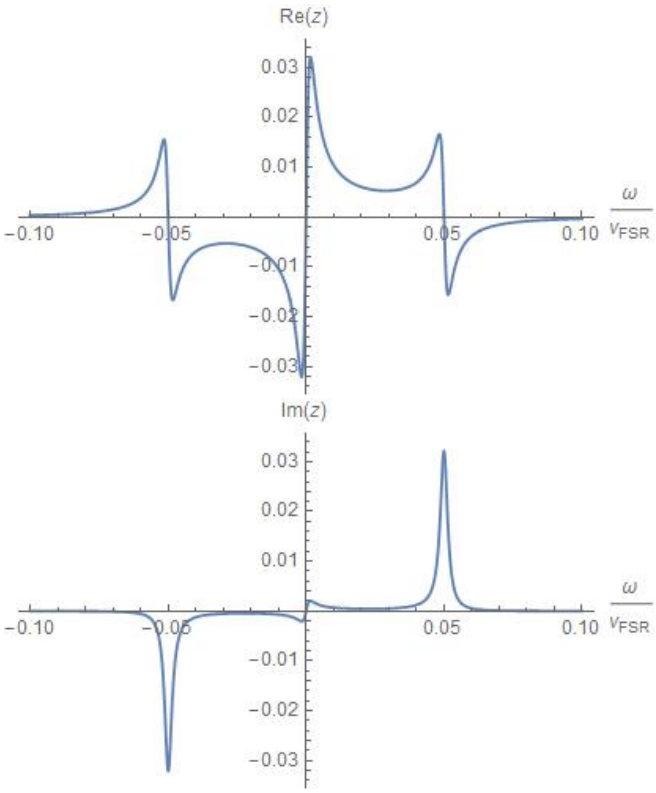

Figure C.1: **Error signal produced by frequency modulation in transmission.** (top) Re[z] and (bottom) Im[z] vs frequency in units of ν_{FSR}. The modulation frequency is at set 5% of ν_{FSR} and the finesse is about 300.

Now, let's set $F(\omega)$ equal to the transmission amplitude coefficient (from Chapter 1):

$$F(\omega) = \frac{E_T}{E_0} = \frac{t_1 t_2 e^{i\delta/2}}{1 - r_1 r_2 e^{i\delta}} \tag{C.12}$$

where $\delta = 2kd = \omega/\nu_{FSR}$. The plots of Re[$z$] and Im[$z$] are shown in Figure C.1.

Actually, frequency modulation is more commonly used in conjunction with the reflected signal rather than the transmitted signal. Then, it is called the Pound-Drever-Hall (PDH) technique, which we discuss next.

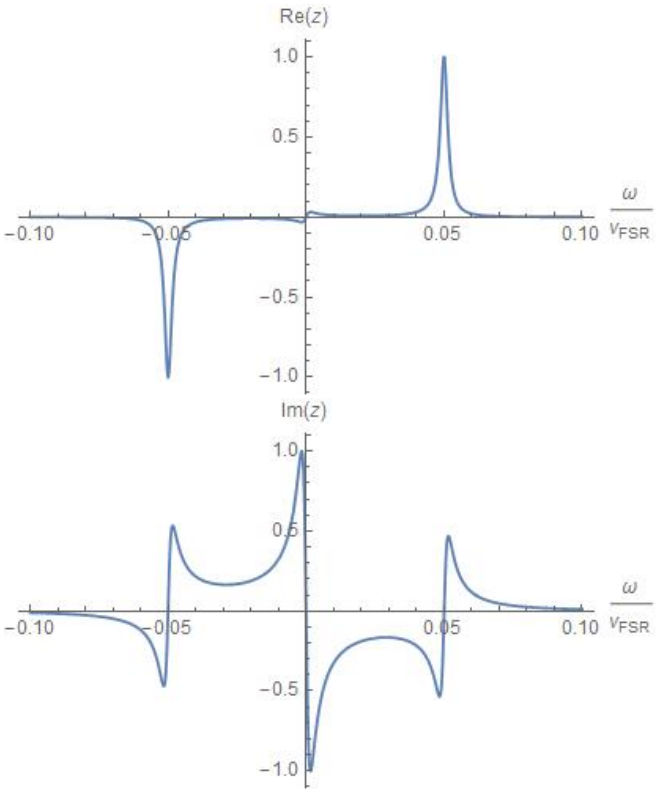

Figure C.2: **Error signal produced by frequency modulation in reflection.** (top) Re[z] and (bottom) Im[z] vs frequency in units of ν_{FSR}. The modulation frequency is at set 5% of ν_{FSR} and the finesse is about 300.

C.4 Frequency modulation in reflection, or Pound-Drever-Hall

Let $F(\omega)$ now denote the reflection coefficient, which, for a symmetric, lossless cavity, is given by (see Chapter 1)

$$F(\omega) = \frac{E_R}{E_0} = \frac{r\left(e^{i\delta} - 1\right)}{1 - r^2 e^{i\delta}} \tag{C.13}$$

where, again, $\delta = \omega/\nu_{FSR}$. The plots of Re[$z$] and Im[$z$] for the reflected beam are shown in Figure C.2.

Other than the fact that the dispersion shape we want in this case is Im[z], the PDH error signal looks essentially the same as that from transmission frequency modulation method. One difference, as we discuss in the next section, is in the *frequency response* of the lock.

C.5 Experimental implementation of the PDH

Here I describe the experimental implementation of the PDH. The basic layout of the system can be found in [26].

C.5.1 Frequency modulator

The easiest way to modulate the laser's frequency (phase) is with a fiber-coupled electro-optic modulator (EOM). In our laboratory, we employ several EOMs (EOSPACE). The downside is that they are costly ($5000).

For DFB diode lasers, another solution is to include a fast feedback board, which can directly affect the laser's injection current and is therefore not limited by the current controller's bandwidth.

The last option is to use lithium niobate crystals ($500) as EOMs. These crystals often require an amplifying circuit in tandem in order to supply a high voltage to the gold-plated surfaces.

For whatever chosen frequency modulator, the local oscillator can be a simple function generator. We frequently set our modulation frequency to 20 MHz.

C.5.2 Optical isolator

Lasers are extremely sensitive to optical feedback, so an optical isolator, though not part of the PDH per se, is a must-have. In fact, the sensitivity is made worse by the fact that we are working with a cavity, which reflects back most of the power away from a resonance. Optical feedback can be seen as a rapid random dither of the cavity transmission.

C.5.3 Accessing the reflected beam

For two-mirror cavities, the reflected beam physically overlaps with the incident beam. To isolate it, use a polarizing beamsplitter and a quarter-wavelength waveplate, so that the

returning beam goes through the other port of the beamsplitter.

C.5.4 DC block and amplifier

Before sending the reflected signal measured by a photodiode to a mixer, it is a good idea to have it go through a DC block followed by an amplifier. The DC block removes unwanted DC signal, which can come from that fact that the cavity is lossy as well as suboptimal polarizing beamsplitter and waveplate combination. The amplifier is useful for providing a good input signal for the control servo.

C.5.5 Mixer and phase shifter

We use a Mini-circuits ZRPD-1+ to mix down the reflected signal with the local oscillator signal. The mixer multiplies the two signals, producing one signal DC and the other at twice the frequency. We use a low-pass filter to isolate the DC part.

It is important that the two signals that are being mixed be at the appropriate frequency. Usually, the local oscillator that drives both the frequency modulator and the mixer with two of its channels has a built-in phase delay that can be adjusted to produce the right error signal. A more permanent solution is to use BNC cables of appropriate length as delay lines.

C.5.6 Servo, or lockbox

Finally, the error signal is fed to the control servo, which we call in our laboratory the lockbox. The lockbox implements a PI circuit with adjustable gain parameters. For locking a cavity to a laser, the gains are chosen such that the PI exactly compensates the single pole arising from the cavity piezo. See Chapter 5 for more detail on measuring transfer functions.